INSTITUTO SUPERIOR DE ENGENHARIA DE LISBOA

Department of Mechanical Engineering

Copper to Stainless Steel Welding in Lap Joint

DIOGO MANUEL FREITAS TABORDA
(BSc in Mechanical Engineering)

Master's final work to obtain the master's degree
in Mechanical Engineering

Advisors:
Prof. Dr. Ivan Rodolfo Pereira Garcia de Galvão
Prof. Dr. Carlos Miguel Almeida Leitão
Prof. Dr. Teresa Leonor Morgado

Jury:
President: Prof. Dr. Vitor Manuel Rodrigues Anes
Elements:
Prof. Dr. Rui Manuel Ferreira Leal
Prof. Dr. Ivan Rodolfo Pereira Garcia de Galvão

September of 2022

INSTITUTO SUPERIOR DE ENGENHARIA DE LISBOA

Department of Mechanical Engineering

Copper to Stainless Steel Welding in Lap Joint

DIOGO MANUEL FREITAS TABORDA
(BSc in Mechanical Engineering)

Master's final work to obtain the master's degree
in Mechanical Engineering

Advisors:
Prof. Dr. Ivan Rodolfo Pereira Garcia de Galvão
Prof. Dr. Carlos Miguel Almeida Leitão
Prof. Dr. Teresa Leonor Morgado

Jury:
President: Prof. Dr. Vitor Manuel Rodrigues Anes
Elements:
Prof. Dr. Rui Manuel Ferreira Leal
Prof. Dr. Ivan Rodolfo Pereira Garcia de Galvão

September of 2022

Acknowledgments

My first thanks goes to my supervisor, Dr. Ivan Galvão, for accepting to be my advisor and for the support, availability, and clarifications provided during this dissertation.

Also, to Dr. Carlos Leitão and Dr. Teresa Morgado for the suggestions and support during the accomplishment of this dissertation.

I would also like to express the acknowledgment to the Department of Mechanical Engineering of the ISEL by the infrastructures provided for the development of this work and by the fundaments provided during my education. A particular thanks to Prof. Joel Jesus for the support in the production of the tensile specimens of the base materials.

The acknowledgment also to the Instituto Politécnico de Lisboa, which sponsored this research through the project IPL/2021/SSWeld_ISEL.

My gratitude to the Department of Mechanical Engineering of the University of Coimbra, which provided resources and conditions to carry out part of the experimental work of this study. Especially to Mr. Fernando Bernardes for the support in the production of the welds, to Eng. Miguel Pereira for the support in the welding temperature measurements and to Dr. Luís Vilhena for the support in the analysis by scanning electron microscopy.

My gratefulness to my colleagues who accompanied me on this journey, especially my friends Paulo Faria and Diogo Lima, for a journey done together, from the long hours doing work, studying for exams, or simply hanging out.

Finally, I would like to thank my family for their constant motivation, care, and kindness.

Abstract

The development of solid-state welding over the last 30 years has offered numerous benefits compared to the more traditional techniques, especially for materials whose composition and properties are vastly different. The welded components composed of stainless steel and copper take advantage of the high strength and corrosion resistance of stainless steel and the high thermal and electrical conductivity of copper.

The aim of the present work was to study the morphological, microstructural, and mechanical properties of copper-DHP to stainless steel AISI 304 friction stir spot welds. The welding parameters, including rotational speed (870–1500 rpm), welding time (20 and 60 s), and material position, were varied to find a window of parameters allowing sound joining of these materials. Two probe-less tools were used, differing by the shoulder diameter (10 and 12 mm). After their production, the weld trials were submitted to visual inspection, macro and microstructural analysis, and microhardness and tensile-shear testing.

All the trials performed with copper as the top plate were not consistent, as no bonding was achieved at the weld interface. The temperature measured, during friction stir spot welding, increased by increasing the welding time, tool diameter, and rotational speed, which agreed with the morphological changes on the weld surface. In addition, the macrostructural analysis of the joints' transverse sections showed no material mixing or macro-defects.

The copper's microstructural analysis only exhibited a heated affected zone, which was significantly affected by the welding time. Micro-discontinuities and micro-mechanical interlocking features were seen on the weld interface, with mutual diffusion occurring between the two materials. The stainless steel showed a microhardness increase compared to the base material but decreased with increments in the welding temperature. For copper, in agreement with the grain size evolution, the microhardness decreased, and the reduction was more intense with the increase in the welding temperature.

Repeatability was seen among the trials, with the most common failure type being the nugget pull-out. The maximum load achieved during the tensile-shear testing varied between 4.1 and 5.8 kN, being influenced either by the microhardness or by the size of the bonded interface.

Keywords: Friction stir spot welding; Copper; Stainless-Steel; Dissimilar joint; Interface

Resumo

O desenvolvimento ao longo dos últimos 30 anos de soldadura em estado-sólido tem oferecido inúmeros benefícios em comparação com as técnicas mais tradicionais, especialmente para materiais cuja composição e propriedades são muito diferentes. A soldadura de materiais dissimilares permite tirar partido das melhores propriedades de cada material, enquanto a soldadura em estado-sólido permite que esta seja exequível, algo dificilmente obtido ou com piores resultados com o uso de outras técnicas para certos materiais. A ligação entre aço inoxidável e cobre tira partido da elevada resistência do aço inoxidável e da elevada condutividade térmica do cobre. Uma junta dissimilar em que o seu estudo em soldadura em estado-sólido ainda não está muito aprofundado.

A revisão da literatura apresenta a relevância da soldadura de cobre com aço inoxidável na indústria e explica o processo de *friction stir spot welding*, como também a sua variante *probe-less friction stir spot welding*. Também são apresentados estudos que recorreram a *friction stir welding* e *friction stir spot welding* entre ligas de cobre e aço, que permite uma visão geral das ferramentas e parâmetros utilizados, como também quais as técnicas de caracterização usadas e os resultados obtidos para este par numa soldadura em estado sólido.

O objetivo do presente trabalho foi estudar as propriedades morfológicas, microestruturais e mecânicas das juntas entre cobre-DHP e aço inoxidável AISI 304, obtidas através de *probe-less friction stir spot welding*. Os parâmetros de soldadura, incluindo a velocidade de rotação (870–1500 rpm), tempo de estabilização (20 e 60 s) e posição do material, foram variados para encontrar uma janela de parâmetros que permitisse a união desses dois materiais. Foram utilizadas duas ferramentas sem pino, diferindo no diâmetro da base (10 e 12 mm). Durante a execução das soldaduras procedeu-se à medição da temperatura. Após a sua produção, as soldaduras foram submetidas a inspeção visual, análise macro e microestrutural e ensaios de microdureza e tração-corte.

O posicionamento do material foi um fator determinante para se alcançarem soldaduras. Nenhum dos ensaios realizados com cobre na chapa superior produziu soldaduras consistentes, muito devido à diferença da condutividade térmica dos materiais. Dos 16 ensaios realizados foram obtidas com sucesso 6 soldaduras. A redução de diâmetro da ferramenta permitiu que as soldaduras fossem também obtidas para valores mais baixos de velocidade e tempo de estabilização. A temperatura registada durante o processo aumentou

com o aumento dos parâmetros, estando de acordo com as observações feitas através da inspeção visual sobre a intensificação das alterações morfológicas.

A análise da macroestrutura permitiu verificar que não existe mistura entre os dois materiais, isto é, a interface permaneceu muito idêntica quando do início do processo de soldadura. Ainda nesta análise, verificou-se que o tempo de estabilização teve mais impacto no comprimento de ligação do que a velocidade de rotação. A análise microestrutural mostrou que o cobre passou por um processo de recozimento, onde se verifica o crescimento de grão. Ou seja, no cobre apenas se identificou uma zona termicamente afetada que é significativamente afetada pelo tempo de estabilização, quer em dimensão quer no aumento do grão. As micrografias obtidas por microscopia eletrónica de varrimento revelaram descontinuidades micro-dimensionais e o aparecimento do fenómeno de *micro-mechanical interlocking*. Através da análise por espectrometria de dispersão de energias de raios-X, verificou-se que a ligação foi alcançada por mútua difusão entre a composição elementar (Cu e Fe) dos dois materiais.

O aço inoxidável sofreu um aumento de dureza, no entanto com uma tendência de diminuição com o aumento dos parâmetros. Além disso, verificou-se uma maior sensibilidade na variação da dureza para o aço inoxidável do que para o cobre com a variação dos parâmetros, já que este está sujeito aos efeitos da deformação e temperatura. No caso do cobre, a dureza diminuiu em relação ao valor do material base, com uma redução ainda mais acentuada à medida que os parâmetros aumentavam, algo que está de acordo com as observações feitas da microestrutura. 57.16 $HV_{0.2}$ foi o valor médio mais baixo registado para o cobre e 283.48 $HV_{0.2}$ a dureza média mais alta para aço inoxidável, correspondente às condições com introdução mais elevada e mais baixa de calor, respetivamente. Foi também observada repetibilidade entre a maioria dos ensaios de tração-corte, com o modo de falha mais comum a ser *nugget pull-out*. A força registada pelas soldaduras variou de 4.1 a 5.8 kN, sendo a dureza e o comprimento de ligação as duas características que mais influenciaram este valor.

Palavras-chave: *Friction stir spot welding*; Cobre; Aço inoxidável; Junta dissimilar; Interface

Abbreviation List

BM - Base Material

DF - Downward Force

DSS - Duplex Stainless Steel

DT - Dwell Time

EDS - Energy-Dispersive X-Ray Spectroscopy

FSSW - Friction Stir Spot Welding

FSW - Friction Stir Welding

HAZ - Heat Affected Zone

IMC - Intermetallic Compound

ITER - International Thermonuclear Fusion Experimental Reactor

LHC - Large Hadron Collider

OM - Optical Microscope

PD - Probe Diameter

PDb - Probe Diameter at the bottom

PDt - Probe Diameter at the top

PL - Probe Length

PR - Plunge Rate

RS - Rotational Speed

RSW – Resistance Spot Welding

SD - Shoulder Diameter

SEM - Scanning Electron Microscopy

SS - Stainless Steel

SZ - Stir Zone

TEM - Transmission Electron Microscopy

TMAZ - Thermo-Mechanically Affected Zone

TPD - Tool Plunge Depth

TS - Travel Speed

TSFL - Tensile-Shear Force Load

UHVS - Ultra-high Vacuum Systems

UTS - Ultimate Tensile Strength

XRD - X-Ray Diffraction

Figure Index

Table Index

Contents

1. Introduction

Welding similar and dissimilar materials is an essential element across the industry. In 1991, a newly developed solid-state welding technology was revealed, Friction Stir Welding (FSW); being Friction Stir Spot Welding (FSSW) its punctual variant, i.e., without longitudinal movement. The development of solid-state welding of similar and dissimilar materials over the last 30 years has offered numerous benefits compared to the more traditional techniques. These advantages include the elimination of solidification cracking and porosity, acceptable distortion, and improved mechanical properties in the joint. This welding technique presents other advantages inherent to the process, such as the non-emission of radiation and harmful gases and energy and cost saving.

For dissimilar joints, this type of welding also made possible the welding of materials with different physical properties, such as melting point, thermal conductivity, expansion coefficient, etc., and low chemical affinity. Given this interest in dissimilar welding, new material combinations with an industrial application have become more relevant, such as aluminum-to-copper (Al-Cu) and aluminum-to-ferrous alloys (Al-Fe).

There are still some material pairs where the research is limited, like copper and stainless steel (SS), a combination that, for example, can give to a stainless steel-based component the ability to transfer heat along its surface through the welding of a copper layer/plate. SS is recognized for its strength, while copper is known for its high capacity for conducting heat and electricity. The development of scientific work should provide a helpful understanding of the potential industrial applications, enhancing industrial development. Choosing suitable parameters, such as rotational speed, tool penetration, welding time, and material position, is essential for producing sound FSS welds.

The aim of the present work was to study the morphological, microstructural, and mechanical properties of copper-DHP to SS AISI 304 friction stir spot welds. The welding parameters, including rotational speed (870–1500 rpm), welding time (20 and 60 s), and material position, were varied to find a window of parameters allowing sound joining of these materials. Two probe-less tools were used, differing by the shoulder diameter (10 and 12 mm). Several characterization techniques, such as optical microscopy, Scanning Electron Microscopy (SEM), Energy-Dispersive X-Ray Spectroscopy (EDS), and microhardness and tensile-shear testing, were used to assess the influence of the welding parameters on the welding results.

The present work is divided into five chapters. Once the Introduction was presented, a literature review section is conducted in the second chapter. The chapter starts with the relevance of Cu/SS dissimilar welding and describes the FSSW technology and its variant, the probe-less FSSW. Then, a more dedicated review of the work already developed on the dissimilar welding between copper alloys and steel for FSW and FSSW is presented, including tools and parameters used, macro and microstructural analysis, and hardness and tensile testing. The third chapter defines the experimental procedure used for the execution and characterization of the welds. This chapter contains the materials characterization, welding process, tools and parameters selected, temperature acquisition and data treatment, and characterization techniques to study the welds. The results obtained and their discussion are presented in the fourth chapter. Finally, the conclusions and main suggestions for future work are presented in the fifth chapter.

2. Literature Review

2.1. Industrial relevance of dissimilar welding Cu/SS

The demand for copper/steel joints has increased due to the advantages of this bimetallic combination, becoming technically crucial for the most varied industries [1]. Copper has excellent thermal and electrical conductivity and good ductility. Alternatively, SS presents outstanding wear resistance, high strength, toughness, and corrosion resistance [2]. Joining these two metals is desirable in the nuclear, chemical, naval, aviation, and automobile sectors [3]. Examples are:

- Production of parts for smelting furnaces [4];
- Hybrid structures for sliding parts [5];
- Pipeline transport [6];
- Offshore platform insulators [7];
- Fabrication of the first wall and divertor in the International Thermonuclear Fusion Experimental Reactor (ITER), Ultra-high Vacuum Systems (UHVS) for particle accelerator and Large Hadron Collider (LHC) [8];
- Heat exchangers [8];
- Connecting cells in electric vehicles battery systems [9].

2.2. Friction Stir Spot Welding

FSSW, a derivative process of FSW, is a solid-state welding technique invented by Mazda to compete with the single-point joints produced by Resistance Spot Welding (RSW) and by riveted joints. It has the same operating principles as FSW but without linear translation [10,11]. Mazda first applied it in the aluminum body assembly process for automobiles. The company reported an energy reduction of 99% compared to the RSW and a 40% reduction in equipment investment [12]. FSSW was initially exclusively used to join aluminum alloys due to the complexity of selecting the suitable tool material that could withstand elevated temperatures during the process [13]. Today, FSSW is used in similar and dissimilar welding of aluminum [14], magnesium [15], titanium [16], copper [17], steel [18], aluminum-copper [19], aluminum-magnesium [20], aluminum-steel [21], polymeric materials [22], and others.

There are six different variations of the FSSW referenced in the ISO 18785-1:2018, including the conventional FSSW, probe-less FSSW [23], refill FSSW [24], and three short

travel FSW variants, including stitch FSSW [25], swing FSSW [26], and swept FSSW [27]. Other alternatives have been explored by other authors, such as the two-step FSSW [28], protrusion FSSW [29], pre-hole FSSW [30], intermediate layer FSSW [31], and double-sided adjustable tools FSSW [32], all of them with the same primary objective, which is to remove or reduce the probe-hole.

In conventional FSSW, generally applied to a lap joint, a non-consumable rotating tool consisting of a probe and a shoulder is used in the way that the mechanical interaction between the tool and the sheets produces frictional heating and plasticizes the region at the bonding interface, softening the material. The FSSW process includes three main phases, as shown in Fig. 1. With a predefined rotational speed, Fig. 1a), in the plunging phase, Fig. 1b), the cylindrical tool gradually plunges, at a specific plunge rate, into the overlapped sheets to a predetermined depth. Due to the tool's downward force, an anvil is used at the bottom of the workpiece. As soon as the plunge depth is achieved, the welding phase starts, as represented in Fig. 1c). The tool stays at that depth for a period defined as the welding time to promote the mixing between the materials and the formation of the solid-state joint. Fig. 1d) shows the last phase, i.e., the retracting phase in which the tool is retracted from the workpiece, leaving a probe-hole [10,33,34].

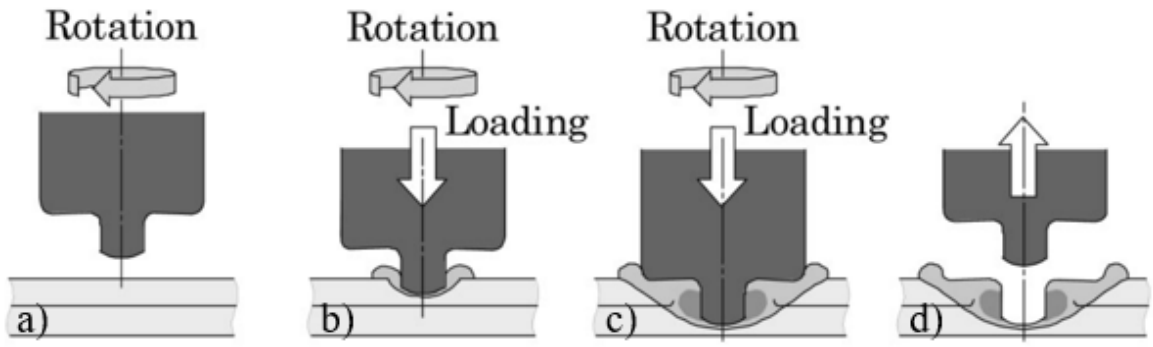

Figure 1 - Schematics of conventional FSSW process stages: a) pre-plunging rotation, b) plunging, c) welding (stirring), and d) retraction [35].

The three primary purposes of the tool are to induce the heating of the workpiece, stir and mix the plasticized material, and restrict the overflow of plasticized material out of the weld zone. The tool's geometry affects the weld quality. Due to the tool wear, the material selection is essential to prevent changes in tool geometry, interaction, contamination, and, consequently, the degradation of the weld strength. For probe-less FSSW, using a shoulder with features is also essential to ensure control to avoid tool adhering and shearing with the upper layer [11,36,37].

There are four main parameters in FSSW: the tool's rotational speed, plunge rate, plunge depth, and welding time. The rotational speed is associated with mixing and stirring control and heat generation since almost all the energy generated during FSSW is contributed by the tool torque [11,37]. The plunge rate determines the heating rate, energy utilization efficiency, and extent of plasticity, which means that more energy is produced for a lower plunge rate. This concept is more prominent for shorter welding times, given that the process temperature tends to be less sensitive to the plunge rate as the total process time increases [10,11]. The plunge depth is the distance at which the tool penetrates the joint and is determined by the sheet thickness and geometry of the tool, significantly influencing the joint dimensions, macrostructure, and weld strength. It should not be excessive so that a significant quantity of the upper sheet material is extruded, causing an excessive thinning of the top sheet or too reduced so that the tool does not promote bonding. This parameter can be force or position-controlled, which is the method to maintain the required force or position on the tool during welding, respectively [11,13,37]. Finally, the welding time is the period when the tool is in the welding phase, providing the energy necessary to form a bonded region between the upper and lower sheets. A welding period is applied to increase the tool shoulder contribution to the material flow and heat generation [11,13].

The tool's vertical positioning evolution over time is represented in Fig. 2, as well as the corresponding stages. The rotational speed is constant during the process, not depicted in the figure.

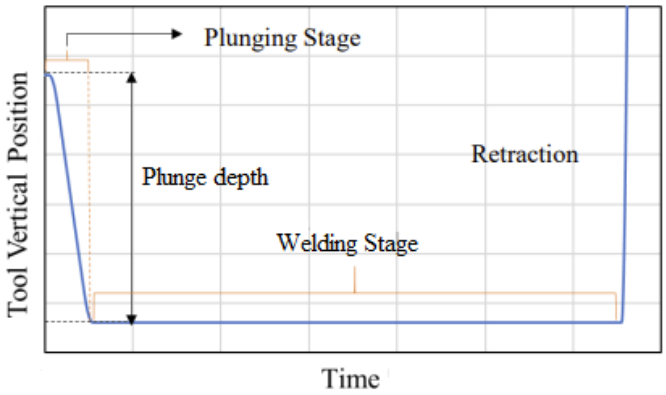

Figure 2 - Evolution of the tool's vertical position with time, adapted [10].

Typically, FSSW and FSW produce three distinct microstructural zones: a Stir Zone (SZ), a Thermo-Mechanically Affected Zone (TMAZ), and a Heat Affected Zone (HAZ), which can be recognized in sequence from the probe-hole periphery towards the Base Material (BM) [11]. As an example, Fig. 3 shows the three distinct zones of a dissimilar probe-less FSSW.

In the SZ, high plastic deformation and temperature cause dynamic recrystallization of the grains. This region is characterized by an onion ring structure, i.e., one of the most noticeable features of friction stir welds because cylinder-shaped layers of material are extruded during each tool rotation [38]. In FSSW, this effect is less observable; however, it was seen when using a probe-less feature tool due to the material flow [11,23,39]. The TMAZ is subjected to heat and plastic deformation, but there is no grain recrystallization due to insufficient strain. The HAZ is exposed to a thermal cycle without any plastic deformation, under which certain conditions may lead to coarsening or changes in the precipitation structure and density [40,41]. Finally, neither heating nor plastic deformation affects the microstructure in the BM, thus remaining unchanged [33,42].

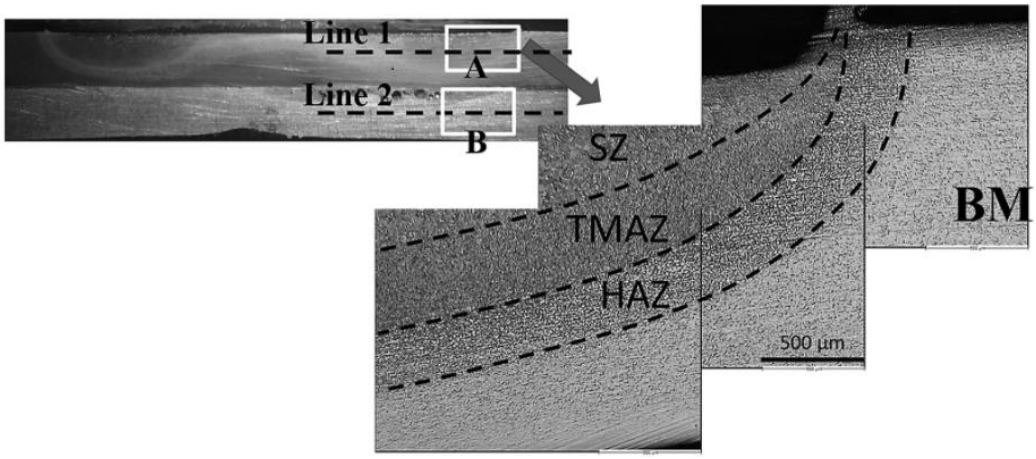

Figure 3 - Microstructure of dissimilar probe-less FSSW of DP600/Zn/AA6061, adapted [43].

2.2.1. Probe-less Friction Stir Spot Welding

Probe-less FSSW has the same basic principles as the conventional FSSW. In its first application, it used a probe-less scroll-grooved tool. Fig. 4 illustrates the indentation difference between these two types of FSSW, with the probe-less variant not producing a probe-hole [23,34], removing the stress concentration factor. This FSSW variation may produce a comparable or even superior joint integrity, with a reduced hooking defect and a remarkable advantage for joining thin materials. Since the tool is composed only of a shoulder, it can be considered an extreme example of a probe tool [10,11].

The flow pattern is also different from the conventional FSSW, as indicated by the arrows in Fig. 4. A predominant vertical flow in the conventional FSSW is seen, while in the probe-less variant, a horizontal flow with a less intense hook formation is observed. The hook formation can occur since the sheet interface suffers from an upward bending due to the tool penetration force into the lower sheet, which can affect the strength [44]. In Fig. 4a), the

material is pushed down close to the bottom surface and then moves upward away from the material that flows downwards. Unlike this material movement, in Fig. 4b), it is observed that the material starts to flow to the center of the tool. Then a downward movement occurs in that same area due to the tool geometry, leading to a material movement toward the limit of the shoulder actuation zone. For the probe-less scrolled tool, it is common to see the formation of onion rings at the upper sheet and grain refinement. The forces and loading rates for a tool surface with inscribed geometrical features are higher than in conventional FSSW, and critical shoulder penetration is necessary to achieve reliable weld performance [11,23,45].

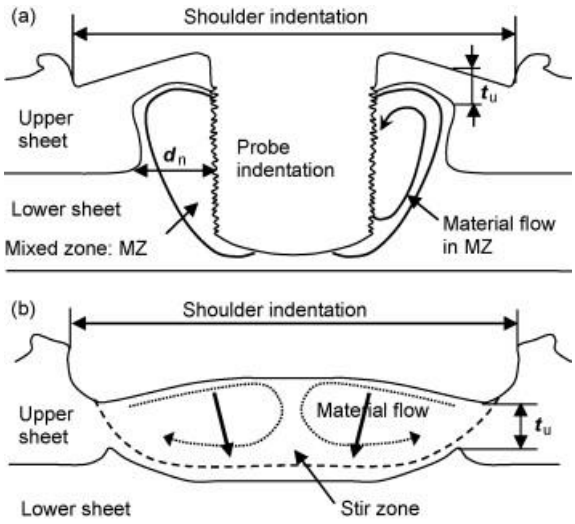

Figure 4 - Schematic illustration of weld structures: a) probe tool and b) probe-less scrolled tool [23].

2.3. Tool design and material position in Friction Stir Spot Welding and Friction Stir Welding of copper alloys to steel

Table 1 summarizes the tool material and geometry in FSSW and FSW of copper alloys to steel. The best tool geometry is highlighted in case different options have been tried. The workpiece material and thickness column is organized so that the first material that appears is on top or at the Retreating Side (RS) for lap and butt joints, respectively.

For most of the work conducted in lap joining, either in FSSW or FSW, the copper alloy is placed on a steel substrate. Almost no study mentions the reason for this selection, and neither analyzes the impact of copper or steel being used as a substrate. However, Sahlot et al. [46], who welded by placing the copper alloy as the bottom sheet, reported that plunging through copper would result in higher heat input to plasticize the bottom steel, which could lead to an extreme weakening of copper due to abnormal grain growth. On the other hand,

for butt joining, the copper alloy is always placed on the RS and the steel on the Advancing Side (AS) since there is a greater easiness of penetration of steel into copper.

The thickness of the materials evaluated in the literature varies between 1 and 6 mm. For most of the works on lap joining, the substrate plate is two times thicker than the upper material. In general, three types of probe geometry have been used in literature, i.e., the cylindrical probe, the tapered probe, and probe-less. The probe length is usually inferior to the material thickness, while the shoulder diameter varies between 10 and 22 mm. The tools can also have an additional geometry in the shoulder besides a flat one, i.e., a shoulder groove with two one-lap ridges or a convex shoulder. For the analyzed studies, there is a balance between the number of studies that used a tapered and a cylindrical probe. However, as for the shoulder, there is a tendency to use a flat one. The most common tool materials used are WC, WC-Co, and W-Re, with the earlier studies using H13 and SKH51.

The only three studies that performed copper/steel FSSW used both material positions, either with the copper alloy on the upper or lower layer. The three studies performed a lap joint on a 1 mm upper sheet, with two of the studies opting for a tool with a minimal probe length of 0.6 and 0.9 mm and the other with a probe-less tool [47–49].

Regarding the FSW works in which different tool designs were compared, Shen et al. [50] addressed the cladding of steel with copper using two types of tools, a tapered probe geometry and a hexagonal flat faceted probe. Cladding FSW differs from lap FSW since its objective is to provide an extra layer to another material achieved by the tool's successive and spaced passes. This study revealed that, for similar welding parameters, the tool with a hexagonal flat faceted probe had higher apparent penetration since more steel fragments were created, which were moved into the copper layer, resulting in a more significant formation of voids. This tool geometry could not achieve the robust mechanical interlocking created by the hook effect, which was visible when using the tapered probe. No wear of the tool was detected using a Co-WC cermet material tool.

Another analysis was made by Joshi and Badheka [8], testing different tool shoulder diameters with fixed parameters on a butt joint. The authors used a tool with the same tapered probe and four different shoulder diameter dimensions, which ranged from 16 to 22 mm. Two significant defects occurred when using the 16 mm tool, specifically, lack of material filling and surface voids due to cold conditions. No significant defects were reported for the other shoulder diameters except the flash defect, which increased as the tool shoulder

diameter increased. However, void defects were detected in the cross-section, which was explained by the increased size of SS particles due to the higher heat input, leading to excessive softening. The best joint was obtained using the 18 mm shoulder diameter. A similar analysis was made by Gao et al. [51], but this time on a lap joint with five different tools changing the probe diameter and shoulder diameter, which ranged from 6 to 10 mm and 15 to 20 mm, respectively. The five kinds of tools produced sound joints. However, the tensile-shear strength decreased with the increase of probe and shoulder diameters, justified by the grain size increase in the SZ of the brass for larger-diameter tools.

Table 1 - Summary of tool material and geometry in FSSW and FSW of copper alloys to steel.

Process and Joint configuration	Workpiece material and thickness	Tool geometry	Tool material	Ref.
Probe-less FSSW Lap joint	Carbon steel/Copper (1 mm)	Flat SD: 10 mm	Carbide	[48]
FSSW Lap joint	Brass/Dual-phase steel (1 mm)	Concave SD: 15 mm PL: 0.6 mm		[47]
FSSW Lap joint	Brass (1 mm)/Low carbon steel (2 mm)	SD: 20 mm; PD: 8.2 mm; PL: 0.9 mm	WC	[49]
Probe-less FSW Lap joint	Copper alloy (3.6 mm)/Low carbon steel (4 mm)	Flat SD: 17 mm	SKH51	[52]
FSW Lap joint	Copper (1.1 mm)/SS (1 and 6 mm)	Two grooves one-lap ridge SD: 16 mm; Threaded PD: 6 mm; PL: 0.92 mm	H13	[2]
FSW Lap joint	Brass (3 mm)/Plain carbon steel (5 mm)	Concave SD: 15 mm; PD: 6 mm; PL: 2.9 mm	WC-Co	[5]
FSW Lap joint	Brass (3 mm)/Plain carbon steel (5 mm)	Concave SD: **15** and 20 mm; PD: **6**, 8, and 10 mm; PL: 2.9 mm	WC-Co	[51]
FSW Lap joint	SS (3 mm)/Copper alloy (6 mm)	SD: 16 mm; Spiral tapered PDb: 7.5 mm; PDt: 6 mm; PL: 4 mm	W-25%Re	[46]
Cladding FSW Lap joint	Copper (2.1 mm)/Structural carbon steel (25.4 mm)	**Tool 1**: SD: 12 mm; PDb: 5 mm; PDt: 4 mm; PL: 2.1 mm; Tool 2: hexagonal flat faceted probe: 0.5 mm	Co-WC cermet	[50]
Cladding FSW Lap joint	Copper (3 mm)/Mild steel (6 mm)	SD: 20mm; PD: 6,5 mm; PL: 3.5 mm	WC	[53]
FSW Butt joint	Copper/SS (5 mm)	SD: 22 mm; PD: 5 mm; PL: 4.9 mm	Probe: WC Shoulder: molybdenum	[54]
FSW Butt joint	Copper/SS (2 mm)	SD: 10 mm; PDb: 4 mm; PDt: 2 mm;	Tungsten based alloy	[55]
FSW Butt joint	Copper/SS (3 mm)	SD: 17 mm; tapered PDb: 6 mm; PL:2.8 mm	Probe: WC Shoulder: M2 steel	[56]
FSW Butt Joint	Copper/SS (3 mm)	PDb: 5 mm, PDt: 3 mm; PL: 2.9 mm	Cryogenic-treated WC refractory	[57]
FSW Butt joint	Copper/DSS (4 mm)	SD: 20 mm; PDb: 5 mm; PDt: 3 mm; PL: 4 mm	WC	[1]
FSW Butt joint	Copper alloy/SS (2 mm)	SD: 18 mm; PD: 6 mm; PL: 1.8 mm	WC	[7]

FSW Butt joint	Copper/SS (6 mm)	SD: 16 mm; PDb: 7 mm; PDt: 4 mm; PL: 4 mm	W-Re	[3]
FSSW Butt joint	Copper/SS (3 mm)	Spiral tapered PDb: 5 mm; PDt: 3 mm; PL: 2.9 mm; Tool 1: SD: 16 mm; **Tool 2**: SD: 18 mm; Tool 3: SD: 20 mm; Tool 4: SD: 22 mm	Cryogenic-treated WC+6%Co	[8]
FSW Butt joint	Copper/Plain carbon steel (3 mm)	SD: 18 mm; tapered PL: 2.85 mm		[58]
SD: Shoulder Diameter; PL: Probe Length PDb: Probe Diameter at the bottom; PDt Probe Diameter at the top; PD: Probe Diameter				

2.4. Process parameters in Friction Stir Spot Welding and Friction Stir Welding of copper alloys to steel

Table 2 summarizes the welding parameters used in FSSW and FSW of copper alloys to steel, following the same presentation logic of Table 1. The highlighted parameters are the ones considered by the authors to be the best parameters according to the defects observed and, especially, with the ultimate tensile strength (UTS) achieved.

The literature shows that the rotational speed is the parameter common to the various variations, either in FSSW or FSW, with values ranging from 400 to 1800 rpm. The welding time, characteristic of FSSW, ranged from 8 to 30 s. For FSSW, a consensus is seen between authors [47–49]; by increasing the rotational speed and welding time, so does the Tensile-Shear Force Load (TSFL). Ataya et al. [49] explained that this evolution was due to higher generated heat, which allowed better cohesion of the copper alloy on steel and higher penetration of the extruded steel into the copper alloy. Nevertheless, the excessive rise of these parameters would lead to an extreme softening of the copper alloy, leading to a lower joint strength.

Regarding the FSW studies, the selection of the rotational speed influences the travel speed chosen and vice versa. Nevertheless, a relationship between these two parameters and identifying whether there is a tendency to use higher or lower values is more difficult to obtain, with these values varying among the studies. The travel speed in FSW can be considered to have an inverse behavior to that of the welding time in FSSW, having the most significant variation between studies, ranging between 10 and 600 mm/min. For example, according to Martins [2], bonding was not achieved when joining copper and SS with low rotational speeds due to a rapid variation in temperature and lack of heat input. With higher rotational speeds, the probe exhibited accelerated wear, making it possible to observe debris throughout the entire thickness of copper. Gao et al. [5] detected two major defects when FSW was used to join brass and plain carbon steel on a lap joint. Fig. 5 reveals the range of welding parameters where larger burrs and grooves were seen for excessive heat input conditions or absence of joining when incipient heat input conditions were used. However, in this study, the tensile-shear fracture load of the joints increased remarkably as the travel speed decreased. A similar result was observed by Shokri et al. [1]. The effects of rotational and travel speed were also investigated by Aval [7] in FSW between brass and SS, with

tunneling defects present when the rotational to travel speed ratio was lower than 10 r/mm and longitudinal cracking at the interface appearing for a ratio greater than 20 r/mm.

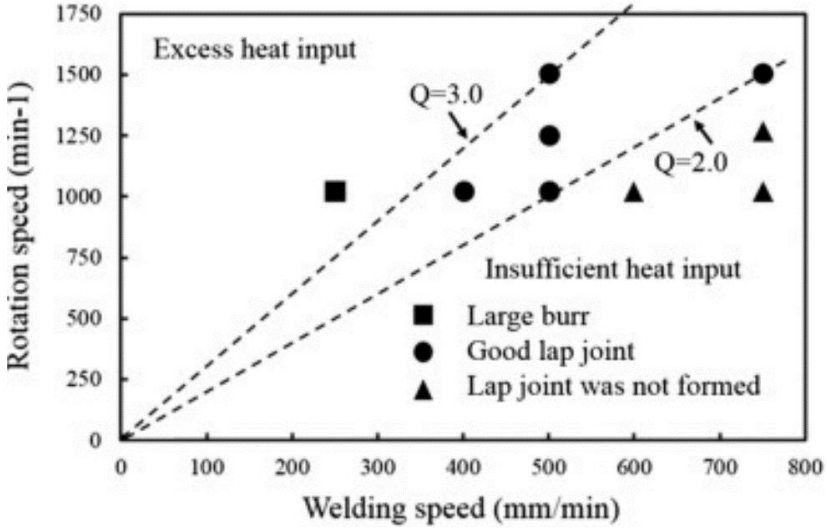

Figure 5 - Combined effect of tool's rotational speed and welding speed on FSW between brass and steel [5].

Another parameter common to FSSW and FSW is the plunge depth, which can be achieved by position or force control, with the definition of the tool plunge depth or downward force parameters, respectively. The values used remained between 0.2 and 1 mm for tool plunge depth and between 3.2 and 14 kN for downward force, influenced by the thickness of the material, tool geometry, and other parameters. The impact of the tool plunge depth was analyzed by Abdullah and Hussein [48], with values varying between 0.2 and 1 mm when using a probe-less tool for FSSW. The authors verified that a value of 0.85 mm achieved the best tensile strength related to the applied pressure. Shen et al. [50] focused on steel cladding with copper, testing a variable tool penetration (0.06–0.6 mm). The authors observed that bonding was not promoted for a plunge depth inferior to 0.15 mm, while voids and steel fragments were detected with higher penetrations. The best plunge depth was from 0.25 to 0.27 mm. Barlas [47], when performing FSSW, reported that the best weld was achieved using the highest axial load of 4.8 kN when this parameter was varied between 3.2 and 4.8 kN.

Two other parameters very typical in FSW are the tilt angle, with values ranging from 1º to 3º, and, for a butt configuration, the lateral offset towards the copper side, which varied between 0.75 and 2 mm. Shokri et al. [1] were the only authors to study the impact of the variation of the lateral offset towards copper. These authors verified that increasing the tool offset also increased the strength of the joint because it induced more heat into the welding zone, allowing duplex-SS pieces to react and mix more intensely with the copper. However,

this increment, combined with increased rotational speed, could reduce the bonding strength due to copper softening. In the same way, Jafari et al. [56], in the only study where the tilt angle parameter was varied, observed that the maximum UTS was obtained when using the median value of 1.8º among the values tested, 1º to 2.6º, since when inappropriate parameters were used porosity, cracks and unsightly appearance were seen. This analysis was made using the response surface methodology.

Additional works studied the influence of other parameters outside the conventional ones, like the effect of a nickel coating on the shear strength of a lap weld between brass and low-carbon steel. The thickness of the Ni coating on the brass sheet was kept constant at 5 μm but varied between 5 and 40 μm on the steel sheet. It was seen that a layer of 20 μm on the steel side reached the saturation strength value [52].

Joshi and Badheka [57] performed heating and cooling assisted FSW, using a TIG welding torch in front of the tool and compressed air or water behind it. The variables were three different preheating currents, two different pressures for the compressed air, and just one flow of water. As cooling conditions increased, a deterioration of the tensile strength was seen, with minor degradation as the heating current increased. Both cooling and heating-assisted FS welds exhibited significant cracks and voids. Thus, the best weld quality was achieved by using conventional FSW. Contrary to this, in FSSW, the same no longer happened; the pre-heating created by the tool in contact with the top sheet for 15 s before welding proved to be beneficial [48].

A recent research by Giridharan et al. [58] performed a biochar-assisted copper/steel FSW using biochar as a solid lubricant for the butt joint. The biochar additions were 0.5 to 4 wt.%. It was observed that adding biochar improved the joint's mechanical properties, being related to the enhanced heat distribution and microstructure. The best performance was achieved with 2 wt.% of biochar.

Table 2 - Summary of parameters in FSSW and FSW of copper alloys to steel.

Process and Joint configuration	Workpiece material and thickness	Welding parameters	Remarks	Ref.
Probe-less FSSW Lap joint	Carbon steel/Copper (1 mm)	RS: 1120-**1800** rpm; PR: 16 mm/min; TPD: 0.2-**0.85**-1 mm	The pre-heating process was done for 15 s between the rotating tool and the upper surface	[48]
FSSW Lap joint	Brass/Dual-phase steel (1 mm)	RS: 1200 rpm; DF: 3.2-**4.8** kN; DT: 8 and **12** s		[47]
FSSW Lap joint	Brass (1 mm)/Low carbon steel (2 mm)	RS: **1000**-1500 rpm; DF: 11-**13** and 14 kN; PR: 6 mm/min; DT: 5-**20** and 30 s		[49]
Probe-less FSW Lap joint	Copper alloy (3.6 mm)/Low carbon steel (4 mm)	RS: **800**-**1400** rpm; TS: **10**-80 mm/min; TPD: 0.3 mm; DT: 90 s; tilt angle: 1º	Nickel coating on the copper side of 5 μm and 400 SS of 5, 10, 20, and 40 μm	[52]
FSW Lap joint	Copper (1.1 mm)/SS (1 and 6 mm)	RS: 800-**1800** and 2000 rpm; TS: 60 and **90**-180 mm/min; PR: 6 mm/min DF: 5.5 kN; DT: 5 s		[2]
FSW Lap joint	Brass (3 mm)/Plain carbon steel (5 mm)	RS: **1000**-1300 rpm; TS: 250-**500** and 600 mm/min; DF: 9.8 kN; tilt angle: 3º		[5]
FSW Lap joint	Brass (3 mm)/Plain carbon steel (5 mm)	RS: 1000 rpm; TS: 500 mm/min; DF: 9.8 kN; tilt angle: 3º		[51]
FSW Lap joint	SS (3 mm)/Copper alloy (6 mm)	RS: 850 rpm; TS: 50 mm/min; PD: 0.25 mm; tilt angle: 2.5º		[46]
Cladding FSW Lap joint	Copper (2.1 mm)/Structural carbon steel (25.4 mm)	RS: 1120 rpm; TS: 31,5 mm/min; TPD: 0.06-0.6 mm **0.25**-**0.27**; tilt angle: 2.5º		[50]
Cladding FSW Lap joint	Copper (3 mm)/Mild steel (6 mm)	RS: 700 rpm; TS: 100 mm/min; tilt angle: 1.5º		[53]
FSW Butt joint	Copper/SS (5 mm)	RS: 720 rpm; TS: 16 mm/min	Argon gas was used for surface protection	[54]
FSW Butt joint	Copper/SS (2 mm)	RS: 1000 rpm; TS: 40 mm/min; lateral offset: 3 mm		[55]
FSW Butt joint	Copper/SS (3 mm)	RS: 700-**1170** and 1450 rpm; TS: **25**-60 mm/min; tilt angle: 1-**1.8**-2.6º		[56]
FSW Butt Joint	Copper/SS (3 mm)	RS: 1500 rpm; TS: 31.5 mm/min; tilt angle: 2º; lateral offset: 2 mm	Preheating and cooling assisted	[57]
FSW Butt joint	Copper/DSS (4 mm)	RS: 1000, **1200,** and 1400 rpm; TS: 20 and **30** mm/min; TPD: 0.1 mm; tilt angle: 3º; lateral offset: 0, **1.5**, 2 mm		[1]

FSW Butt joint	Copper alloy/SS (2 mm)	RS: 800 and **1000** rpm; TS: 40-**80** mm/min; lateral offset: 0.75 mm		[7]
FSW Butt joint	Copper/SS (6 mm)	RS: **400** and 500 rpm; TS: **25** and 50 mm/min; PD: 0.75 mm; tilt angle: 2.5º; lateral offset: 2 mm		[3]
FSSW Butt joint	Copper/SS (3 mm)	RS: 1500 rpm; TS: 40 mm/min; tilt angle: 2º; lateral offset: 2 mm		[8]
FSW Butt joint	Copper/Plain carbon steel (3 mm)	RS: 900 rpm; TS: 30 mm/min; TPD: 0.2 mm; DT: 5 s; DF 5 kN	Various wt.% of biochar used, such as 0.5, 1, **2** and 4	[58]
RS: Rotational Speed; PR: Plunge Rate; TPD: Tool Plunge Depth; DF: Downward Force; DT: Dwell Time; TS: Travel Speed				

2.5. Macro/Microstructural characterization in Friction Stir Spot Welding and Friction Stir Welding of copper alloys to steel

The optimization of the welding parameters requires the accurate analysis of the weld cross-section, where a macroscopic trend between the process and joint configuration was seen among the studies. Fig. 6 shows the four macrostructures' examples found for FSSW, cladding, lap, and butt FSW. In FSSW, shown in Fig. 6a), there is a reduction in the thickness of the copper alloy since it is the weaker material. A spot weld also potentiates the creation of localized heat softening even further the copper alloy, which is extruded to the periphery of the tool [49]. When performing cladding FSW, particularly in the first pass, there is a predominant hook effect, Fig. 6b), which is justified by the evident tool penetration into the steel, allowing the steel to be displaced into the upper copper sheet by the movement of the tool [50]. For FSW on a lap joint, Fig 6c), the interface line is very similar to that of the materials before welding since, in this case, the length of the probe and the penetration tends to be smaller than the thickness of the upper material [5]. Finally, Fig. 6d), FSW on a butt joint, shows a severe mixing between the two materials at the weld nugget with the creation of steel fragments, characteristic of this joint configuration due to the hardness difference between the two welded materials [1].

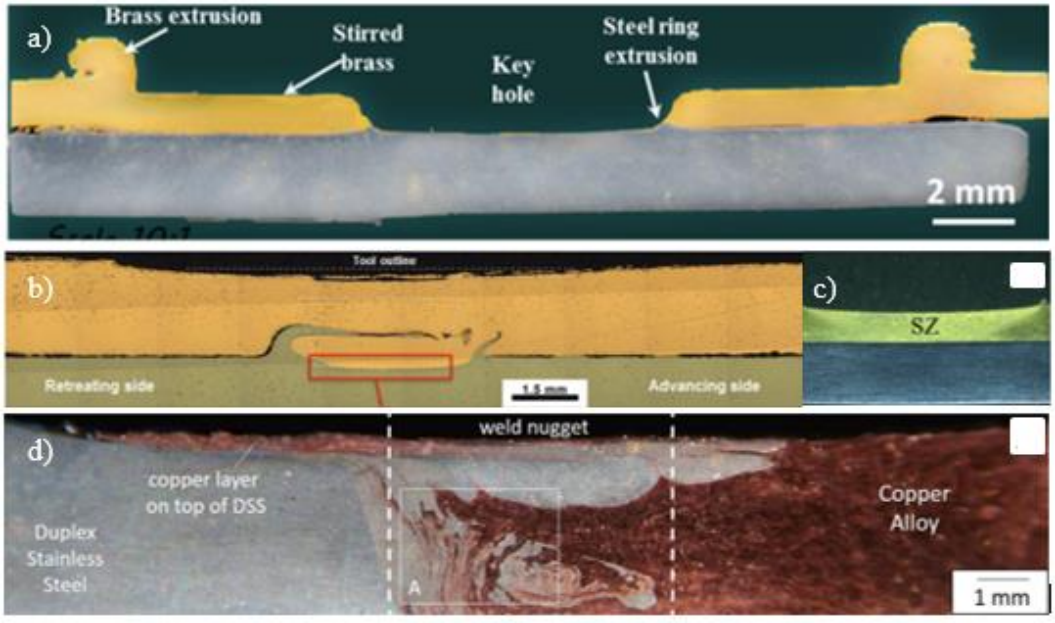

Figure 6 - Macrostructure example: a) FSSW, b) Cladding FSW, c) Lap joint FSW, and d) butt joint FSW, adapted [1,49–51].

The typical hook formation with some material dragged out of the edge was reported in FSSW and cladding FSW, leading to steel being displaced into the upper copper sheet with

more or less intensity, which improved the mechanical interlocking between the materials [48–50,53]. Fig. 7 shows other features reported at the weld interface. In the cladding interface from the studies by Shen et al. and Mahto et al. [50,53], it was visible that the Cu had mushroomed and penetrated the substrate (Fig. 7a)). A peak and wave formation was seen, showing good interlocking across the interface; however, poor bonding was achieved outside the SZ and yet below the shoulder. Sahlot et al. [46] also observed a severe mechanical mixing between the two materials at the interface at a micro-level during lap FSW, which can be seen in Fig. 7b). This was justified by the presence of a probe with a slightly greater length than the upper material thickness.

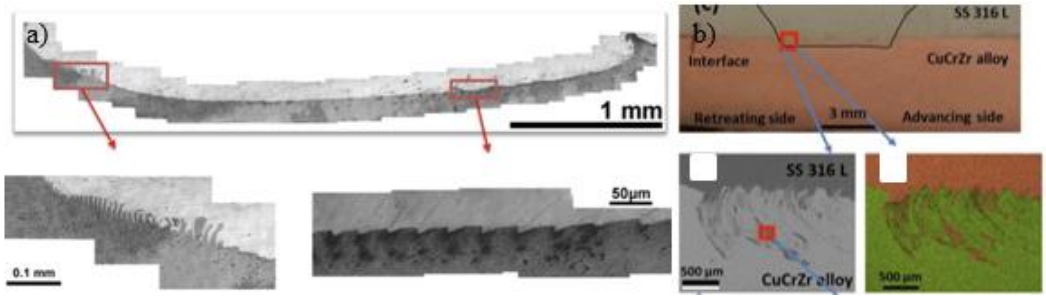

Figure 7 - Interface microstructures features: a) cladding and b) lap FSW, adapted [46,50].

In general, no macrostructural defects were found in the studies since the best parameters were previously selected before the cross-section analysis. However, for FSSW, the material thickness reduction often leads to flash formation [47–49]. Additionally, when the interface was analyzed at the microstructural level, it was possible to see some defects. For example, partially bonded regions, lack of consolidation, or even nano-sized voids were found to be formed in the joint. The nano-sized voids were formed either due to inadequate mixing or residual surface oxides, which were too small to be observed in the optical microscope (OM) [2,5,50,53]. Fig. 8 shows two defects seen at the interface, corresponding the Fig. 8a) to nano-sized voids and Fig. 8b) to lack of joining.

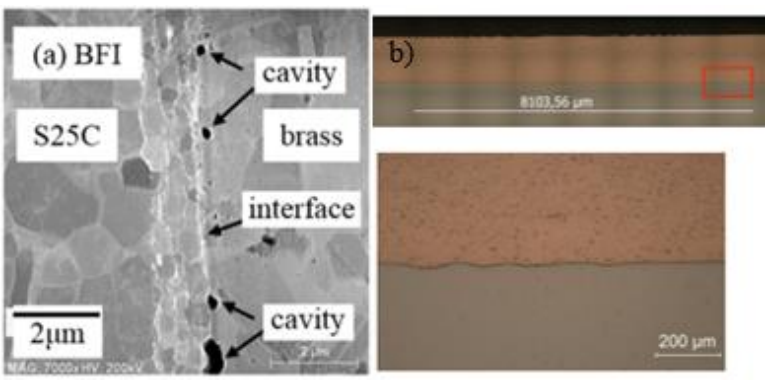

Figure 8 - Defects saw at the interface: a) nano-sized voids and b) lack of joining, adapted [2,5].

Throughout the studies concerning the grain structure of the welds from FSSW and FSW, the material in the SZ experienced dynamic recrystallization resulting in grain refinement. In turn, the grain was elongated in the TMAZ, and grain growth occurred in the HAZ, sometimes being difficult to identify/distinguish these zones.

The microstructure of the FSS welds was found to be influenced by the relative position of the materials in the joint. According to Abdullah and Hussein [48], when the steel was in contact with the tool, the SZ exhibited fine and equiaxed grains. In the TMAZ, the grain was elongated, highly extruded, and upward oriented with non-uniform size. The HAZ grains were affected by the heat generated during the welding process. Nonetheless, when the brass was placed on the top layer, as Barlas [47] studied, recrystallized finer grains of the brass were seen in the SZ, showing a softened SZ with onion rings. Nevertheless, no grain growth was registered at HAZ in the brass due to low heat input. Ferrite matrix and martensite were seen in the SZ of the steel, like the BM.

Regarding FSW works on a lap joint with copper as the top sheet, Martins [2] observed that the SZ was asymmetric and seen only on the copper side with recrystallized grains. The TMAZ with deformed grains and HAZ with grain growth compared to the BM. The SS did not suffer any transformation. However, σ-phase and precipitation of carbides at grain boundaries were seen. The microstructural analysis of copper, performed by Gao et al. [5], showed that at the top of the SZ, the grain size was very small and uniform, and the middle region exhibited a banded structure. At the bottom, an onion ring structure was observed.

For cladding FSW, the typical annealing twins were seen in the SZ, whereas for FSW on a butt joint, the stirring phenomena removed the annealing twins on the steel side [7,50,53].

Concerning FSW works on a butt joint, Fig. 9 shows an example of a microstructure analysis performed by Joshi and Badheka [8]. During FSW on a butt joint, various authors [1,3,7,54] reported that the HAZ of the copper side showed grain growth as opposed to the TMAZ, where there was a refinement in the grain. In turn, Jafari et al. and Joshi and Badheka [8,56] saw that the grain size in the HAZ and TMAZ of copper was larger when compared to the BM. This grain size difference can be seen by comparing Figs. 9a), b), and c) corresponding to the copper's BM, HAZ, and TMAZ.

In the SZ, some authors [3,8,56] reported that both materials experienced grain refinement, and the SZ revealed an intercalated vortex-type microstructure, shown by Figs. 9d), e), and f). Other authors [1,7,54] reported the formation of an SZ consisting of a combination of

copper and dispersed steel particles, with the recrystallization occurring with significant predominance on the copper side with refined equiaxial grains. On the other hand, this prevalence in grain refinement was seen more on the steel side by Wang et al. [3]. The TMAZ in the steel side revealed an elongated grain that has rotated, and the HAZ indicated a similar structure when compared to the BM [1,3,7,54]. Jafari et al. [56] also observed a grain increase in the TMAZ and HAZ of steel, while Wang et al. [32] did not identify a HAZ in the steel. Nevertheless, Joshi and Badheka [8] saw no significant differences between the HAZ and TMAZ when compared to the SS BM, as shown in Figs. 9g), h), and i).

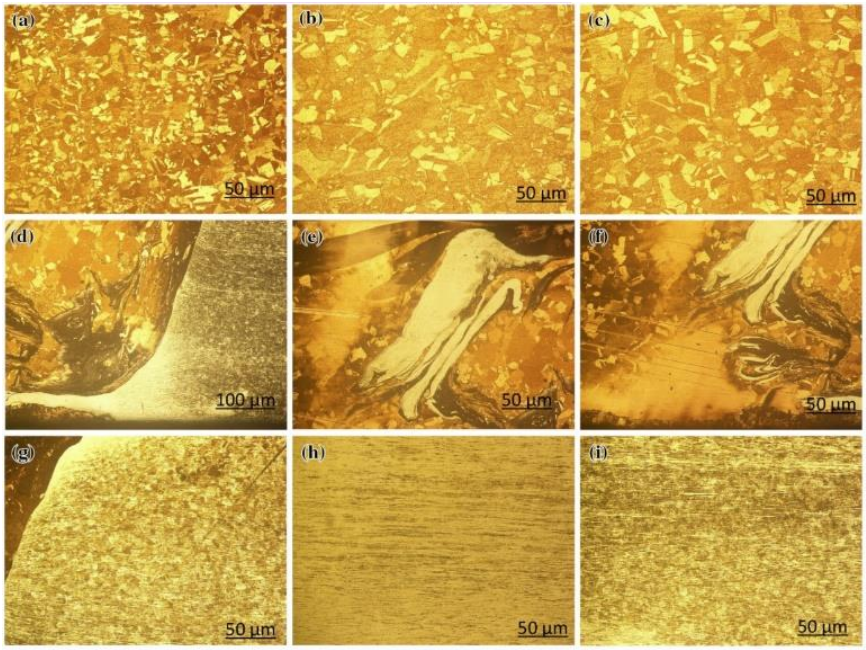

Figure 9 - Microstructural regions in butt FSW: a) Cu BM, b) Cu HAZ, c) Cu TMAZ, d) interface of Cu and SS, e) SZ at the center, f) SZ of Cu top side, g) SS TMAZ, h) SS HAZ, and i) SS BM [8].

Regarding the presence of intermetallic compounds (IMC), varied information for all types of process variants and welded materials were obtained, with some authors reporting the formation of IMC, identified by the X-Ray Diffraction (XRD) tests [1,2,7,8,48,53]. In contrast, others stated that the presence of IMCs was not seen [3,5,50,51,55], with some authors relying on the Cu-Fe phase diagram, which shows in equilibrium conditions the nonexistence of the formation of IMCs. However, the explanation for the presence of IMCs is that no equilibrium conditions are present when executing the welds since the weld is exposed to large deformation and temperature. For FSSW, between copper and carbon steel [48], a good mixing between the materials at SZ was revealed, confirmed by the formation of IMC. In cladding FSW, IMCs were also seen with a small presence near the interface and not detected on the top surface. Fig. 10 shows an example of the XRD analysis to identify

the IMCs, which displays the presence of $Cu_{0.8}Fe_{0.2}$ and $Cu_{0.3}Fe_{1.7}$ intermetallic phases [53]. Other phases were also observed during FSW on a lap joint between copper alloys and SS, such as intermetallic of σ-phase, carbon-chromium-iron, copper-nickel, and austenite of chromium-iron-nickel-iron [1,7,8].

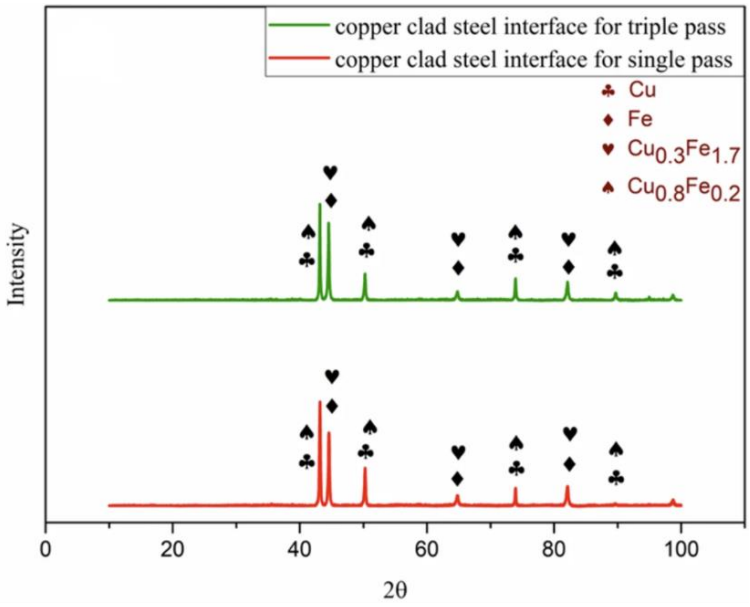

Figure 10 - XRD peaks of transverse cross-section interface indicating the formation of IMCs, adapted [53].

The diffusion evaluation can be obtained with an EDS line scan or mapping analysis, and different observations were made. During FSSW between brass and steel, Ataya et al. [49] observed mutual diffusion of elements at the interface, with Fe, detected on the brass side and Cu and Zn on the steel side. This mutual diffusion was also seen when performing FSW on a lap joint between copper alloys and steel [2,5,51]. On the other hand, the analysis performed by Jafari et al. and Wang et al. [3,56], when performing FSW on a butt joint, revealed that, unlike Fe, Cr, and Cu elements, Ni from steel diffused into the copper side, with only Ni having total solubility in Cu. This solubility for the Ni element is seen in Fig. 11, which shows the EDS analysis on the welded copper/steel interface for Cr, Fe, Ni, and Cu elements. Aval [7] noticed that only diffusion of Cu and Ni from the brass occurred towards the steel between the brass and steel. The EDS quantification performed by Mahto et al. [53] suggested the occurrence of diffusion. However, the micrographs of the interface obtained by Transmission Electron Microscopy (TEM) and the EDS elemental maps revealed a straightforward interface where no Mn or Si could be seen on the copper side of the interface.

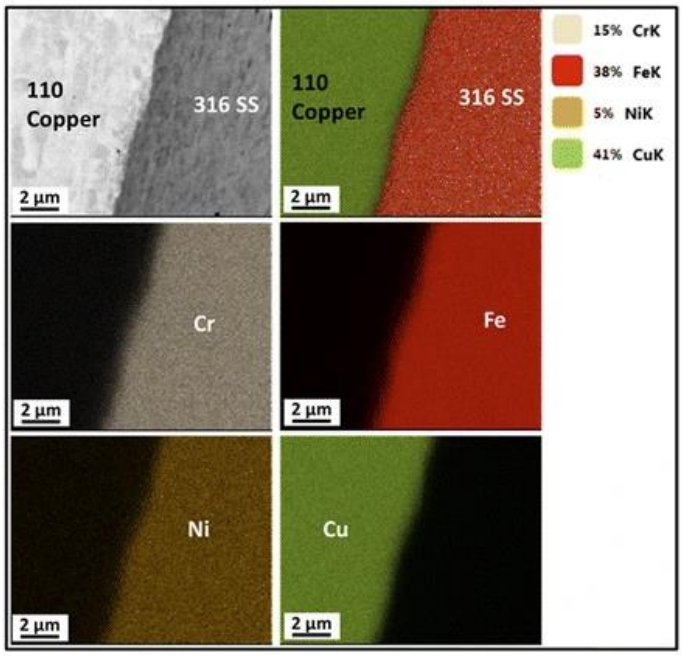

Figure 11 - EDS analysis on welded steel/copper interface [3].

In the study in which an interlayer of Ni was used between the steel and brass sheets, diffusion occurred between the Ni coating and the Cu substrate as well as between the Ni coating and the Fe substrate [52]. The analysis, made by Gao et al. [5], confirming the presence of mutual diffusion is displayed in Fig. 12. Initially, a TEM bright field image was prepared, presented in Figs. 12a) and b), with the EDS element line, Fig. 12c), confirming the existence of mutual diffusion. The only two studies that measured the length of mutual diffusion found that there was a mutual diffusion between Fe and Cu and Zn with similar distances. The first study measured a diffusion over a length of about 80 nm, while the other over a distance between 70 and 120 nm [5,51]. This last case is shown in Fig. 12c).

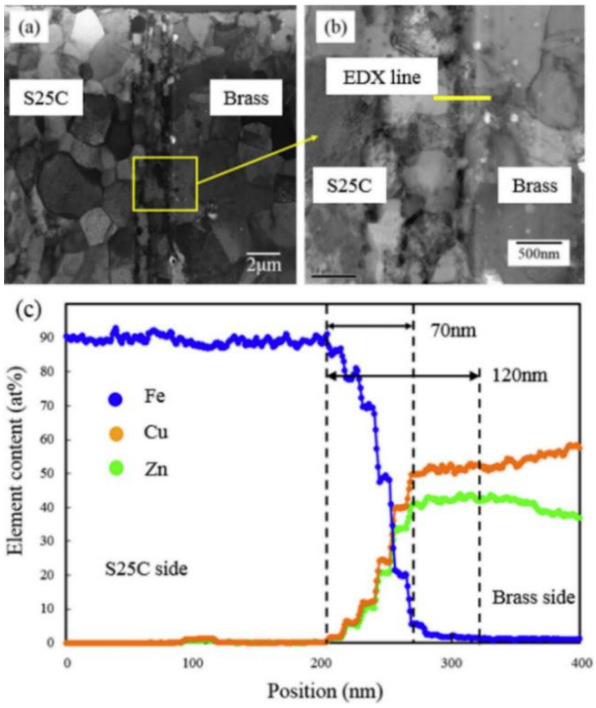

Figure 12 - Interface of a brass-steel FS weld: a) TEM micrograph, b) higher magnification TEM micrograph, and c) EDS element line [5].

2.6. Temperature analysis in Friction Stir Spot Welding and Friction Stir Welding of copper alloys to steel

The temperature is a crucial factor for the production of sound joints, being dependent on the welding parameters and the BMs. Table 3 summarizes the peak temperatures measured for the FSSW and FSW of copper/steel welding. In some cases, the values were not measured, but the temperature information results from microstructural observations, specifically from the metallurgical phenomena whose occurrence has been identified. The maximum temperature measured ranged between 420 and 900 °C, usually measured using a K-type thermocouple positioned at the interface under the tool actuation zone. In the cases where the temperature was obtained based on microstructural observations, the maximum temperature ranged between 650 and 900 °C.

The literature shows that increasing the axial load, rotational speed, welding time, and shoulder diameter raises the temperature until a stabilization temperature is reached. In contrast, the travel speed has the opposite effect [8,47,49,52]. During FSW, Lee et al. (52) found that the increase in dwell time would have more impact on the temperature than a higher rotational speed. In addition, the temperature reached a saturation point (approximately 1000 °C) where rotational speed increments did not raise the temperature.

Table 3 - Peak, interval, or limit temperature register in FSSW and FSW of copper alloys to steel.

Peak Temp. [°C]	Measurement procedure	Measurement zone	Ref.
607	K-type thermocouple	Interface	[47]
583	K-type thermocouple	Interface under the tool actuation zone	[49]
900	K-type thermocouples	Interface at the center of the tool	[52]
650<T<900	Grain boundaries observations		[2]
420	K-type thermocouple	Interface 3 mm away from the center	[5]
T<727	Below critical A1 steel transformation		[50]
550	Laser thermocouples	Weld zone beneath the shoulder	[56]
~750	Thermodynamic calculation phases fractions		[1]
650	K-type thermocouples	Located near the shoulder diameter with a depth of 1.5 mm at both materials	[8]

In FSW and for studies with tool position-controlled, the downward force reduces with the decrease in the travel speed and with the increase in rotational speed as well as with the progression of the weld. This downward force reduction is due to the higher heat input, which softens the material near the tool, leading to some plastic flow with some material being squeezed out [52,56].

2.7. Mechanical properties in Friction Stir Spot Welding and Friction Stir Welding of copper alloys to steel

The assessment of mechanical properties of the spot welds has most commonly been performed based on tensile-shear testing. The results depend on the material properties, joint geometry, and parameters used, as well as on the macro and microscopic features. There is also the opportunity to assess the type of failure and fracture mode. Most researchers have also focused on microhardness measurements in the joints, often reporting higher hardness values for the welds when compared to the BMs because of the formation of highly deformed grains in the TMAZ or refined recrystallized grains in the SZ [11].

2.7.1. Tensile proprieties and fracture surface

FSSW and FSW proved to be effective processes for producing copper/steel welds. Table 4 summarizes the UTS and elongation of the BM, the maximum UTS and elongation, the joint efficiency, the failure types, and the fracture modes obtained in FSSW and FSW. The joint

efficiency is calculated by dividing the weld resistance by the resistance of the least resistant BM. The values shown with the symbol ~ are approximate values taken from published graphs. In two cases, the TSFL is shown due to the absence of the UTS. On the failure type and fracture mode columns, it is highlighted the situation in which the maximum joint efficiency was registered when more than a single type/mode was observed for different welds.

It was possible to achieve a range of 76% to 97% in joint efficiency for the dissimilar welds produced with the different process variants. For some studies, the joint efficiency could not be computed as the authors presented no data regarding the BM properties. Fig. 13 displays the two types of failure found for FSSW: nugget pull-out, Fig. 13a), and interfacial, Fig. 13b). The first failure is caused by plastic collapse, being related to sufficient heat input conditions, and the second one is governed by crack propagation associated to low heat input during welding. Also, in Fig. 13c) is seen an SEM image of the brass fracture surface of a sample that failed by nugget pull-out. The dimples observed in the fracture surface indicate ductile fracture [47,48].

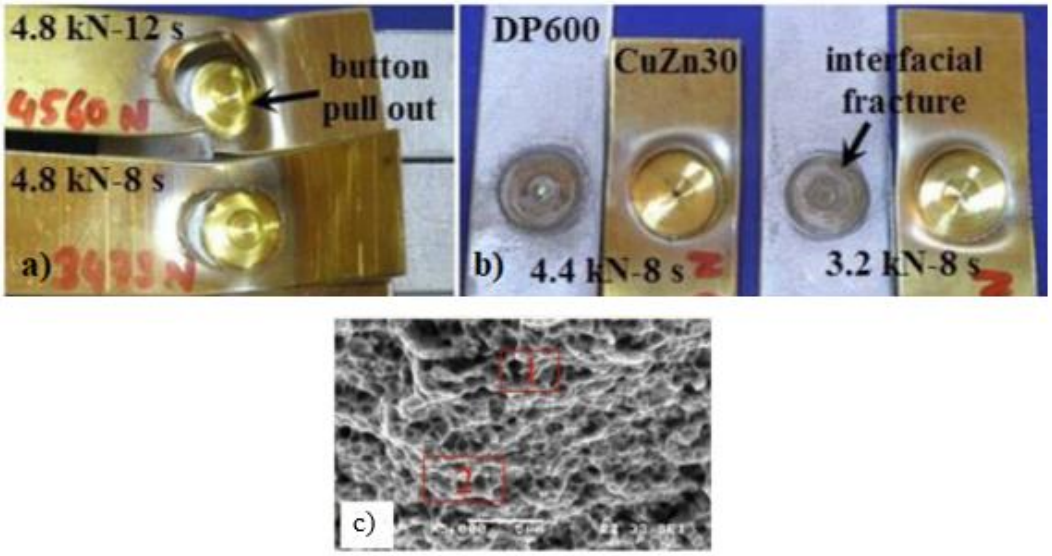

Figure 13 - Failed welds with different failing modes: a) button pull-out, b) interfacial, and c) SEM image of the fractured sample, adapted [47].

The primary failure type for FSW on a lap joint was interfacial within the copper alloy side. According to Sahlot et al. [46], in FSW on a lap joint, the failure occurred by weld debonding under shear load, with dimples visible in the Cu-rich regions and cracks along those dimples in the Fe-rich regions. In turn, Gao et al. [5], in another lap joint, also reported a ductile fracture, but this time, occurring at the brass side near the interface with a fine and uniform dimple pattern and with no significant amount of Fe detected on the fractured surface.

Beyond this, Martins [2] observed that some welds failed in the processing area on the RS of the copper and in the copper BM.

For a butt joint configuration, the most common failure type was at the weld nugget or in the SZ near the interface between materials, with a ductile fracture [3,7,55,57]. In turn, failure at the HAZ of copper was also detected, with both zones of failure (HAZ and SZ) achieving values above 96% of joint efficiency [1,54,56]. The general fracture mode seen was a ductile one since the failure occurred on the copper material in most studies, as confirmed by the SEM images of the fracture zone, making it possible to observe dimples.

Wang et al. [3] achieved the highest joint efficiency, 97%. The authors identified three critical stages of the failure process, including elastic deformation, crack initiation, and crack propagation during tensile testing on a butt joint. The failure path began and grew in the SZ near the interface between the two materials, related to the significant difference in hardness, which led to stress concentration. Aval [7] also observed a fracture in the SZ. However, the fracture mode was hybrid, i.e., it was between a brittle cleavage, revealed by a faceted morphology, and a ductile fracture, exposed by spherical dimples, as shown in Fig. 14. The faceted morphology is explained by the different orientations of the cleavage planes in the grains, while the spherical dimples are related to micro voids starting the crack formation.

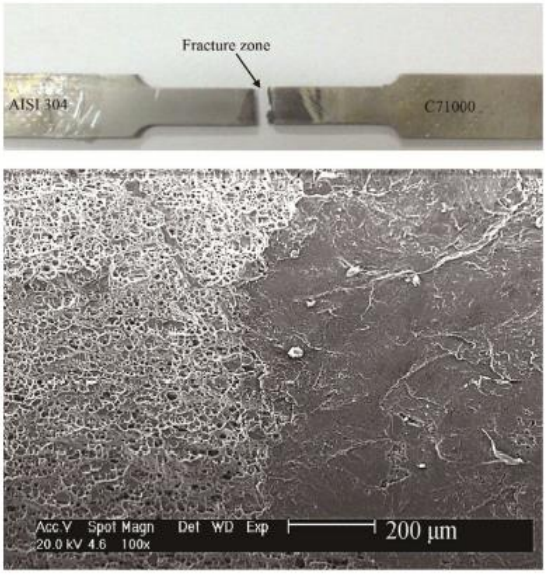

Figure 14 - SEM image of the fracture surface of the joint [7].

Shokri et al. [1] demonstrated that the three fracture modes detected: brittle-ductile, ductile, and brittle, were related to the IMC thickness, which in turn were related to the heat input. Fig. 15 shows the three fracture modes: at the weld nugget, Fig. 15a), at the HAZ Cu alloy,

Fig. 15b), and at the interface line, Fig. 15c), which were registered in welds with small, intermediate, and high IMC thickness, respectively. The trials that failed at the weld nugget (small IMC thickness) revealed a ductile-brittle fracture mode, explained by the low heat input and insufficient material mixing. With the optimum values of heat input, the thickness of the IMC strengthens the weld, while the temperature weakens the copper failing at the HAZ of copper, thus revealing a ductile surface. At the highest IMC thickness, the brittle phase starts to weaken the interface; hence, a brittle fracture was visible at the highest heat inputs.

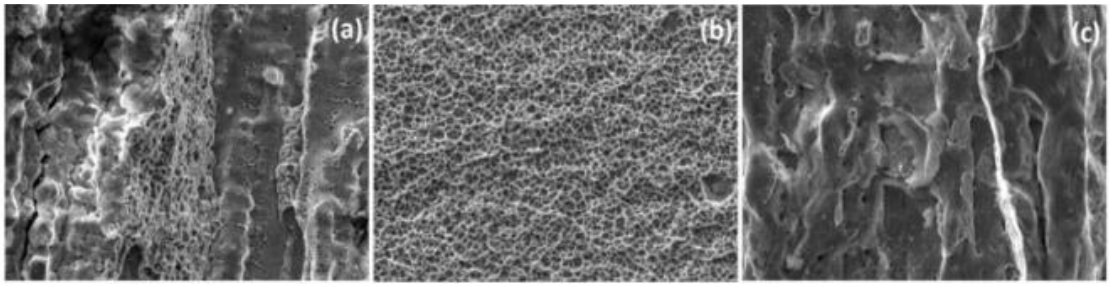

Figure 15 - SEM fractography showing the fracture surfaces: a) the weld nugget, b) the HAZ - copper-alloy side, and c) the interface [1].

The use of Digital Image Correlation by Srinivas [55] allowed the registration of the temporal evolution of localized deformation and enabled the plot of the stress-strain curves for various regions. Using that technique, the area that accounted for 26% of the deformation was the one adjacent to the weld on the copper side, where the actual stress, after an initial rise and fall, constantly increased. At first, the copper near the failure region had practically no elongation, followed by a substantial elongation. The SS region near the weld only accounted for 6% of the elongation, and the region far from the weld presented 1.4% elongation.

Table 4 - BM UTS, maximum UTS obtained, failure type, and fracture mode in FSSW and FSW of copper alloys to steel.

Process and Joint configuration	Workpiece Material, UTS (MPa)/Elongation (%)	Results				Ref.
		Maximum UTS (MPa)/Elongation (%)	Maximum Joint Efficiency (%)	Failure type	Fracture mode	
Probe-less FSSW Lap joint	Carbon steel: 333 Copper: 228 (1 mm)	216	95	Interfacial **Nugget pull-out**		[48]
FSSW Lap joint	Brass Dual-phase steel (1 mm)	TSFL: 4.6 kN		Interfacial **Nugget pull-out**	Ductile	[47]
FSSW Lap joint	Brass: 434 (1 mm) Low carbon steel: 525 (2 mm)	TSFL: 7.5 kN		Nugget pull-out		[49]
Probe-less FSW Lap joint	Copper (3.6 mm) SS (4 mm)	295		**Interfacial debonding brass side** Interfacial Ni coating		[52]
FSW Lap joint	Copper: ~257.44 (1.1 mm) SS: 603 and 623.21 (1 and 6 mm)	~242	94	**On the reverse side of processing copper** Copper BM Interfacial	Ductile	[2]
FSW Lap joint	Brass (3 mm) Plain carbon steel (5 mm)	~141		Interfacial, on the brass side	Ductile	[51]
FSW Lap joint	SS (3 mm) Copper alloy (6 mm)	305		Interfacial	Ductile in Cu-rich areas and cracks along the dimples in Fe-rich	[46]
FSW Butt joint	Copper 261.7 SS: 632 (5 mm)	225.6	85	HAZ copper side	Ductile	[54]
FSW Butt joint	Copper SS (2 mm)	216		Adjacent to the SZ and towards the copper side		[55]
FSW Butt joint	Copper: 273.2/33.54 SS: 557.5/49.3 (3 mm)	217.2/20.7	79	HAZ copper side	Ductile	[56]
FSW Butt joint	Copper: 300 DSS: 520 (4 mm)	279	96	Interface line Weld nugget **HAZ copper side**	Brittle Ductile and brittle **Ductile**	[1]

FSW Butt joint	Copper alloy: 338/32 SS: 585/42 (2 mm)	285/21	84	Weld nugget at the interface of steel and brass	Ductile and brittle	[7]
FSW Butt joint	Copper: ~228 SS: ~661 (6 mm)	~222	~97	SZ copper side adjacent to steel interface	Ductile	[3]
FSSW Butt joint	Copper: 227/23 SS: 682/51 (3 mm)	173/8.2	76	At the interface at the faying surface **Cu side of the nugget**	Mainly ductile with brittle phases	[8]
FSW Butt joint	Copper: 210/20 Plain carbon steel: 355/60 (3 mm)	205/44	97	TMAZ copper side **The middle portion of the nugget**		[58]

2.7.2. Hardness evaluation

Table 5 summarizes the hardness of the BM, the peak hardness registered, the respective location, and the percentage hardness variation obtained in FSSW and FSW of copper alloys to steel. The percentage hardness variation was calculated based on the peaks measured in relation to the values of each BM. The values shown with the symbol ~ are approximate values taken from published graphs. The micro-indentation hardness testing revealed that either for FSSW or FSW, there was a hardness increase of the two materials welded at the SZ due to grain refinement. Nevertheless, it is difficult to identify a dominant profile of hardness evolution across the weld between the different studies.

For FSSW, when evaluating the microhardness, it was possible to observe a softening in the SZ at the upper brass, leading to a reduction in hardness. Nonetheless, a higher value than that of the BM was measured in the onion ring region, which can lead to the belief that the hardness had increased when in reality decreased. As a rule, these regions show more considerable deformation, which generates a more significant number of grain nucleation zones and, consequently, a smaller grain size [47].

For FSW on a lap joint, the material in contact with the tool was more prone to a hardness increase. Martins [2], who worked in lap FSW, performed hardness tests in the center of the processing zone along the thickness of the copper. A general increase in copper hardness is seen in the weld zone due to decreased grain size in that area. Oppositely, in the HAZ, a reduction compared to the BM is noticed due to grain growth. In the SS, when comparing the use of a 1 mm sheet or 6 mm plate, the hardness increased for the thinner one and decreased for the thicker plate compared to the BM. This variation in hardness is associated with the higher formation or practically non-existent sigma phase for the 1 mm sheet and the 6 mm plate, respectively. The copper's horizontal hardness profile is illustrated in Fig. 16. Gao et al. and Mahto et al. [5,53] also performed horizontal hardness profiles in FSW lap joining and cladding FSW, respectively, reporting similar variations to the copper hardness.

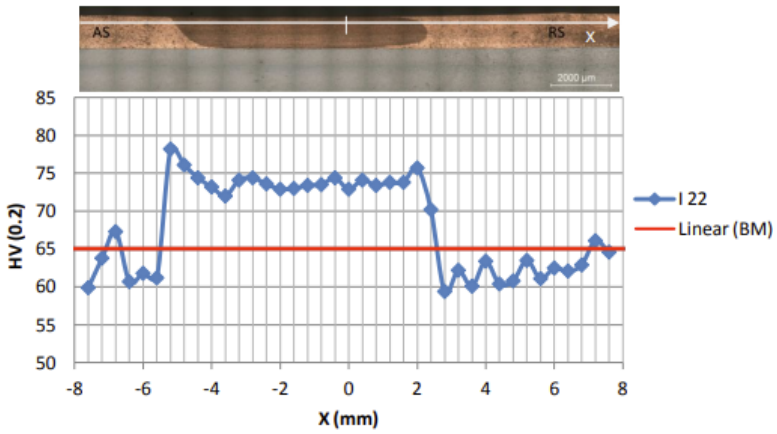

Figure 16 - Evolution of the horizontal hardness profile on copper [2].

By performing a clad FSW between a copper sheet on a steel substrate, Shen et al. [50] saw that the hardness continuously increased through-thickness from the steel side until the interface. On the copper side, the hardness slightly increased compared to the BM. In another approach, but again cladding copper on a steel substrate, Mahto et al. [53] evaluated the hardness in the transverse cross-section, specifically in two zones, i.e., near the top surface and close to the interface for both copper and steel sheets. For a single pass, the copper hardness was similar to that of the BM, both near the interface and the top surface, with no major variations throughout the profile. At the same time, the mild steel showed a decrease in hardness, and compared to copper, the mild steel showed a more significant variation throughout the profile near the SZ, while a uniform and even lower hardness was noticed in the HAZ. For double-pass and triple-pass cladding, no remarkable variation of hardness for copper was registered; however, a successive reduction in hardness was noticed for the mild steel.

In the case of a butt configuration, a general increase at the SZ was visible, with some studies revealing hardness peaks in the copper side created by some steel fragments or the presence of IMCs. The average percentual increase in hardness among the FSW studies is higher for butt joining than for lap configuration, where two studies reached more than 100% in hardness compared to the steel BM.

A microhardness reduction compared to the BM was registered in the HAZ of copper due to coarsening of precipitates and grain growth [1,3,54,56]. In the TMAZ of copper, microhardness was slightly higher than in the HAZ but lower than in the SZ [3,56]. The SZ showed an increased hardness for each material [1,7,32,54–56]. In two studies, the steel and copper registered a hardness decrease in the regions adjacent to the SZ [54,55].

Concerning the copper in the SZ, Wang et al. [3] affirmed that the copper suffered both from grain boundary strengthening contribution due to grain refinement and loss of strength due to thermal softening. At the same time, the existence of steel fragments in SZ increased hardness locally. When a higher travel speed was used, higher hardness values were obtained; when a low travel speed was used, thermal softening was the main factor, reducing hardness. Aval [7] registered that the SZ on the brass side had a more uniform hardness profile, gradually decreasing to the level of the BM by moving away from the SZ.

Regarding the steel, Aval [7] visualized that as moving closer to the interface, the hardness fluctuated in that area due to the layer-by-layer structure present, producing a non-uniform hardness profile and stress concentration zones. The hardness of the TMAZ and HAZ of steel remained constant and similar to BM. Shokri et al. [1] also registered an equivalent value in the TMAZ compared to BM. However, with a decreased hardness value in the HAZ of SS. With different results in TMAZ of steel, Najafkhani et al. and Wang et al. [3,54] revealed a hardness increase explained by work hardening without reference to a HAZ.

The hardness of dissimilar joints for additional heating and cooling relative to normal FSW, performed by Joshi and Badheka [57], showed that the highest hardness was noted for the normal FSW. In another study [8], the same authors compared the hardness registered in welds produced with four different shoulder diameters, from 16 to 22 mm. It was concluded that the 20 mm tool gave rise to variations in microhardness on the Cu side due to steel fragments in the SZ, with the hardness measurements remaining likely uniform for the 18 and 22 mm, without variation in the SS side. Due to the higher presence of IMCs and precipitates, the maximum hardness was reported for the 20 mm tool. A similar approach was studied by Gao [51], but this time on a lap joint, concluding that hardness decreased either when using a tool with the same shoulder diameter but increasing the probe diameter or when using the same probe diameter and increasing the shoulder diameter.

Table 5 - BM Hardness, hardness peak, and location in FSSW and FSW of copper alloys to steel.

Process and Joint configuration	Workpiece material and Hardness (HV)	Hardness Peak (HV)	Documented peak hardness location	Variation to BM (%)	Ref.
FSSW Lap joint	Brass: 149.1 Dual-phase steel: 228.6 (1 mm)	Onion ring: 165.8 Brass: 129.8	Onion rings in the SZ Generalized hardness reduction at SZ	Onion ring area: 11.20 Brass: -12.94	[47]
FSSW Lap joint	Brass: 128 (1 mm) Carbon steel: 223 (2 mm)	Bass: 163 Steel: 262	Brass: peripheric to the probe-hole still in the SZ Steel: SZ center	Brass: 27.34 Steel: 17.49	[49]
FSW Lap joint	Copper: 65.07 (1.1 mm) SS: 184.58 (1 and 6 mm)	Copper: ~81.5 SS: ~211.5	Copper: peripheral to the probe-hole SS: Nugget zone	Copper: ~25.25 SS: ~14.58	[2]
FSW Lap joint	Brass: ~105 (3 mm) Plain carbon steel (5 mm)	Brass: ~153	SZ	Brass: ~45.71	[5]
FSW Lap joint	Brass: ~105 (3 mm) Plain carbon steel (5 mm)	Brass: ~146	SZ	Brass: ~39.05	[51]
FSW Lap joint	SS: 177 (3 mm) Copper: 94 (6 mm)	SS: ~300 Copper: ~121	SZ at the interface	SS: ~69.49 Copper: ~28.72	[46]
Cladding FSW Lap joint	Copper: 70 (2.1 mm) Structural carbon steel: 155 (25.4 mm)	Copper: ~70 Steel: ~199	SZ at the interface	Copper: 0 Steel: ~28.39	[50]
Cladding FSW Lap joint	Copper: 115.1 (3 mm) Mild steel: 335.8 (6 mm)	Copper: 124.6 Steel: 297.0	SZ at the interface	Copper: ~8.25 Steel: ~ -11.55	[53]
FSW Butt joint	Copper: ~68 SS: ~205 (5 mm)	SS: ~287	TMAZ SS	SS: ~40	[54]
FSW Butt joint	Copper: ~89 SS: ~159 (2 mm)	SS: ~264	Near the weld zone on the SS side	SS: ~66.04	[55]
FSW Butt joint	Copper: ~72 SS: ~148 (3 mm)	~256	Weld region	~72.97	[56]
FSW Butt joint	Copper: ~117 DSS: ~311 (4 mm)	SS: ~314	TMAZ SS	SS: ~0.96	[1]
FSW Butt joint	Copper alloy: 90 SS: 152 (2 mm)	~180	SZ	~18.42	[7]

FSW Butt joint	Copper: ~77 SS: ~186 (6 mm)	~390	SZ	~109.68	[3]
FSSW Butt joint	Copper: ~55 SS: ~200 (3 mm)	~412.7	SZ	~106.35	[8]
FSW Butt joint	Copper: 50 Plain carbon steel: 108 (3 mm)	~140	Nugget zone	~29.63	[58]

3. Experimental procedure

3.1. Material characterization

In this study, the following materials were used: Cu-DHP copper alloy and AISI 304 SS, with 1 mm of thickness each. Tables 6 and 7 show the chemical composition and the physical and mechanical properties of the alloys, respectively. In Table 7, the use of the symbol * means that the value was experimentally obtained in this study. Significant differences can be depicted from the information displayed in these tables. In fact, besides the evident discrepancy in chemical composition, relevant differences in thermal conductivity are also noticeable.

Table 6 - Chemical compositions of AISI 304 SS and Cu-DHP (wt.%) [59,60].

AISI 304 SS	C	Cr	Mn	Si	P	S	Ni	N	Fe
	0.08	18.5	1.5	0.6	-	-	10	-	Bal.
Cu-DHP	Cu	Bi	Fe	O	P	Pb	Sn	Zn	Others
	≥99.9	-	-	-	0.02	-	-	-	Bal.

Table 7 - Physical and mechanical properties of AISI 304 SS and Cu-DHP.

Physical and Mechanical Properties	AISI 304 SS [59]	Cu-DHP [60]
Density [g/cm^3]	8.0	8.94
Melting point [°C]	1400-1450	1083
Specific heat [J/kg·K]	500 at 20 °C	385 at 20 °C
Elastic modulus [GPa]	193	115
Thermal conductivity [W/m·K]	16.2 at 100 °C 21.5 at 500 °C	350 at 20 °C
Coefficient of thermal expansion [10^{-6}/K]	17.2 at 0-100 °C 17.8 at 0-315 °C 18.4 at 0-538 °C	17.0 at 20-100 °C 17.3 at 20-200 °C 17.7 at 20-300 °C
Hardness [$HV_{0.2}$] *	177.7	81.9
Yield strength [MPa] *	255.2	182.9
UTS [MPa] *	677.4	250.0

3.2. Welding Process

Initially, all the BM sheets were cut from the original copper and SS sheets by a mechanical guillotine, with a dimension of 100x100 mm. The welds were then performed in the workshop of the Department of Mechanical Engineering of the University of Coimbra with a conventional milling machine, Cincinnati Milacron 207MK.

A tool composed of two parts was used: body + shoulder-probe system. The body was made of H13, and the shoulder-probe system was made of WC. The tool used is characterized as a featureless flat tool, corresponding to probe-less FSSW. Also, two shoulders with different diameters were used, 10 and 12 mm, labeled SP10 and SP12, respectively. The whole tool is represented in Fig. 17, where Figs. 17a) and b) correspond to the SP12 and SP10 tools.

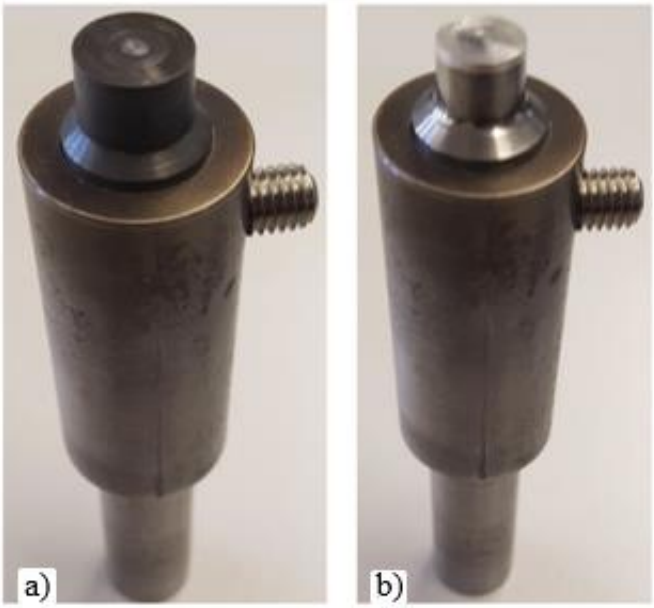

Figure 17 - FSSW probe-less tool: a) SP12 and b) SP10.

The fixture system is an essential part of obtaining good welds. The clamps are used to counter the welding tool force, the workpiece curving due to thermal expansion, to prevent the workpieces from sliding, and to press the sheets against one another [2,61].

In this study, the definition of the fixture system was an iterative process, given the observations throughout the production of the welds. Fig. 18 shows the evolution of the three types of fixture systems used: a double-point clamping system (Fig. 18a)); a double-point clamping system with an additional third point, opposite and centered (Fig. 18b)); a triple-point clamping system (Fig. 18c)). These three types of fixtures are labeled as DP, DPTP, and TP, respectively.

Figure 18 - Types of fixture system: a) double-point clamping system, b) double-point clamping system with a third point using pliers, and c) triple-point clamping system.

Table 8 displays the complete set of welding conditions considered in this study, where two different tool diameters, two material positions in the joint, three rotational speeds, two welding times, and two plunge depths were tested, thus obtaining 16 test conditions. In addition to the 16 tested conditions, 18 more welds were executed with specimens of different dimensions (105x45 mm) for the tensile-shear test. The fixture system used is also displayed in Table 8. All trials with a SS/Cu material position at the interface were sanded. For all the welds using the SP10 tool, the start of the welding time count was made at the moment when the intended penetration was reached. The nomenclature used to label the welds is defined by the tool, material position in the joint, rotational speed, welding time, and penetration. For example, the designation SP10-Cu/SS-870-20-0.8 comes from welding with the tool SP10, with copper being the top material, with a rotational speed of 870 rpm, a welding time of 20 s, and a tool penetration of 0.8 mm.

Table 8 - Welding parameters/conditions used to produce the welds.

Welds	Tool	Material Position	Rotational speed (rpm)	Welding time (s)	Penetration (mm)	Fixture system
SP10-SS/Cu-870-20-0.8	SP10	SS/Cu	870	20	0.8	TP
SP10-SS/Cu-870-60-0.8		SS/Cu	870	60	0.8	TP
SP10-SS/Cu-1140-20-0.8		SS/Cu	1140	20	0.8	TP
SP10-SS/Cu-1140-60-0.8		SS/Cu	1140	60	0.8	TP

SP10-SS/Cu-1500-20-0.8		SS/Cu	1500	20	0.8	TP
SP10-SS/Cu-1500-60-0.8		SS/Cu	1500	60	0.8	TP
SP12-SS/Cu-870-20-0.8	SP12	SS/Cu	870	20	0.8	TP
SP12-SS/Cu-870-60-0.8		SS/Cu	870	60	0.8	TP
SP12-SS/Cu-1140-20-0.8		SS/Cu	1140	20	0.8	TP
SP12-SS/Cu-1140-60-0.8		SS/Cu	1140	60	0.8	TP
SP12-SS/Cu-1500-20-0.8		SS/Cu	1500	20	0.8	TP
SP12-SS/Cu-1500-60-0.8		SS/Cu	1500	60	0.8	DPTP
SP12-Cu/SS-1500-60-0.8		Cu/SS	1500	60	0.8	DPTP
SP12-Cu/SS-870-20-0.8		Cu/SS	870	20	0.8	DP
SP12-Cu/SS-870-60-0.8		Cu/SS	870	60	0.8	DPTP
SP12-Cu/SS-870-60-1		Cu/SS	870	60	1	DP

The temperature measurements were made with a K-type thermocouple, using the High-Precision Thermocouple USB Device DT9828 for the data translation. This device was connected to a computer via USB, where the QuickDAQ software did the data logging for further analysis. For the placement of the thermocouple, a 2 mm diameter hole was drilled, 5 mm away from the extremity of the shoulder, as displayed in Fig. 19. The hole depth coincides with the thickness of the upper sheet, whereby the thermocouple stayed positioned at the interface of the two sheets. Regardless of the material position (SS/Cu or Cu/SS), the thermocouple placement was always done through the hole in the copper.

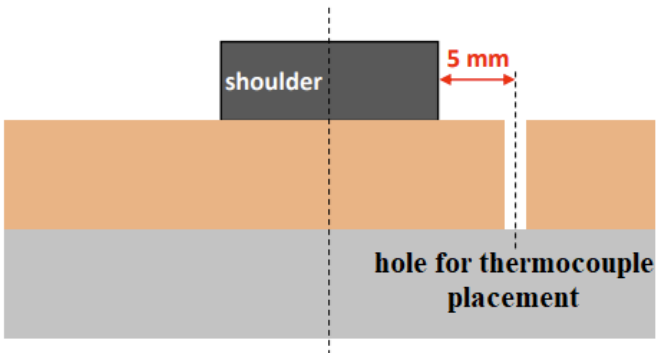

Figure 19 - Schematic representation of the placement of the thermocouple.

Due to the high-frequency data acquisition, the data displayed high noise, and a smoothing technique was used to minimize the noise and better read the data. The graph in Fig. 20, which shows the temperature evolution with the welding time, is an example of the treated temperature data. The software used for the signal processing was OriginPro, obtaining a smooth curve using the Fast Fourier Transform (FFT) filtering method. The parameters used

for the FFT filtering were five points of window and a cut-off frequency automatically determined by the software.

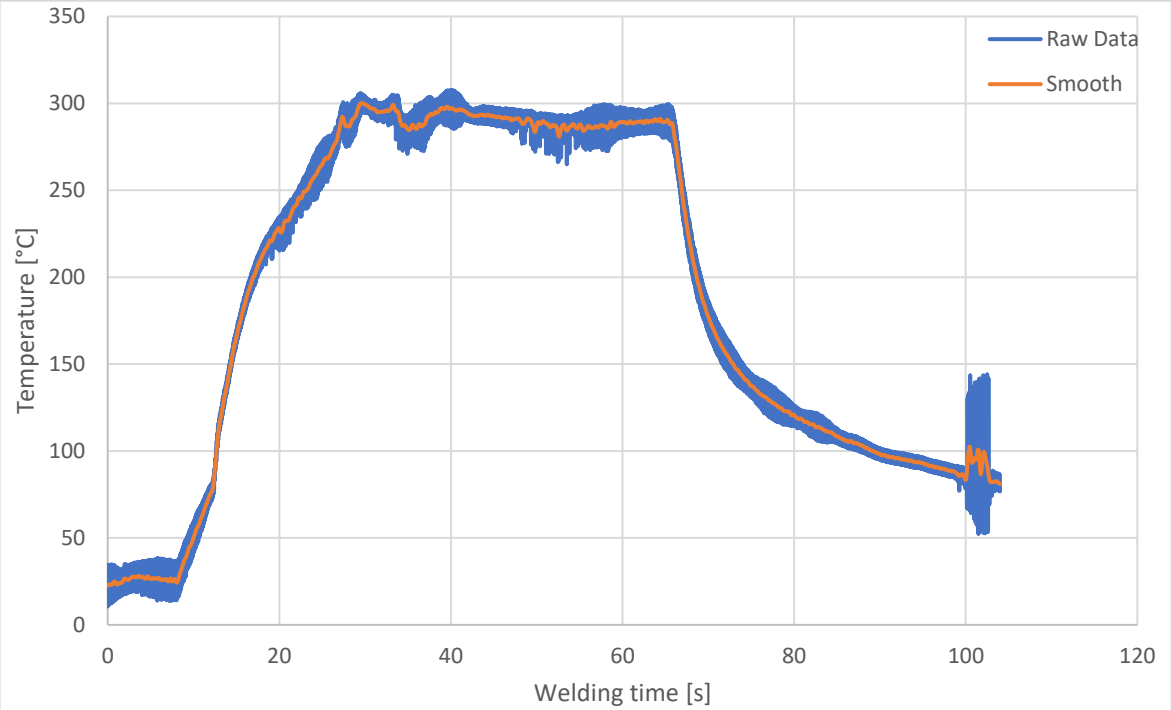

Figure 20 - Raw temperature curve and smoothed curve.

3.3. Characterization techniques

3.3.1. Visual inspection

The first phase of the characterization of the trials consisted of their visual inspection. The surface of each weld was analyzed in detail and photographed.

3.3.2. Metallographic analysis

A material sample illustrating the cross-section of the bonding area was taken from each weld, having been embedded in resin. These welds were subjected to the action of four different granulometric grades of sandpaper, 320, 600, 1000, and 2500. The finish was obtained from a diamond suspension of 6, 3, and 1 μm. The trials were then subjected to chemical etching, with the copper being etched with a solution of 5 ml of H_2O_2 in 50 ml of NH_4OH. The etching time was variable and could not be generalized. Several attempts were made until the attack was the one that offered the best observation conditions. The trials were observed under the Leica DM4000M LED OM, displayed in Fig. 21, with magnifications of 50x, 100x, 200x, 500x, and 1000x and micrographs were then taken.

Figure 21 - Leica DM4000M LED OM.

3.3.3. SEM analysis

The cross-section welds used for the metallographic analysis, together with horizontal section welds, referring to the region of the welding interface where there was no material bonding, were analyzed by SEM using the Hitachi SU3800 equipment, Fig. 22.

Figure 22 - Hitachi SU3800 scanning electron microscope.

3.3.4. EDS analysis

The elemental chemical composition of the welds was performed by EDS, using the system coupled to the Hitachi SU3800 SEM, which is highlighted in yellow in Fig. 22. This analysis focused, essentially, on the bonding interface region, both in the cross-section and the horizontal section samples.

3.3.5. Hardness test

Vickers microhardness tests were conducted using an LTF SpA GALILEO ISOSCAN OD-Automatic Microhardness Tester (Fig. 23). The indentations were performed along the weld cross-section, perpendicularly to the thickness of the samples, under a load of 200 g, with a dwell time of 15 s, spaced 0.5 mm from each other, for both welded materials. The hardness profiles were taken at an average distance of 0.25 mm from the interface. Transverse indentations (along the thickness of the samples) were also performed in the center of the welds at a distance of 0.15 mm from each other. The software ZEN core was used to measure the indentation diagonals.

Figure 23 - GALILEO ISOSCAN OD - Automatic Microhardness Tester.

3.3.6. Tensile-Shear test

The tensile tests were performed on a universal tensile testing machine, Shimadzu AGS-X 100 kN, presented in Fig. 24, using a deformation speed of 5 mm/min. The clamps used for the tensile test belong to the [0–6] mm class. The welding process was repeated for each trial where bonding was achieved, obtaining three tensile specimens per condition (18 specimens in total) to perform the analyses. The specimens were obtained according to the standard ISO 14273:2016, i.e., with 105x45 mm in dimension and an overlap length of 35 mm.

Figure 24 - Shimadzu AGS-X 100 kN universal tensile testing machine.

4. Results and Discussion

4.1. Visual observation

Initial attempts to perform FSSW and FSW of copper alloys to steel showed that welds could be generated using appropriate welding parameters. Table 9 shows all the trials, identifying the ones in which it was or was not achieved weld/interfacial bonding. Some remarks are gathered from the observations made during and after the welding process. For the given experimental layout, it was possible to achieve successful welding trials; specifically, six consistent welds were produced in a total of 16 trials. None of the trials performed with copper as the top plate led to the production of consistent welds. On the other hand, some SS/Cu trials presented consistency after the process.

Table 9 - Welding results.

Welds	Interfacial bonding	Remarks
SP10-SS/Cu-870-20-0.8	Achieved	Initial welding created burrs of SS
SP10-SS/Cu-870-60-0.8	Not Achieved	Indentation of the weld by one of the fixing points;
SP10-SS/Cu-1140-20-0.8	Not Achieved	
SP10-SS/Cu-1140-60-0.8	Achieved	Mushroom effect on tool
SP10-SS/Cu-1500-20-0.8	Achieved	
SP10-SS/Cu-1500-60-0.8	Achieved	
SP12-SS/Cu-870-20-0.8	Not Achieved	
SP12-SS/Cu-870-60-0.8	Not Achieved	Initial bonding was achieved
SP12-SS/Cu-1140-20-0.8	Not Achieved	
SP12-SS/Cu-1140-60-0.8	Achieved	
SP12-SS/Cu-1500-20-0.8	Not Achieved	
SP12-SS/Cu-1500-60-0.8	Achieved	Mushroom effect on tool; bending of the weld side with the plier
SP12-Cu/SS-1500-60-0.8	Not Achieved	
SP12-Cu/SS-870-20-0.8	Not Achieved	Initial welding created burrs of copper
SP12-Cu/SS-870-60-0.8	Not Achieved	
SP12-Cu/SS-870-60-1	Not Achieved	Bending of the copper on the unfixed side

All the trials, with copper or SS as the top sheet, showed a shining surface produced by the tool shoulder, leaving a slight indentation without a probe-hole, minimal flash, and no major visible defects. In addition, color changes surrounding and in the shoulder actuation zone

were observed. This phenomenon is seen due to the heat input, which shows different tempering colors due to the oxide layer formation, identifying the evolution of heat propagation.

Fig. 25 shows the formation of burrs for the SP12-Cu/SS-870-20-0.8 and SP10-SS/Cu-870-20-0.8 trials, having been the first two welds performed with each tool. This formation only occurred with extraordinary evidence in these two welds as the tool started cold before the welding and the shoulder's edge was sharper compared to the progression of the welds.

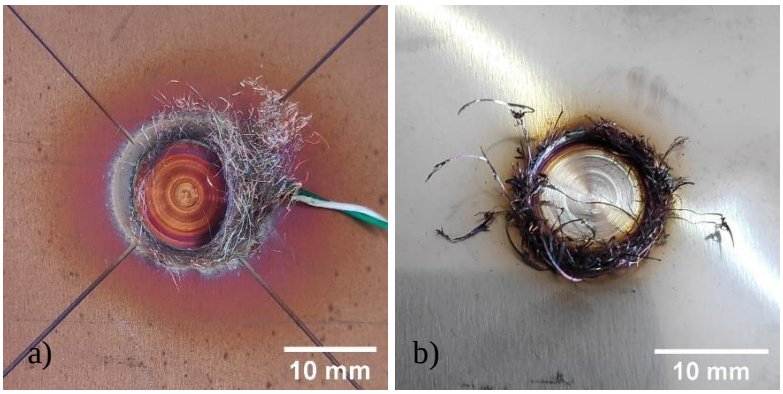

Figure 25 - Burrs formation: a) SP12-Cu/SS-870-20-0.8 and b) SP10-SS/Cu-870-20-0.8.

Fig. 26 illustrates the weld surface (Fig. 26a)), weld bottom (Fig. 26b)) and weld interface (Fig. 26c)) for the SP12-Cu/SS-1500-60-0.8 trial, which was performed with the Cu/SS material position; therefore, bonding was not achieved. A change of color with a circumferential format and a trend to spread to the unfixed side is seen in Fig. 26a). This effect was more prominent when the combination of high parameters and DP or DPTP fixture system was used. This combination allowed the bending of the copper or the material pair, depending on the system used, on the unfixed side, exposing the weld more to the environment, which has lower conductivity than SS, allowing a lesser heat dissipation and increasing the temperature in that area. Another explanation, created again by the bending of the weld, is that the trial may not be fully parallel to the tool, which can create additional pressure, generating more heat on that side. The area affected by this color change is broader and more intense with the increase in rotational speed, penetration, and welding time, which can be observed by comparing Figs. 26a) and 25a) since more heat is generated and applied during more time to the material.

On the other hand, the SS revealed minimal visible morphological or color change on the weld bottom, as shown in Fig. 26b). With a noticeable circumference similar to the size of the tool diameter at the interface, shown in Fig. 26c). This minimal SS change remained similar between the trials with this material position. Still, an embossed copper feature at the

bottom of the top plate is displayed in the weld interface, as seen in Fig. 26c). This phenomenon was also seen in the other trials with this material position. This effect may result again from the DPTP or DP fixture system, which allowed a clearance between the copper and SS to be created. This effect, combined with the material ductility, provides the conditions for the appearance of this phenomenon.

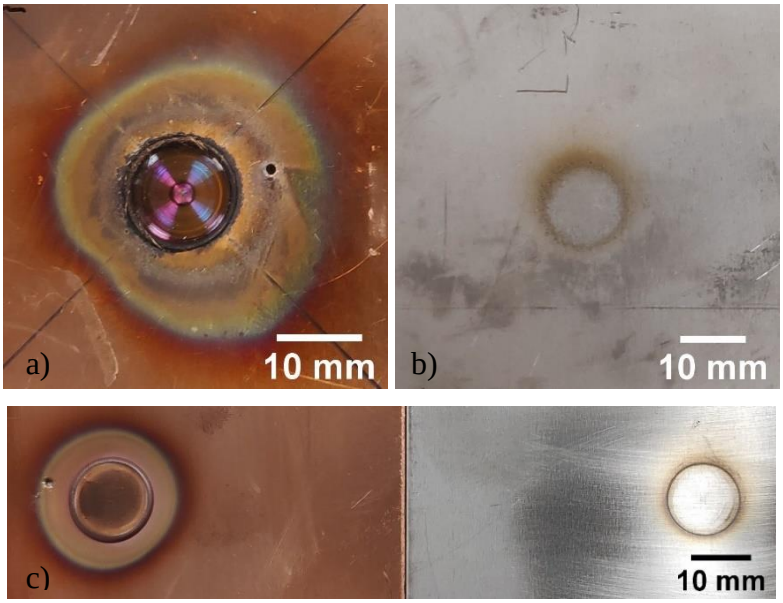

Figure 26 - SP12-Cu/SS-1500-60-0.8 trial: a) surface weld, b) bottom weld, and c) interface.

With the change of SS to the top plate and using the SP12 tool, it was possible to achieve two successful welds, the SP12-SS/Cu-1140-60-0.8 and SP12-SS/Cu-1500-60-0.8. Fig. 27 shows in the rows the weld surface, bottom, and interface (if not welded) of the SP12-SS/Cu-870-20-0.8, SP12-SS/Cu-1500-20-0.8, and SP12-SS/Cu-1500-60-0.8 trials, being the welds identified in their respective column. The area affected by the color change is again more considerable with the increase in rotational speed and welding time. This color difference is confirmed by comparing the welds illustrated in Fig. 27. At the weld surface of SS, these welds show a minimal area color change for the lowest parameters used (SP12-SS/Cu-870-20-0.8) and a more extensive area with the highest parameters used (SP12-SS/Cu-1500-60-0.8). However, this color change is more influenced by the welding time. If the welds SP12-SS/Cu-870-20-0.8 and SP12-SS/Cu-1500-20-0.8 are compared in Fig. 27, a very slight area increase from 870 to 1500 rpm is seen. Unlike this, the color change between SP12-SS/Cu-1500-20-0.8 and SP12-SS/Cu-1500-60-0.8, where the welding time is increased by 40 s, is more evident since the affected area is more extensive and darker.

The weld bottom on all these welds features an evident morphological change, with more or less intensity, influenced by the welding time and accompanied by a color change

peripherical to this morphological change. The SP12-SS/Cu-1500-60-0.8 weld was the only trial where the DPTP fixture system was used, showing the extreme situation where the area of color change in the copper bottom propagates in only one direction to the unfixed side. This observation is explained by the reasons pointed out for the welds using a Cu/SS position. As for the interface, it shows a minimal visible morphological and color change for the lowest parameters used, shown by the trial SP12-SS/Cu-870-20-0.8, that intensifies for the other welds interface with a darker appearance for copper and a small peripheral dark color change on SS, as shown by the SP12-SS/Cu-1500-20-0.8 trial.

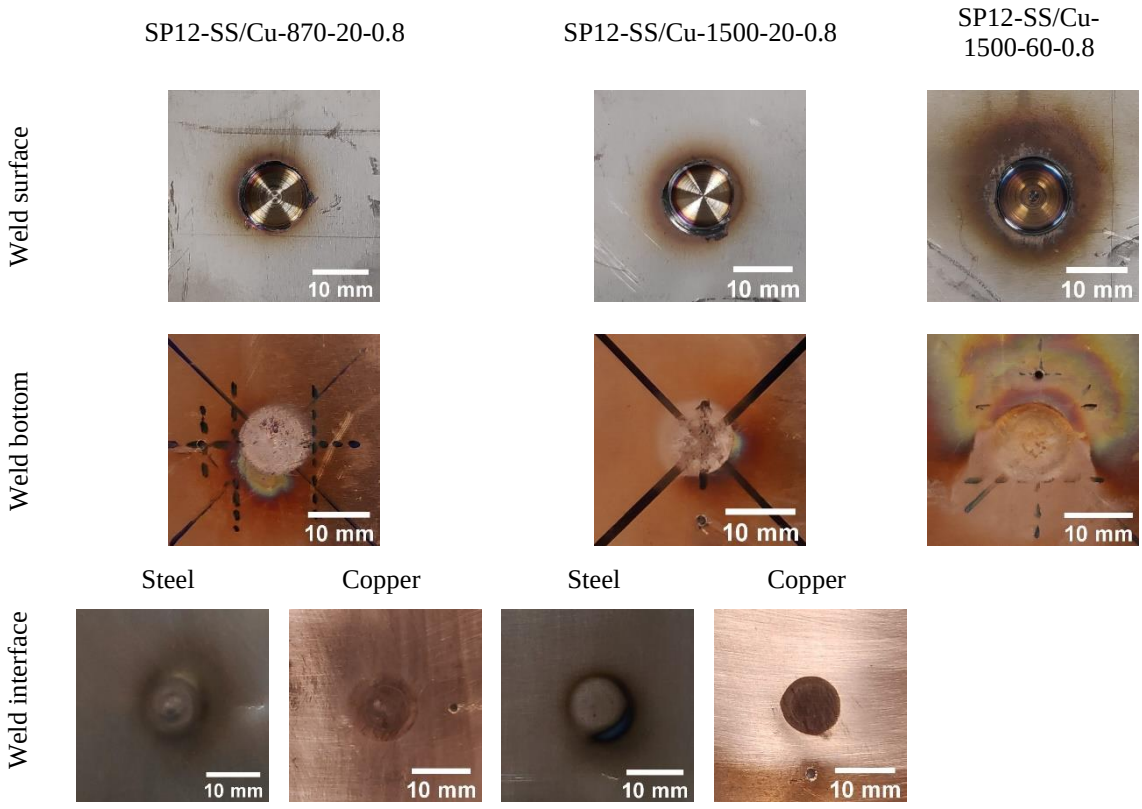

Figure 27 - Weld surface, bottom, and interface from SP12-SS/Cu-870-20-0.8, SP12-SS/Cu-1500-20-0.8, and SP12-SS/Cu-1500-60-0.8 welds.

With the tool change for the SP10, it was possible to achieve four successful welds. Fig. 28 shows, once again, the weld surface, bottom, and interface (if not welded) of the SP10-SS/Cu-870-60-0.8, SP10-SS/Cu-1140-20-0.8 and SP10-SS/Cu-1500-60-0.8 trials. All the trials have similar characteristics compared to the welds in which the SP12 tool was used; therefore, similar conclusions can be drawn as those previously described for that tool. When analyzing the only two trials with the SP10 tool for which welding was not achieved, SP10-SS/Cu-870-60-0.8 and SP10-SS/Cu-1140-20-0.8 in Fig. 28, a convex and concave shape for the SS and copper was seen at the interface, respectively. SP10-SS/Cu-870-60-0.8 even

shows an indentation of the fixture system, leading to a possible non-flat contact at the interface, justifying why it was the only weld where the copper morphological change was minimal compared to the other trials.

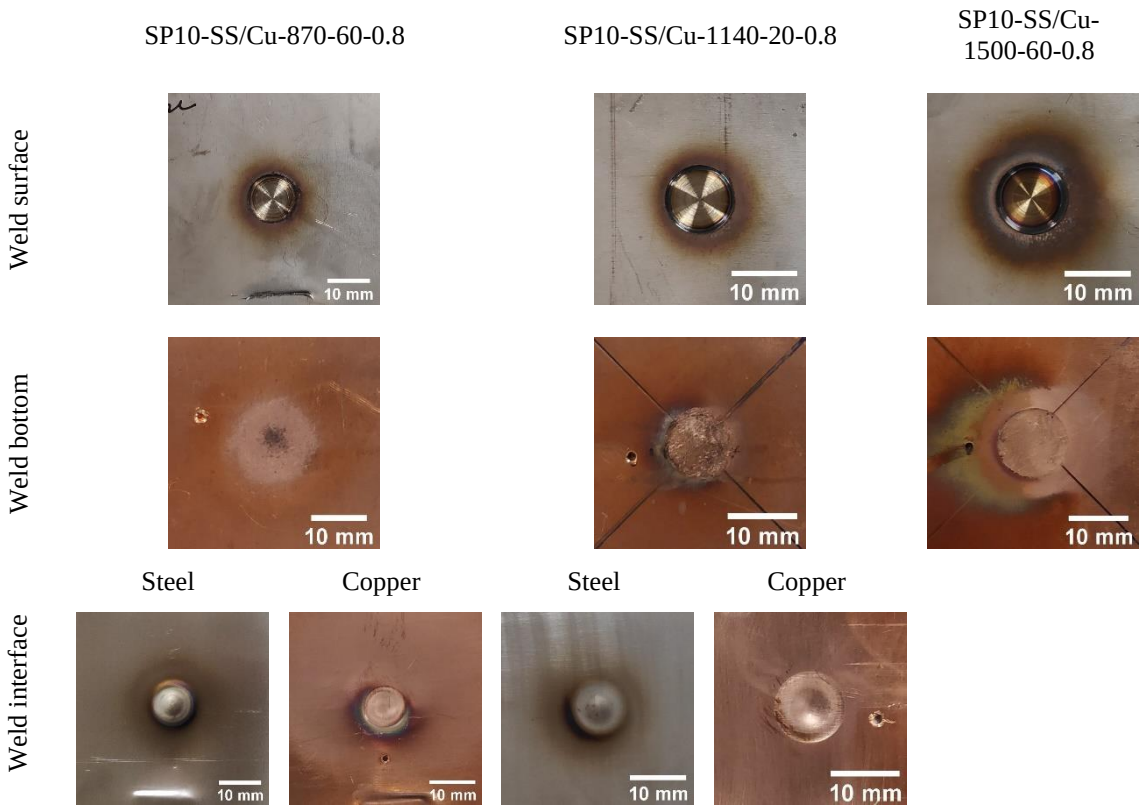

Figure 28 - Weld surface, bottom, and interface from SP10-SS/Cu-870-60-0.8, SP10-SS/Cu-1140-20-0.8, and SP10-SS/Cu-1500-60-0.8 welds.

With the change in the material position from Cu/SS to SS/Cu, it was possible to observe some effects on the tool, as illustrated in Fig. 29. The tool exhibited incandescence, Fig. 29a), being a clear fact of the different thermal conductivities of copper and SS. Moreover, the change in the position of the plates enhanced the occurrence of the mushroom effect in the tool, visible in Fig. 29b), which was observed with great intensity for the SP12-SS/Cu-1500-60-0.8 and SP10-SS/Cu-1140-60-0.8 welds. A bending effect is also visualized in Fig. 29a), which was already referred to explain the color change evolution, showing the importance of a suitable fastening system.

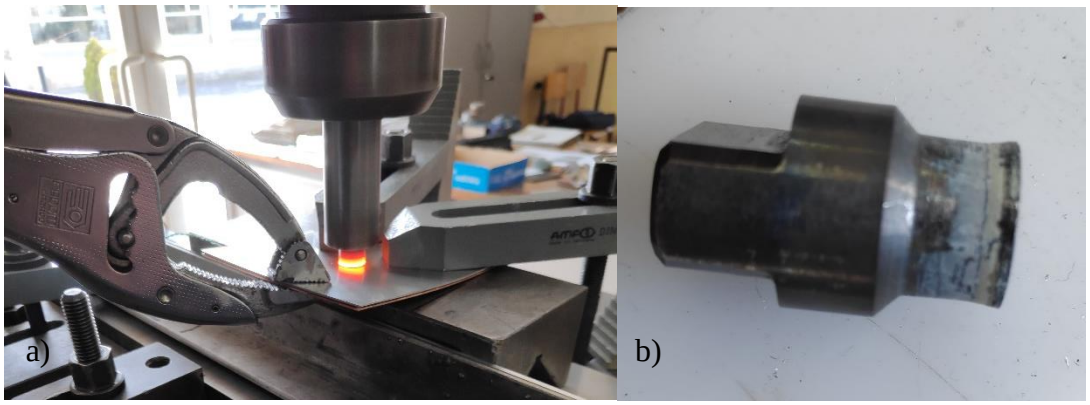

Figure 29 - FSSW tool: a) incandescence and b) geometry and appearance change.

4.2. Temperature data analysis

Overall, the total heat can be attributed to two factors, i.e., the heat generated by the friction between the tool and the workpiece and the heat generated by the plastic deformation, which is associated with the internal frictional forces due to the material's resistance against deformation [62,63]. The temperature versus welding time curves were plotted based on the temperature acquisition system and data processing, as shown in Figs. 30 to 33. The graphs presented in these figures correspond to the smoothed curve for each spot weld performed. The grey area represented in the graphs identifies the welding phase, corresponding to the actual welding time, which may be slightly different from the tested welding times of 20 and 60 s, especially for the SP12 tool since the time count began at the plunging phase, thus reducing the actual welding time. For the SP12-Cu/SS-870-20-0.8 trial, the temperature record was not obtained because of technical reasons.

Fig. 30 shows the registered temperature for the welds SP12-Cu/SS-870-60-0.8 (Fig. 29a)) and SP12-Cu/SS-870-60-1 (Fig. 29b)), where two different penetrations were used, 0.8 and 1 mm, with the same tool, material position, rotational speed, and welding time. The SP12-Cu/SS-870-60-0.8 and SP12-Cu/SS-870-60-1 show a similar temperature evolution. At the beginning of the welding process, the temperature rapidly increased as the tool was plunged into the workpiece. This temperature increase is observable even during the welding phase. After the maximum temperature is reached, there is temperature maintenance until the end of the welding. A slight reduction is seen in the temperature of the SP12-Cu/SS-870-60-1 trial during the welding phase, which may be justified by the DP fixture system, which allowed the workpiece to bend in the copper layer. This weld registered the largest area of color change, with a spread in the direction of the unfixed side. The retracting phase shows a cooling curvature as a logarithmic curve.

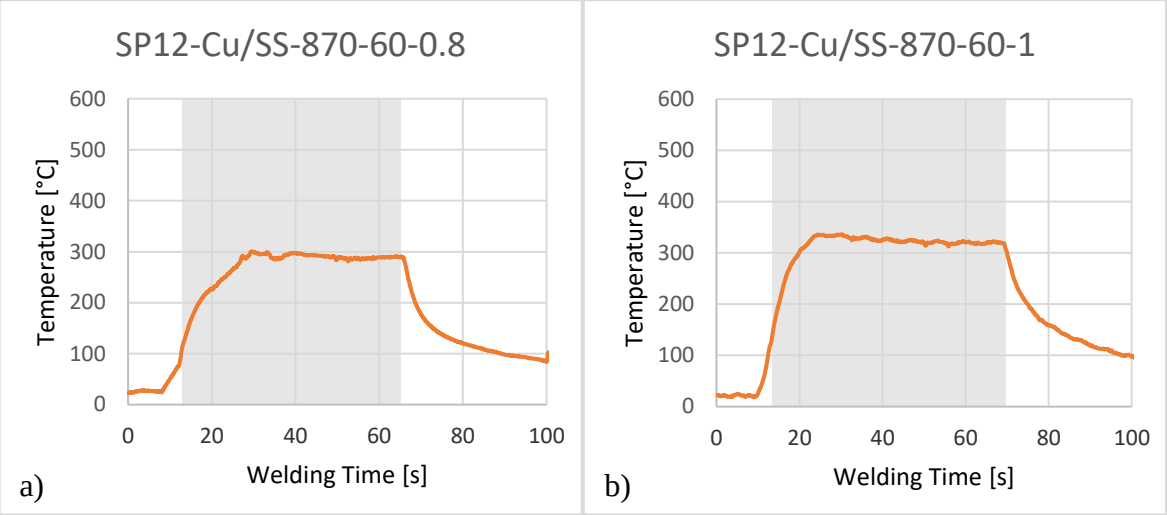

Figure 30 - Temperature evolution: a) SP12-Cu/SS-870-60-0.8 and b) SP12-Cu/SS-870-60-1.

The peak temperature was 300 and 335 °C for the SP12-Cu/SS-870-60-0.8 and SP12-Cu/SS-870-60-1, respectively. A higher peak temperature was registered for the weld produced with a higher plunge depth, 1 mm, which is a result already reported in other studies [62–65]. The authors of these studies concluded that by increasing the tool plunge depth, an increase in temperature is registered, which is explained by an increase in the axial force, leading to an increase in the frictional heat.

Fig. 31 shows the temperature evolution for the same tool, material position, and welding time as the welds addressed in Fig. 30, but with an increased rotational speed of 1500 rpm and a plunge depth of 0.8 mm. Although the graph in Fig. 31 shows a wavy form during the welding phase, due to the presence of noisy data, it can be stated that the weld SP12-Cu/SS-1500-60-0.8 also shows stabilization in temperature like the two previous welds. However, this time a gradual increase in the temperature during the welding phase is seen. In this graph, it is observable that the effect of the rotational speed had less impact than the increase in plunge depth on the temperature, registering a peak temperature of 323 °C.

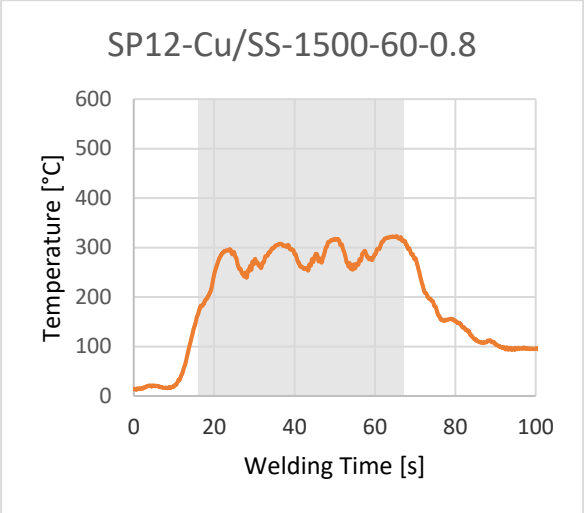

Figure 31 - Temperature evolution for the weld SP12-Cu/SS-1500-60-0.8.

Fig. 32 compares the temperature evolutions with time for the same tool, SP12, material position, SS/Cu, and plunge depth, 0.8 mm, but with the variation of rotational speed and welding time. Taking this into account, Figs. 32a), c), and e) show the results, using a 20 s welding time, with an increasing rotational speed of 870, 1140, and 1500 rpm, respectively. In turn, Figs. 32b), d), and f) show the results with the same rotational speed trend but with a 60 s welding time. Thus, the rows show an increase in rotational speed, and the columns show an increase in welding time.

From Fig. 32, it can be observed that none of the graphs displays the shape previously seen with copper used as the top plate, where the temperature stabilization is well identified, meaning that no thermal balance was achieved. Since the thermal conductivity of copper is 20x higher than that of the SS, when the heat is added, it flows through the nearest surrounding environment, the copper plate, being able to achieve a thermal balance. In the case of SS, as the top plate, the heat generated ends up being retained, so the continuous increase in the heat generated leads to an increased temperature. Even so, it is important to note that the peak temperatures were 237 and 253 °C for the SP12-SS/Cu-870-20-0.8 (Fig. 32a)) and SP12-SS/Cu-870-60-0.8 (Fig. 32b)) welds, respectively. The peak temperature registered for the SP12-SS/Cu-870-60-0.8 was lower than the peak temperatures achieved for similar conditions in Cu/SS welding. A possible justification for this unexpected difference is the measuring zone in the two welding types, which was the same, i.e., 5 mm from the shoulder end. As the SS has a much lower conductivity, the temperature reached at 5 mm from the shoulder reflects much less the temperature in the center of the weld because the heat does not flow there so easily. In Cu/SS, even if the temperature reached may even

be lower, the thermocouple could register a temperature closer to the temperature in the center due to the greater conductivity of this material.

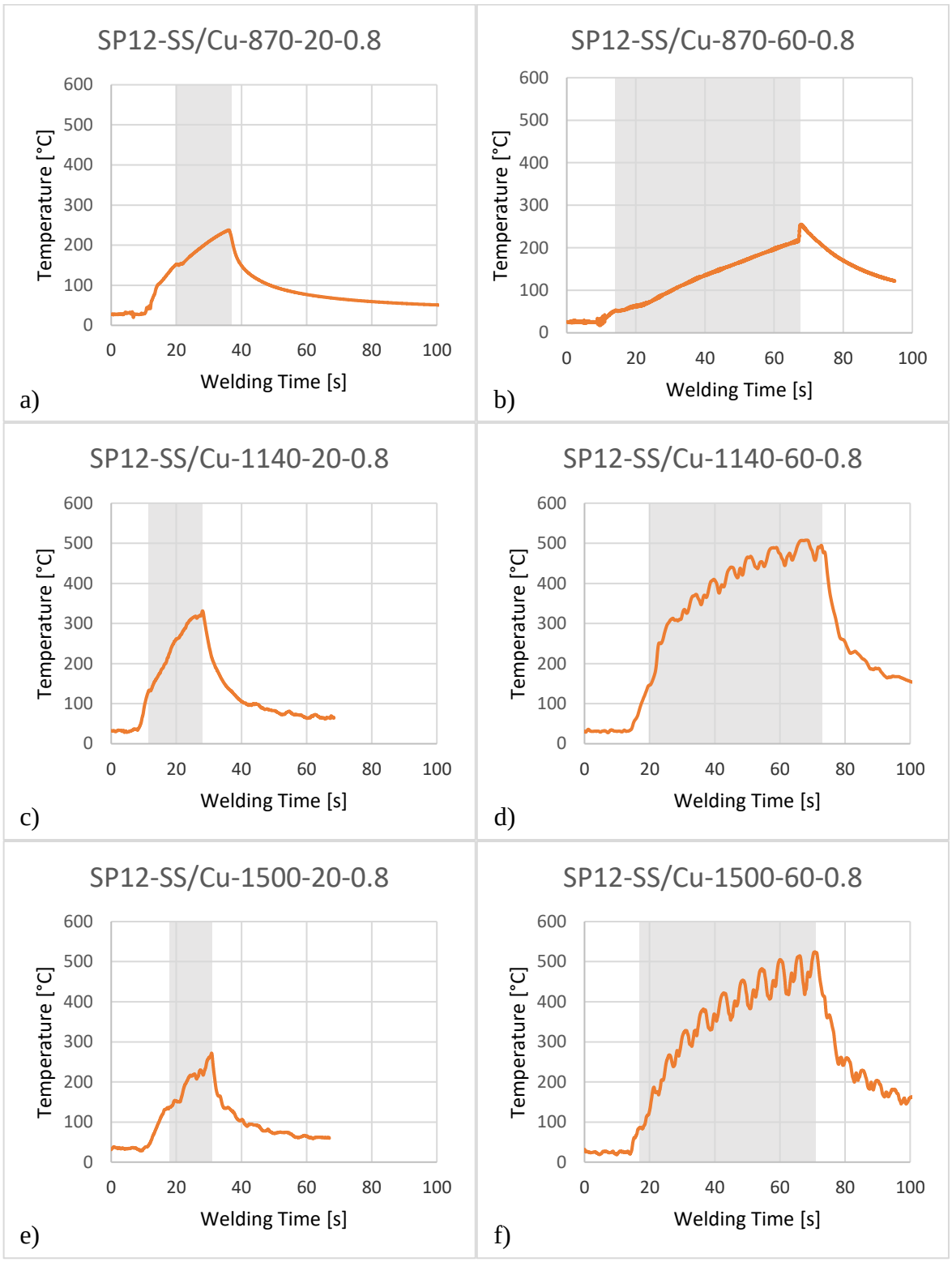

Figure 32 - Temperature evolution: a) SP12-SS/Cu-870-20-0.8, b) SP12-SS/Cu-870-60-0.8, c) SP12-SS/Cu-1140-20-0.8, d) SP12-SS/Cu-1140-60-0.8, e) SP12-SS/Cu-1500-20-0.8, and f) SP12-SS/Cu-1500-60-0.8.

Fig. 32b) shows that the temperature recorded during the SP12-SS/Cu-870-60-0.8 weld is not the most reliable since an almost linear evolution is displayed. Besides that, a spike is seen at the end of the welding phase, taking the temperature from 216 to 249 °C in 0.4 s. However, the aspect that makes this data acquisition unreliable is that it takes almost 56 s of the welding phase to reach a similar temperature to the one obtained after 16 s for the SP12-SS/Cu-870-20-0.8 trial. The visual observation of the weld surface also shows that the area of color change is more extensive comparing these two welds, so it was expected that the temperature would also be higher. In addition to a probably incorrect reading by the thermocouple, this error was also caused by the incorrect position of the thermocouple. The distance to the periphery of the shoulder used was approximately 7 mm, instead of 5 mm, leading to a lower temperature being registered. Sahu and Pal [66] observed a temperature reduction over the distance from the weld line using thermocouples at different distances from the weld center. Armansyah et al. (67) also proved this temperature reduction by computational approach, verifying the maximum temperature below the tool near the probe.

The curves from the welds SP12-SS/Cu-1140-60-0.8 and SP12-SS/Cu-1500-60-0.8, shown by the graphs in Figs. 32d) and f), can be considered a continuation of the ones seen in Figs. 32c) and e), respectively, which have the same parameters but a welding time of 20 s. The first two are similar to a semi-inverted parabola if disregarded the wavy form due to the cyclical noise. The SP12-SS/Cu-1140-60-0.8 and SP12-SS/Cu-1500-60-0.8 were the only trials from Fig. 32 that attained a successful weld, reaching a maximum temperature of 507 and 524 °C, respectively.

In Fig. 33, the same comparison is made as the previous Fig. 32, but this time with the SP10 tool. This means that Figs. 33a), c), and e) show the results using a 20 s welding time, with a rotational speed increasing, and Figs. 31b), d), and f) show the results using a 60 s welding time and the same increments in rotational speed.

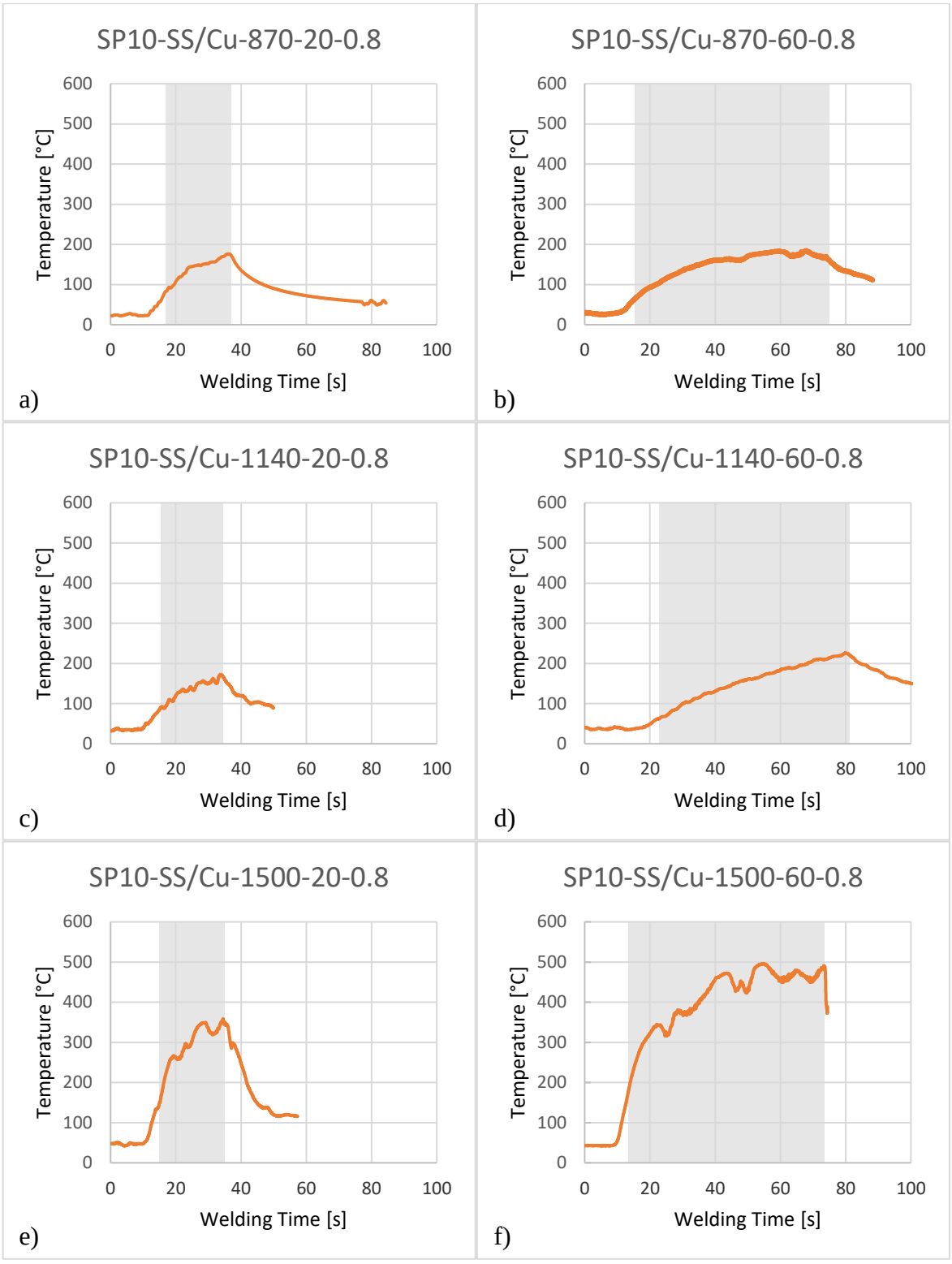

Figure 33 - Temperature evolution: a) SP10-SS/Cu-870-20-0.8, b) SP10-SS/Cu-870-60-0.8, c) SP10-SS/Cu-1140-20-0.8, d) SP10-SS/Cu-1140-60-0.8, e) SP10-SS/Cu-1500-20-0.8, and f) SP10-SS/Cu-1500-60-0.8.

Despite not having, again, the same shape when the SS was used as the bottom plate, some similarities are seen when using the SP10 and SP12 tools with the same material position. However, it should be noted that in these trials, the welding time started counting when the plunge depth was achieved.

The temperature evolution from SP10-SS/Cu-870-60-0.8 weld, Fig. 33b), is a continuation of the SP10-SS/Cu-870-20-0.8 weld, Fig. 33a), and despite not being noticeably clear, the temperature seems to start to stabilize because the maximum temperature reached was 184 and 176 °C for each weld. SP10-SS/Cu-870-20-0.8 was the trial that started with the tool at ambient temperature.

During the use of 1140 rpm, both SP10-SS/Cu-1140-20-0.8 and SP10-SS/Cu-1140-60-0.8 welds, corresponding to Figs. 33c) and d), show a continuous increase in the temperature during the plunging and welding phase, which indicates that to achieve a temperature stabilization, was necessary a higher welding time. However, the values seem too low to what was expected, with maximum values of 170 and 223 °C.

The temperature curves shown in Figs. 33e) and f) resemble the curve from SP12-SS/Cu-1500-60-0.8 (Fig. 32f)), where it was visible the start of an inverted parabola shape. In particular, Fig. 33f) shows the beginning of a curve with temperature stabilization during the final 20 s of the welding phase. There seems to be a higher stabilization trend for the SP10 than for the SP12 tool. There is less heat generation for the SP10 tool, so the accumulated heat is not as elevated as in the SP12 tool. Even if the dissipation rate is low, it gets closer to achieving a thermal balance. Andrade et al. [67], for lower tool diameters, also registered a lower stabilization temperature, which was achieved more quickly. Contrary to that, increasing the tool diameter raised the stabilization temperature, taking more time to reach it.

In order to better illustrate the influence of the rotational speed, welding time, and tool diameter on the temperature peaks, two different graphs were plotted, as illustrated in Fig. 34. These graphs contain the maximum values of the temperature registered at different rotational speeds, welding times and tool diameters. Fig. 34a) shows the maximum temperature for each rotational speed and welding time using the SP10 tool, and Fig. 34b) displays the same data type but for the SP12 tool. The successful welds are represented with a green diamond.

Through Fig. 34, both tools reveal a temperature rise with the increase of rotational speed and welding time due to the friction generated during welding and more prolonged exposure to the heat input, respectively. This increase is similar to what was reported by Ataya et al. [49]. It was also reported that the higher the welding time and rotational speed, the lower the plunging force and torque, suggesting a higher softening intensity of the materials during the

process [68,69]. Also, the observations made in the visual analysis meet what was expected to see with the temperature.

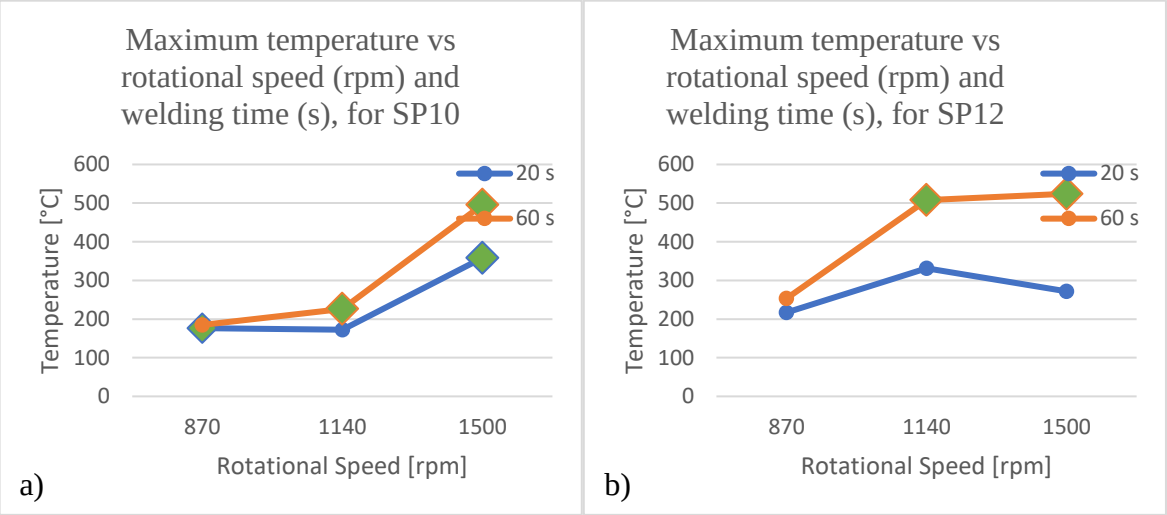

Figure 34 - Influence of rotational speed and welding time with maximum temperature: a) SP10 and b) SP12 tool.

Still, on the graphs from Fig. 34, the increase in temperature is seen from 870 to 1140 rpm for the SP12 tool, with a slight increase from 1140 to 1500 rpm. However, with the SP10 tool, this happens predominantly from 1140 to 1500 rpm. The temperature stabilization stayed above but near 500 °C. Andrade et al. [67] explained that for each tool diameter, there is a threshold in the maximum temperature that can be reached. For larger tool diameters may even be independent of the tool rotational speed. This situation happens when using the SP12 tool, where the threshold is reached. Nevertheless, for the SP10 tool, that threshold has not yet been reached since the threshold temperature increases with the tool diameter. As the shoulder diameter increases, the contact area between the tool and the material increases, generating more heat, which leads to a higher threshold temperature [8,66].

SP12-SS/Cu-1500-20-0.8 trial shows a reduction compared to its precedent, something that is not expected but can be explained by the actual welding time that the trial was subjected, which was 14 s compared to 17 s from the weld SP12-SS/Cu-1140-20-0.8. The welds with 870 rpm, both using the SP12 and SP10 tools, do not show a significant difference in the maximum temperature for 20 or 60 s, while for the remaining conditions, a temperature increase is seen with the largest diameter.

Another graphical approach to understanding the influence of the material position on the peak temperature is shown in Fig. 35, where the maximum temperature was plotted as a function of the rotational speed. It is possible to conclude that the maximum temperature for the Cu/SS configuration does not suffer a significant variation compared to the SS/Cu; this

can be explained principally by the difference in thermal conductivity between materials, something previously mentioned. A result not expected, but as reported above, the not correct placement of the thermocouple may cause the SS/Cu material position to have a lower temperature registered compared to the Cu/SS when using a lower rotational speed.

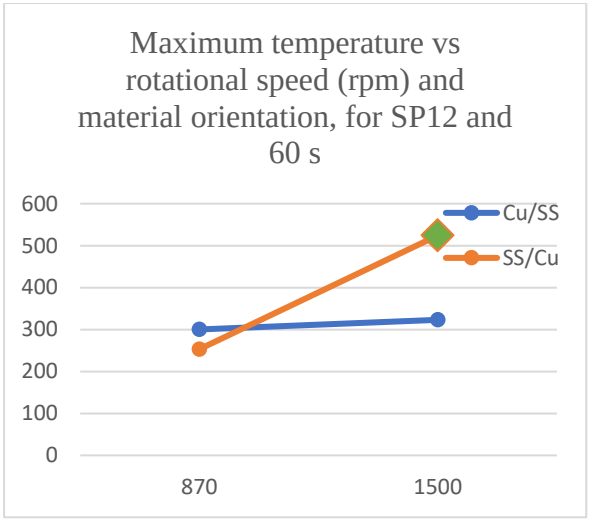

Figure 35 - Influence of material position on the maximum welding temperature.

4.3. Macrostructure

For the six successful welds, SP10-SS/Cu-870-20-0.8, SP10-SS/Cu-1140-60-0.8, SP10-SS/Cu-1500-20-0.8, SP10-SS/Cu-1500-60-0.8, SP12-SS/Cu-1140-60-0.8, and SP12-SS/Cu-1500-60-0.8, a macrostructural study was conducted on the weld cross-section. During the SP10-SS/Cu-1500-60-0.8 weld cut, the weld was damaged, not being possible to obtain a cross-section. Fig. 36 shows the cross-section macrographs of these welds. All images indicate that no defects, such as cracks, pores, voids, and tunnels, were found along the joint line of the cross-section. The flash formation is non-existent since the material was not displaced to the outer edge of the tool shoulder, except for the weld SP10-SS/Cu-870-20-0.8 (Fig. 36a)). However, a depression on the surface is seen in all welds, with more or less intensity, revealing the shoulder actuation zone.

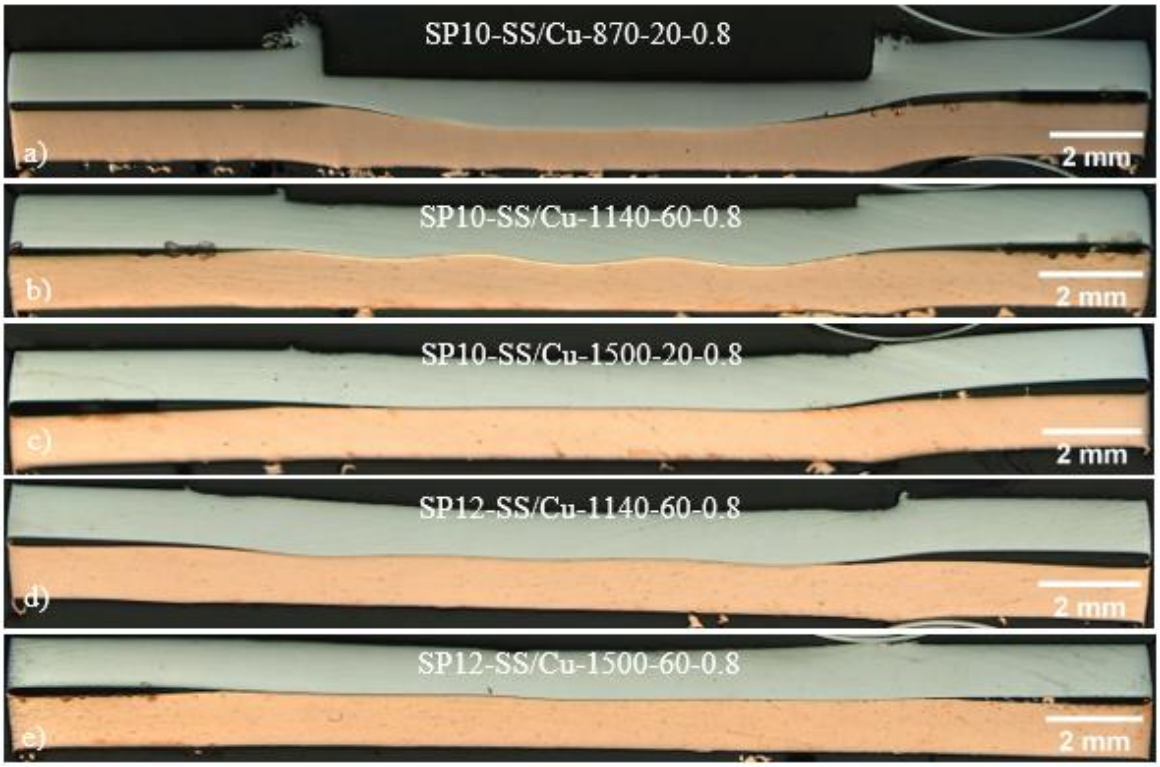

Figure 36 - Transverse cross-section macrographs of the welds: a) SP10-SS/Cu-870-20-0.8, b) SP10-SS/Cu-1140-60-0.8, c) SP10-SS/Cu-1500-20-0.8, d) SP12-SS/Cu-1140-60-0.8, and e) SP12-SS/Cu-1500-60-0.8.

The SP10-SS/Cu-870-20-0.8 macrostructure, Fig. 36a), can explain the reason this weld was a successful joint since a superior reduction in thickness of the SS is noticed, especially on the limit of the shoulder actuation, reducing to 0.567 mm in thickness, leading to the line joint being exposed to higher heat input. Four reasons may explain this, wrong position control when performing the weld, a plunge rate vastly different from the other welds, the tool starting at the ambient temperature, and a sharp edge of the tool. All welds suffered, more or less evidently, from a thickness reduction of the SS and the copper sheet.

An extreme reduction of the thickness of copper and the common hook effect, which can provide some mechanical interlocking, were not observed, which agrees well with what has been reported when performing a copper/steel FSSW [47,49], as well as probe-less FSSW [48]; this means that the bonding was not achieved by macro-mechanical bonding.

The weld SP10-SS/Cu-1140-60-0.8, Fig. 36b), shows the waviness of the joint line, with a convex and concave shape for the SS and copper, respectively. This shape is also seen with less noticeability in Figs. 36a) and 36d) and while performing the visual inspection of the SP10-SS/Cu-870-60-0.8 and SP10-SS/Cu-1140-20-0.8 welds (Fig. 28). This phenomenon is similar to that obtained by Klobčar et al. [70] when analyzing the material flow for aluminum probe-less FSSW with a scrolled shoulder, being influenced by the heat input and the

pressure applied. Although the shoulder is flat in this study, which means a different interaction between tool/material, this phenomenon also seems more recurrent for welds with the SP10 tool since a higher pressure is obtained during the welding, assuming the force remains the same.

The graph from Fig. 37 shows the evolution of the bonding length with the tool diameter, welding time, and rotational speed. The figure reveals that the bonding length increases when the tool diameter, welding time, and rotational speed increase. The increase in the tool diameter and the rotational speed increases the heat generation. On the other hand, the welding time increases the heat addition (the heat is generated during more time, increasing the heat added to the material). These results are similar to the ones obtained by Andrade et al. [71] when analyzing the width of the process-affected zone by tool-assisted friction welding and by Martins [2] when analyzing the joined widths by friction stir diffusion processing.

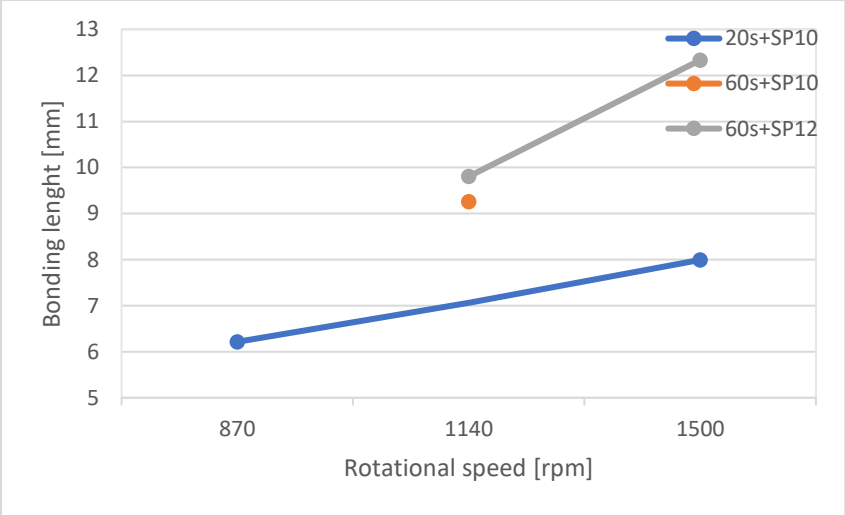

Figure 37 - Bonding length vs tool diameter, welding time, and rotational speed.

4.4. Microstructure

Fig. 38 shows the macrostructure of the cross-section of the same welds presented in Fig. 36 after the copper's etching process, revealing the microstructure of this material. The general features of the grain with the variation of the tool diameter, rotational speed, and welding time are illustrated. The contrast in color has only to do with the chemical etching made.

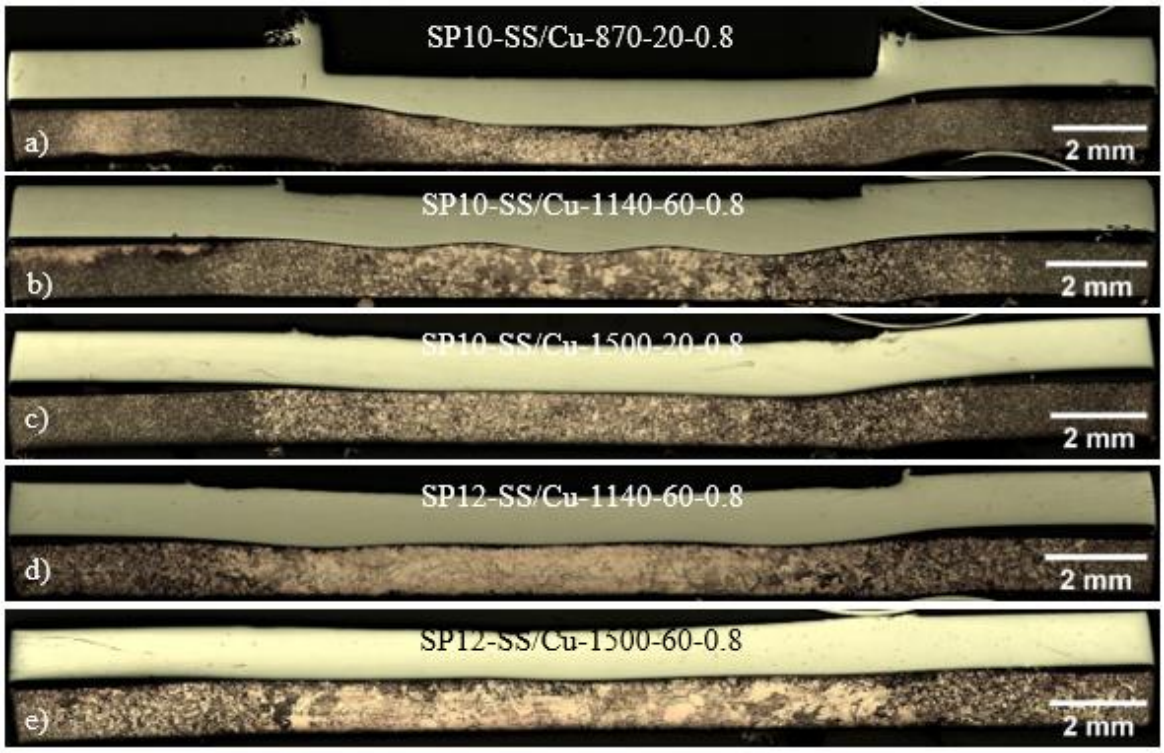

Figure 38 - Transverse cross-section macrographs of the welds after copper's etching: a) SP10-SS/Cu-870-20-0.8, b) SP10-SS/Cu-1140-60-0.8, c) SP10-SS/Cu-1500-20-0.8, d) SP12-SS/Cu-1140-60-0.8, and e) SP12-SS/Cu-1500-60-0.8.

Since the probe-less tool only penetrates the SS, the copper sheet does not experience severe deformation and is mainly affected by heating. So only a HAZ is identified in this material, where grain growth is characteristic. Other authors also identified only a HAZ at the lower sheet [2,43,72], which is different from what is often observed in a butt FSW, where an SZ and TMAZ are also registered for copper [8,56]. This increase in grain size occurs over the entire thickness of the material, as seen in Fig. 38, and with a width superior to the one corresponding to the shoulder actuation zone, except for the weld SP10-SS/Cu-870-20-0.8, Fig. 38a), which corresponds to the trial with lower heat input conditions.

Fig. 39 illustrates, in a frame form, the copper grain structure with a magnification of 200x for the same welds illustrated in Fig. 38. The lines show the various welds, and the columns illustrate the relative position to the weld center, matching the median column to the center of the weld. It should be noted that the distance between micrographs in the same weld may not be identical and may not be precisely coincident between trials. The first image (left end) from the SP10-SS/Cu-870-20-0.8 weld (Fig. 39a)) has a similar grain size as the BM.

The comparison between the SP10-SS/Cu-1140-60-0.8 and SP12-SS/Cu-1140-60-0.8 welds (Figs. 39b) and d)), which have the same parameters except for the tool diameter, confirms that for a higher tool diameter the grain size is larger, being in line with the temperature

results obtained. In addition to this, changing the diameter also affects the longitudinal size of the HAZ in copper, as seen in Figs. 38 and 39. Another parameter that affects the grain structure is the welding time, as previously analyzed by Xie et al. [73]. Through the microstructure of the welds in Fig. 39, it is seen that the SP10 trials with a 20 s welding time, corresponding to Figs. 39a) and c), show a similar microstructure. In turn, the trial with a 60 s welding time, Fig. 39b), even if with a lower rotational speed, has a coarser grain structure. Thus, it can be said that the tool diameter and the welding time have a major influence on the grain size, while the rotational speed has a lesser impact, as seen by comparing Figs. 39d) and e).

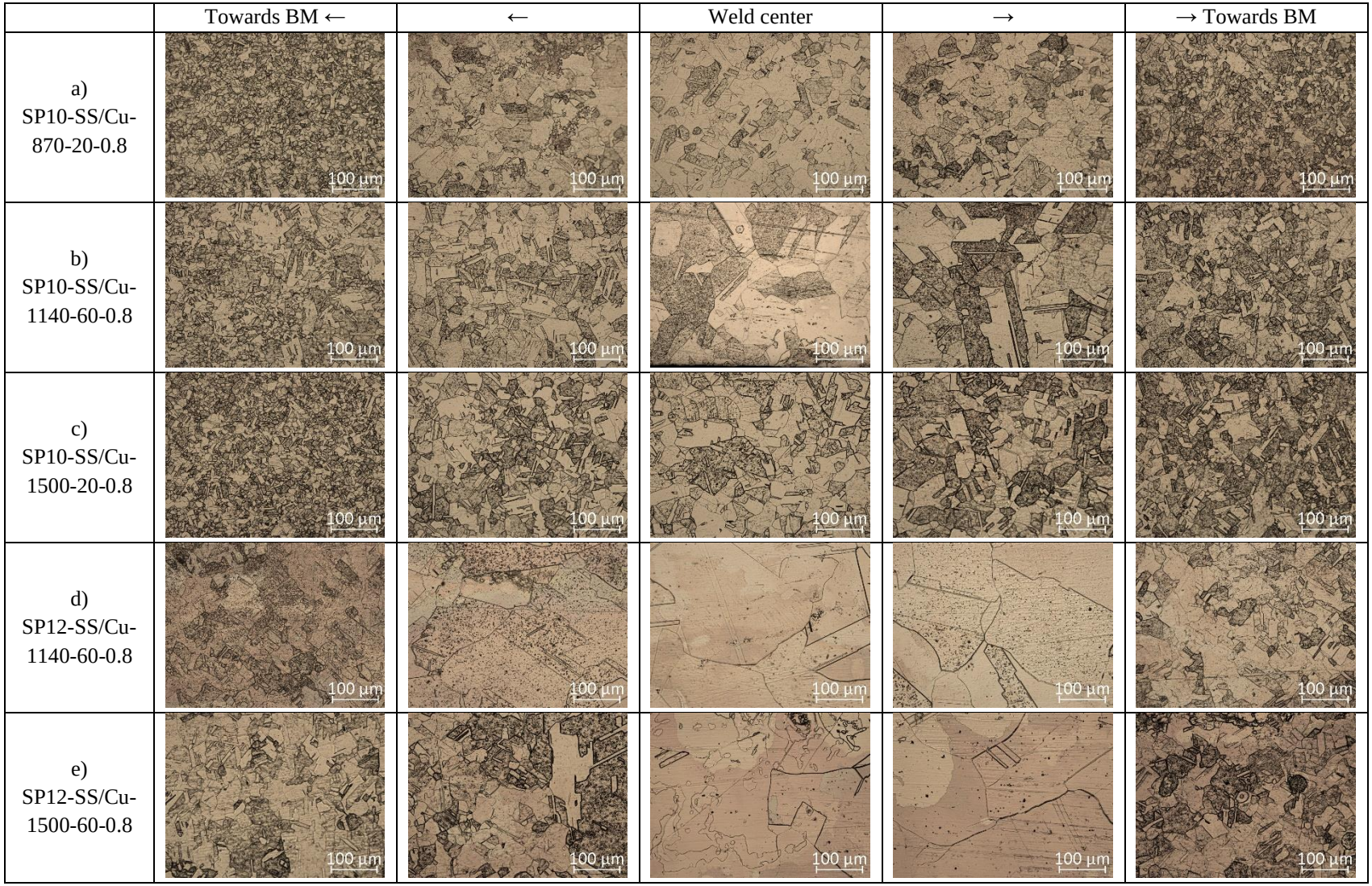

Figure 39 - Micrographs of copper grain structure at 200x magnification for welds: a) SP10-SS/Cu-870-20-0.8, b) SP10-SS/Cu-1140-60-0.8, c) SP10-SS/Cu-1500-20-0.8, d) SP12-SS/Cu-1140-60-0.8, and e) SP12-SS/Cu-1500-60-0.8.

4.4.1. SEM/EDS

To further study the interface, the welds were analyzed by SEM/EDS. Fig. 40 shows some features found at the interface when doing this analysis on the SP10-SS/Cu-1140-60-0.8, SP10-SS/Cu-1500-20-0.8, and SP12-SS/Cu-1500-60-0.8 welds.

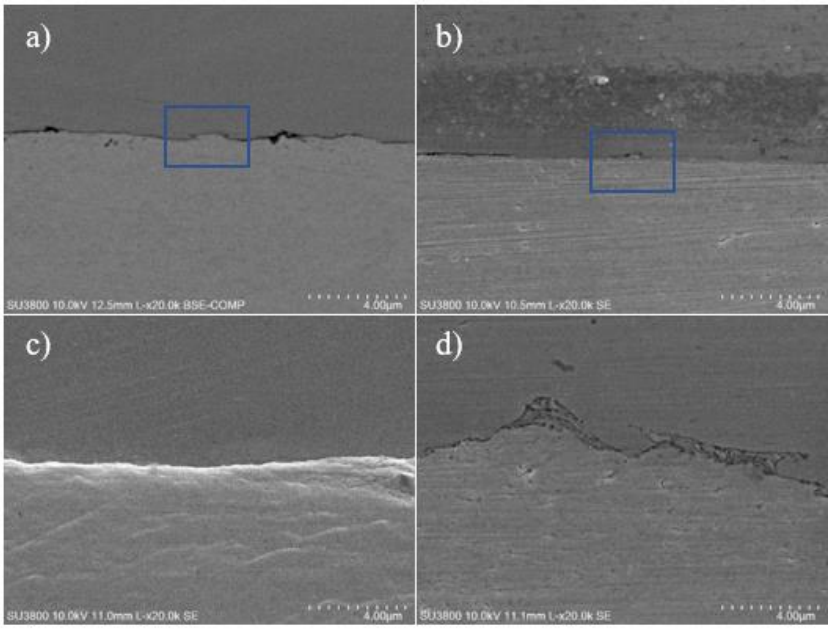

Figure 40 - SEM interface micrographs of the: a) SP10-SS/Cu-1140-60-0.8, b) SP10-SS/Cu-1500-20-0.8, c) and d) SP12-SS/Cu-1500-60-0.8 weld.

The darker dots/areas found in Fig. 40a) can be mistakenly interpreted as nano-sized voids, also noticed in other SEM images. However, these marks can be originated from weld preparation or possibly residual entrapped oxides which fell away during weld extraction, as Shen et al. [50] reported.

In some welds, partial bonding was found at a microscopic level, as illustrated in Fig. 40b), also reported by Martins [2]. However, good bonding between SS and copper with a continuous interface was also achieved, as observed, for example, in Fig. 40c). Also, the absence of a hook effect reduces the partially bonded region at the end of the tool actuation zone, something characteristic of the hook effect, thus, in this case, increasing the contact width [34,72].

A feature that can improve the strength of the weld is the micro-mechanical interlocking, which can be seen in Figs. 39a), b), highlighted by a blue box, and c). This feature is typically seen at a macro level, with the harder material penetrating the softer one due to the material flow [49]. However, in these welds, the material penetrates at a micro-level at the interface in a very localized area. Another observation that can be made is the intensity of this feature,

which seems to get bigger with the parameters increase. Like the maximum temperature reached for each weld, it gets higher, which can lead to a more significant softening in copper, thus increasing the intensity of this phenomenon, so it is expected to be maximum in the SP12-SS/Cu-1500-60-0.8 weld.

For the SP10-SS/Cu-870-20-0.8 weld, an analysis of the copper and SS surface by EDS element map was performed since this joint was forced to separate to allow this analysis. The result of this analysis is presented in Fig. 41. In some areas, the copper surface shows a high presence of Fe (Fig. 41a)), while Cu is seen in the SS surface (Fig. 41b)), which may be another evidence of the micro-mechanical interlocking. Thus, it is expected that in the welds where the micro-interlocking was strongest, this phenomenon occurs with greater intensity.

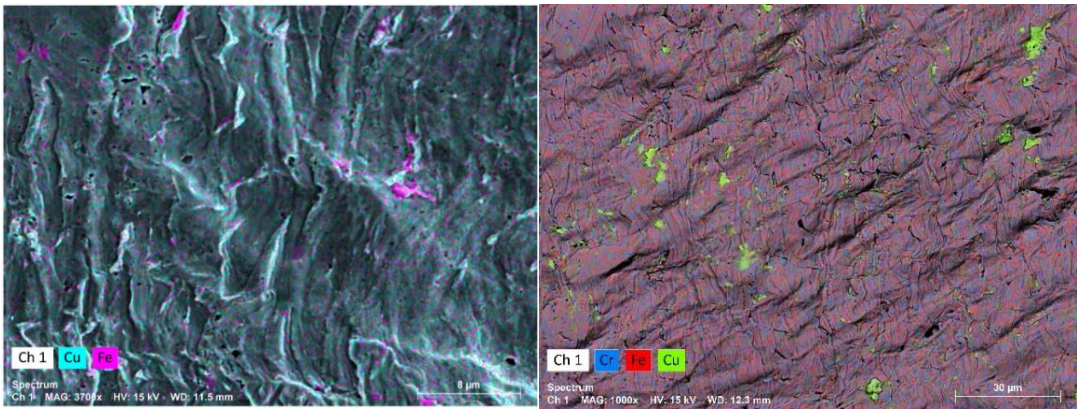

Figure 41 - EDS surface elemental maps for SP10-SS/Cu-870-20-0.8 weld: a) Copper side and b) SS side.

An EDS analysis was conducted along a line across the interface for the SP10-SS/Cu-1140-60-0.8, SP10-SS/Cu-1500-20-0.8, and SP12-SS/Cu-1500-60-0.8 welds. The results corresponding to the SP12-SS/Cu-1500-60-0.8 weld are illustrated in Fig. 42. For all the welds, Cu, Fe, Ni, and Cr were detected along this line. Other elements were also found, such as oxygen and carbon due to oxidation and contamination, respectively.

The result of the EDS line scan of elements, and for all the trials, suggests the existence of mutual diffusion of Cu and Fe across the interface because there is no sharp transition in Fe and Cu chemical compositions, which refers to the occurrence of material transference at the interface. Other authors also reported this mutual diffusion in probe-less FSSW, lap FSW, and radial friction welding [5,49,53,74]. Nevertheless, in other studies, this mutual diffusion was not seen, being explained by the low solubility shown by the phase diagram of Cu-Fe, with only a Ni diffusion from steel into copper [3,50,56].

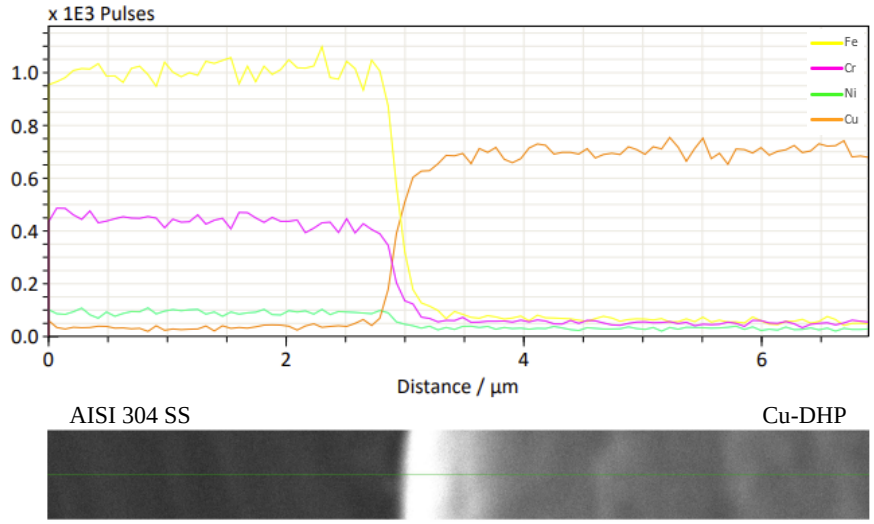

Figure 42 - EDS line scan element of weld SP12-SS/Cu-1500-60-0.8.

It is known that the diffusion constant (D_0) and the activation energy of diffusion (Q) for Cu into a γ-Fe matrix are $D_0=1.9*10^{-5}$ m^2/s and Q=270.7 kJ/mol, respectively and for Fe into a Cu matrix is $D_0=5.04*10^{-5}$ m^2/s Q=193.049 kJ/mol, respectively [75,76]; this shows that the diffusion coefficient of Cu into γ-Fe is smaller than γ-Fe into Cu and needs higher activation energy. Moreover, other studies reported that the diffusion length of Fe in Cu was greater than that of Cu in Fe [5,74]. However, that relationship was impossible to measure in the present study, as well as establish a correlation between the temperature reached and the diffusion that occurred for the trials analyzed. It should also be pointed out that the EDS is not a precisely accurate technology, being even lower for relatively small amounts of some elements or when analyzing at very high magnifications.

4.5. Hardness testing

Fig. 43 displays the Vickers microhardness horizontal profiles near the interface for both materials. Similar to the metallographic analysis and SEM/EDS, the graph only shows the welds in which bonding was achieved. The tool actuation zone is marked with a darker and a lighter grey area for the SP10 and SP12, respectively, as well as the average hardness for the BMs, represented by two horizontal lines. According to the profile, the hardness distribution was found to be relatively symmetric to the central axis, with a general hardness increase on the upper sheet and a decrease on the lower sheet.

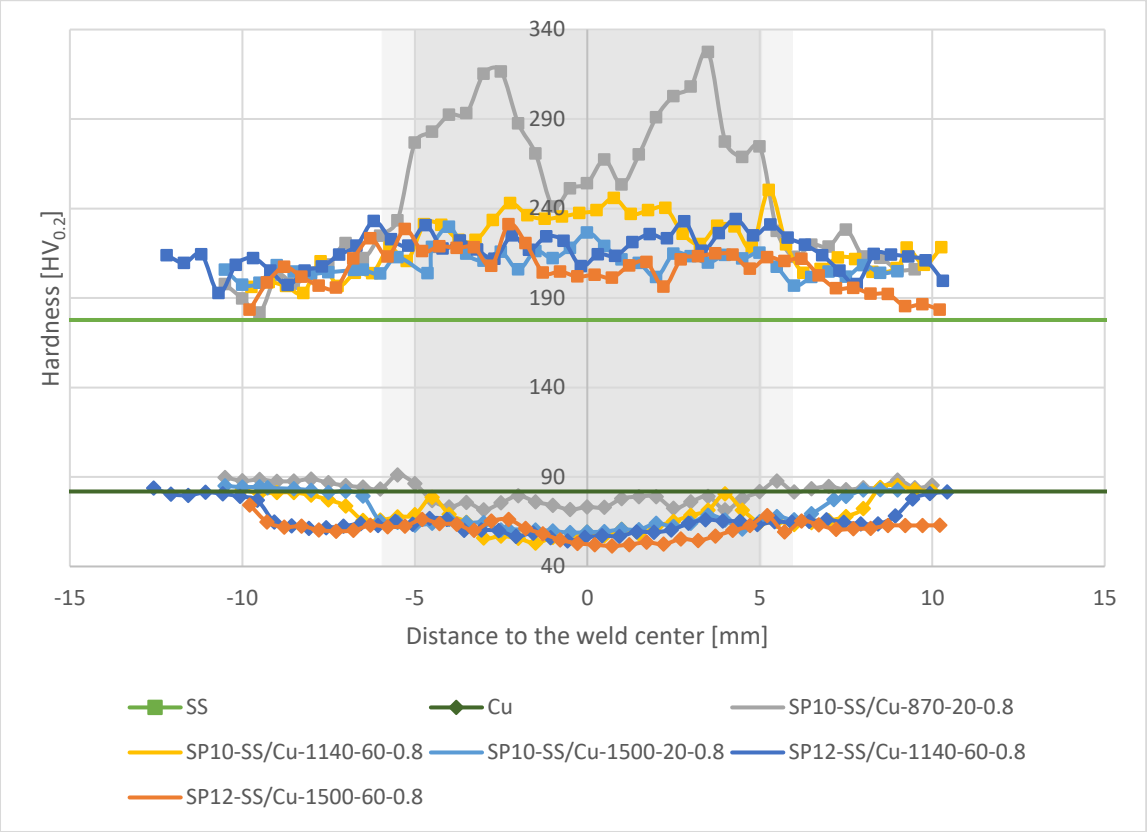

Figure 43 - Evolution of the horizontal hardness profile of the welds.

The hardness evolution for SS in Fig. 43 shows that there is always an increase in hardness compared to the BM. This increase is apparent even outside the tool actuation zone. The highest hardness was registered in the weld SP10-SS/Cu-870-20-0.8, with a value of 327 $HV_{0.2}$ because of the high deformation to which the weld was subjected, visible in the macrostructure (Fig. 36a)). For the SS and referring only to the nugget, this increase in hardness would be expected, even without having been revealed the microstructure of the SS since it was not chemically etched. However, considering the literature [48,49,77–79], this area is known to experience a very high deformation due to the stirring and the axial force, coupled with high temperature, which led to grain recrystallization.

Contrarily, the hardness evolution for copper, in Fig. 43, shows a decrease compared to the BM, and changes in the width of the area affected by the process are seen. A superior reduction in hardness is seen with a higher rotational speed and welding time. At the same time, the width of that reduction gets bigger. The lowest hardness was registered on the trial SP12-SS/Cu-1500-60-0.8, with a value of 51.4 $HV_{0.2}$. In this case, the results agree with the microstructure found in the copper (Fig. 39) and the literature results [17], where intense grain growth is seen since the copper undergoes an annealing process. Nevertheless, the hardness from SP10-SS/Cu-870-20-0.8 and SP10-SS/Cu-1140-60-0.8 welds have some

regions (under the tool actuation zone) that show a higher or a similar value as the BM. These regions experienced some deformation that counteracts the effect of temperature on hardness, having a coincident position with the zones of thickness reduction observed in copper in the macrostructural analysis (Figs. 36a) and b)).

The Vickers microhardness vertical profile (along the thickness direction) of the SS and copper sheets is shown in Fig. 44. According to the profile, the influence of the parameters is more significant on the hardness of SS than that of copper since the process has a thermal and mechanical influence on SS but only has a thermal impact on copper. Fig. 44 also shows that does not exist major difference between horizontal and vertical hardness. Additionally, a high vertical variation in hardness between trials is seen for the SS sheet, especially between tool diameters. With the use of the SP10 tool, thus reducing the contact area, the pressure is expected to increase, subjecting the material to a more significant deformation, which leads to a higher hardness. This difference is reduced towards the interface because the hottest zone will be at the SS/tool interface, and the deformation is also more intense in that place (SS/tool). On the other hand, this diameter difference does not impact copper much, as seen by the slight hardness variation (against the SS). The hardness of copper tends to reduce towards the interface since the copper's top (interface) is more exposed than the weld bottom to the temperature.

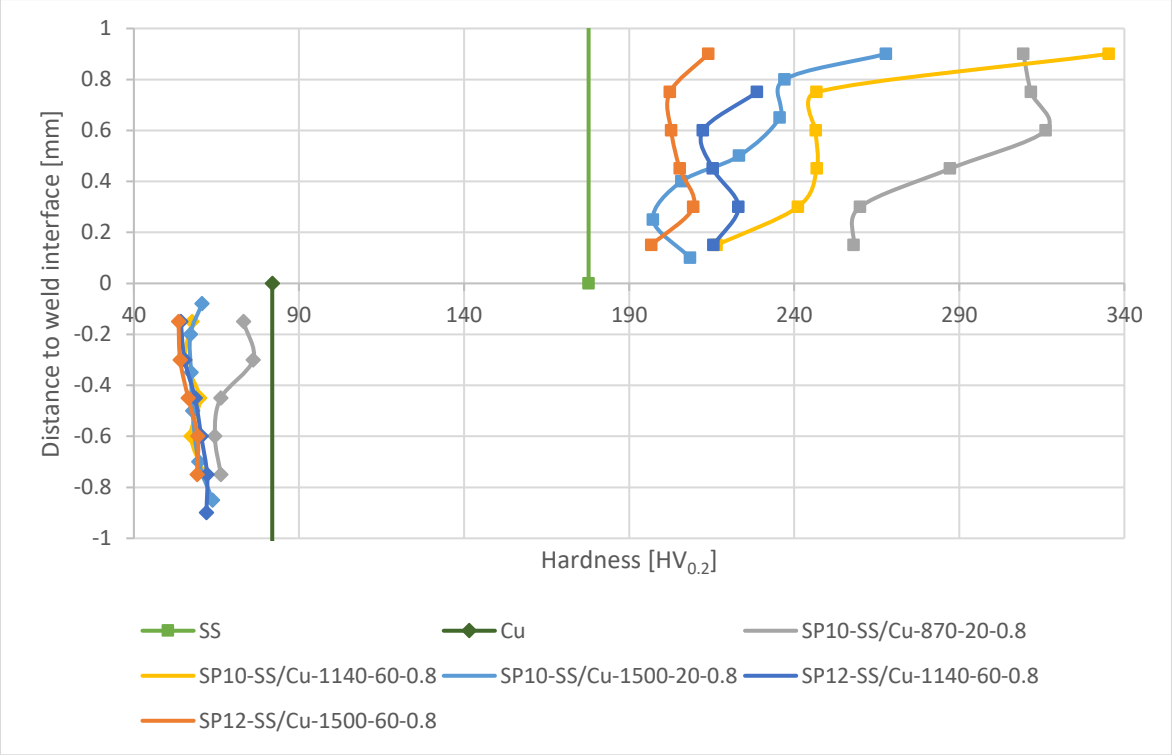

Figure 44 - Evolution of the vertical hardness profile of the welds.

Table 10 displays, for the horizontal profile, the highest and the lowest hardness for each trial. The table also shows the average hardness for each material from each trial within a central width of 8 mm, allowing the calculation of the hardness variation against each BM. Fig. 45 puts together the average hardness obtained for each material and trial, comparing it with the temperature measured and the parameters used.

Table 10 - Highest, lowest, and average hardness for each weld and hardness variation.

Welds	Highest hardness for SS and lowest hardness for Cu registered [$HV_{0.2}$]		Average hardness with a width of 8 mm [$HV_{0.2}$]		Hardness variation compared to the BM [%]	
	SS	Cu	SS	Cu	SS	Cu
SP10-SS/Cu-870-20-0.8	327.37	67.72	283.48	75.26	60%	-8%
SP10-SS/Cu-1140-60-0.8	250.37	53.01	233.63	61.80	31%	-25%
SP10-SS/Cu-1500-20-0.8	229.68	58.87	214.00	62.37	20%	-24%
SP12-SS/Cu-1140-60-0.8	233.99	54.30	219.86	59.85	24%	-27%
SP12-SS/Cu-1500-60-0.8	231.14	51.45	210.55	57.16	18%	-30%

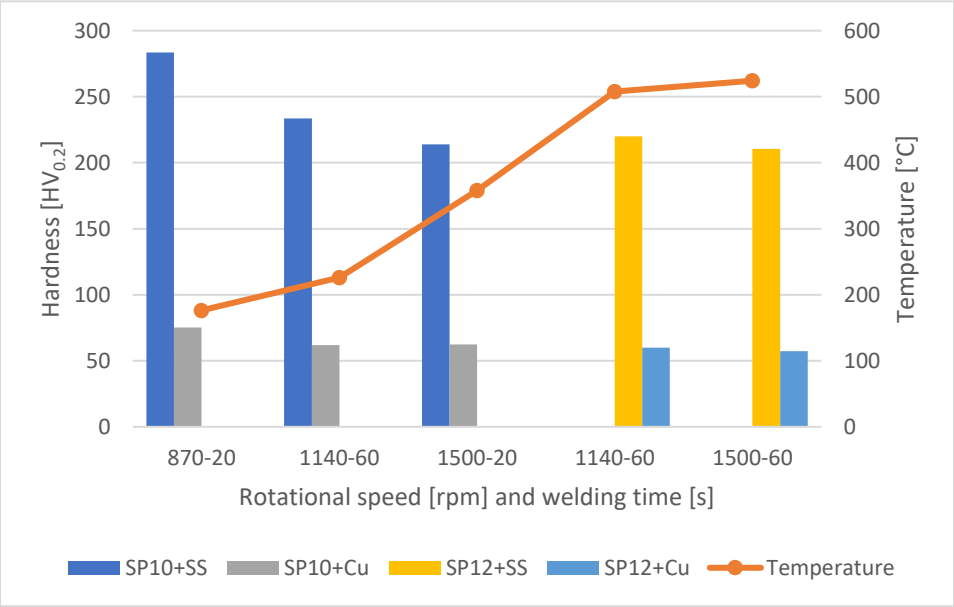

Figure 45 - Influence of parameters and temperature on the average hardness of the welds.

Through Table 10 and Fig. 45, it is possible to visualize that the SS goes under a continuous decrease in its hardness with the increase in parameters. The average grain size in the nugget zone is expected to be higher for more significant heat inputs [80]. The recrystallized grain is formed in this zone, which undergoes grain growth during the cooling cycle, being accelerated by an increase in the maximum temperature [81]. Hence, the SP10-SS/Cu-870-20-0.8 has the highest hardness, and the SP12-SS/Cu-1500-60-0.8 trial has the lowest. The SP10-SS/Cu-1500-20-0.8 trial has a lower value compared to SP12-SS/Cu-1140-60-0.8

because the welding phase is shorter, not allowing a more accentuated deformation, even though the temperature had been lower.

For the hardness evolution in copper, there is a continuous reduction with the parameters increase since the temperature also increases, softening the material even more; however, these hardness variations are softer than in the SS. Nonetheless, the SP10-SS/Cu-1500-20-0.8 trial shows a higher hardness than SP10-SS/Cu-1140-60-0.8, even with a higher temperature. Since the SP10-SS/Cu-1500-20-0.8 weld is performed using a lower welding time, it limits the time the weld is exposed to the generated heat, making a higher grain growth impossible [49], thus showing the impact of this parameter on the hardness. Its influence is well seen in the microstructural analysis (Fig. 39). A 20 s welding time shows a finer grain against the 60 s, causing the hardness of the trials with 20 s to have a higher hardness than those of 60 s.

4.6. Tensile-shear testing

Fig. 46 illustrates the Force-Displacement curves for two trials to demonstrate the repeatability and how the joint behaves during the test. Since the tested specimens were not only under the effect of a specific nature of stress due to the configuration of the weld, the Stress-Strain curves were not obtained, making it impossible to obtain the joint efficiency.

In general, repeatability was seen for all the welds, where at least two specimens showed equivalent results. There are some conditions, like colder parameters or more worn tools, where there is higher dispersion in results, especially for the specimens from the SP10-SS/Cu-870-20-0.8 (Fig. 46 a)) and SP12-SS/Cu-1500-60-0.8 welds. The SP10-SS/Cu-870-20-0.8 weld has no repeatability since its maximum force varies significantly among the different specimens. The same can no longer be referred for the SP12-SS/Cu-1140-60-0.8 specimens, shown in Fig. 46b), since similar maximum forces and displacements were obtained.

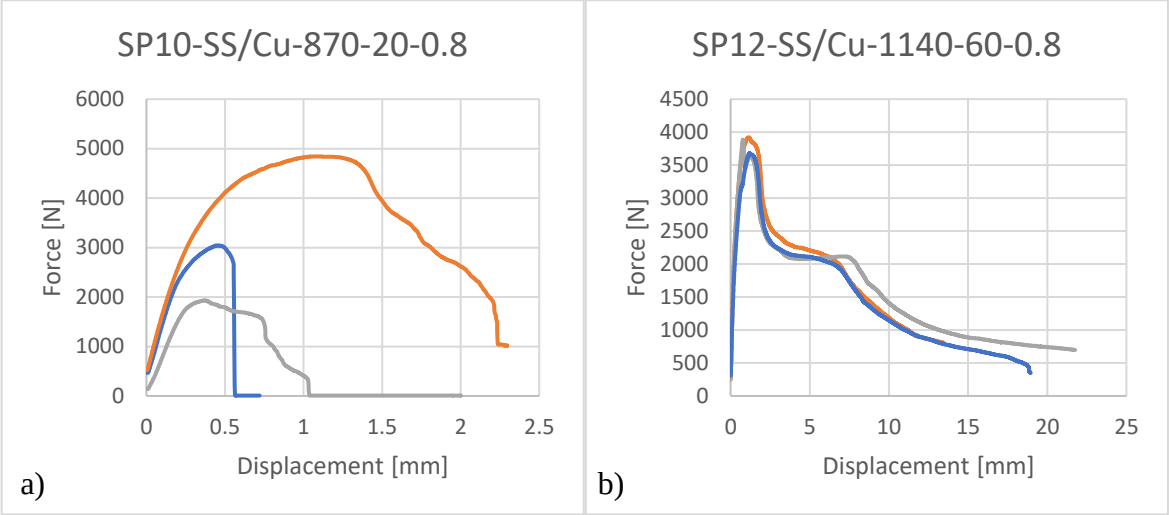

Figure 46 - Force-Displacement curves of the welds: a) SP10-SS/Cu-870-20-0.8 and b) SP10-SS/Cu-1140-60-0.8.

The maximum force values registered per specimen from each weld are shown in Table 11. The table also shows the average force values registered per weld and the failure type of each specimen. It can be concluded from Table 11 that with the increase in parameters, whether in tool diameter, rotational speed, or welding time, there is a general increase in the maximum force recorded.

Table 11 - Maximum and average force and failure type registered in tensile-shear testing.

Welds	Max. Force [N]	Average Force [N]	Failure type
SP10-SS/Cu-870-20-0.8	3040.139	3271.18	Interfacial
	4841.646		Nugget pull-out
	1931.747		Nugget pull-out
SP10-SS/Cu-1140-60-0.8	3461.234	3657.36	Nugget pull-out
	3835.027		Nugget pull-out
	3675.826		Nugget pull-out
SP10-SS/Cu-1500-20-0.8	4205.736	4168.07	Nugget pull-out
	4130.411		Nugget pull-out
SP10-SS/Cu-1500-60-0.8	3668.769	3409.47	Nugget pull-out
	3150.177		Nugget pull-out
SP12-SS/Cu-1140-60-0.8	3919.713	3827.97	Nugget pull-out
	3680.086		Nugget pull-out
	3884.109		Nugget pull-out
SP12-SS/Cu-1500-60-0.8	5121.438	4493.54	Nugget pull-out
	4323.069		Nugget pull-out
	4036.125		Nugget pull-out

The failure type is a qualitative measure of welding performance. The welds with a nugget pull-out failure have a better energy absorption capability and load-carrying capacity than those which fail under interfacial mode [82]. As seen in Table 11, the most common failure

type for the trials under study was nugget pull-out. As expected, the material to fracture under the tensile-shear testing was copper since it is the softest material and even showed a hardness reduction compared to the BM.

Fig. 47 illustrates the different failure types found for the welds, revealing each material's interface. Fig. 47a) reveals the only specimen that failed at the interface, corresponding to the SP10-SS/Cu-870-20-0.8 weld, since it links to the weld with the lowest heat input. In Fig. 47b), it is observed that all the SS material under the tool separated itself from the BM. This situation occurs due to the extreme reduction in the thickness of the SS in that area, which is expected to be similar to what was observed in the macrostructure image from this weld. However, the type of failure considered for this specimen was nugget pull-out.

Figs. 47c) and d) show the specimens' most common type of failure. In the first case (Fig. 47c)), a nugget pull-out with complete copper separation is seen, whereas (Fig. 47d)) a nugget pull-out but without separation of the nugget from the copper is seen in the second case. This type of failure behavior and its propagation were studied by other authors [83–85]. Beyond how the test is conducted, which intensifies the bending of the sheets, for the welds using the SP12 tool, it was more common to see a nugget pull-out, as shown in Fig. 47d). One explanation for this difference is the increase in the joint width. By increasing the joint width, there is a point during the test that the resistance section becomes inferior in the copper compared to the one from the joint, leading to a crack propagation through the copper BM. It is also expected that the fracture mode, although not visualized, to be ductile since the fracture occurs in the HAZ of the copper, peripheric to the bonding area.

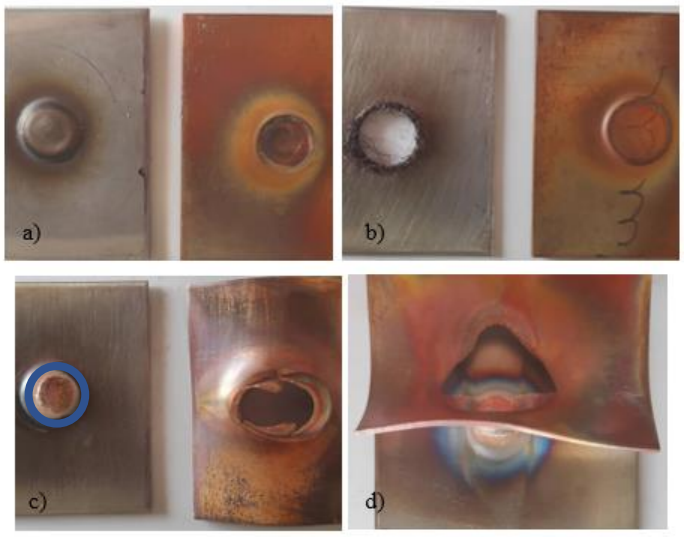

Figure 47 - Different specimen failure types: a) interfacial from SP10-SS/Cu-870-20-0.8, b) nugget pull-out from SP10-SS/Cu-870-20-0.8, c) nugget pull-out from SP10-SS/Cu-1140-60-0.8, and d) nugget pull-out from SP12-SS/Cu-1140-60-0.8.

To show the trend of copper hardness reduction and force increase, Fig. 48 shows a graph with the maximum force, the average force, and the hardness for each weld. The copper hardness is the only one shown, as this material was the one to affect the weld strength primarily.

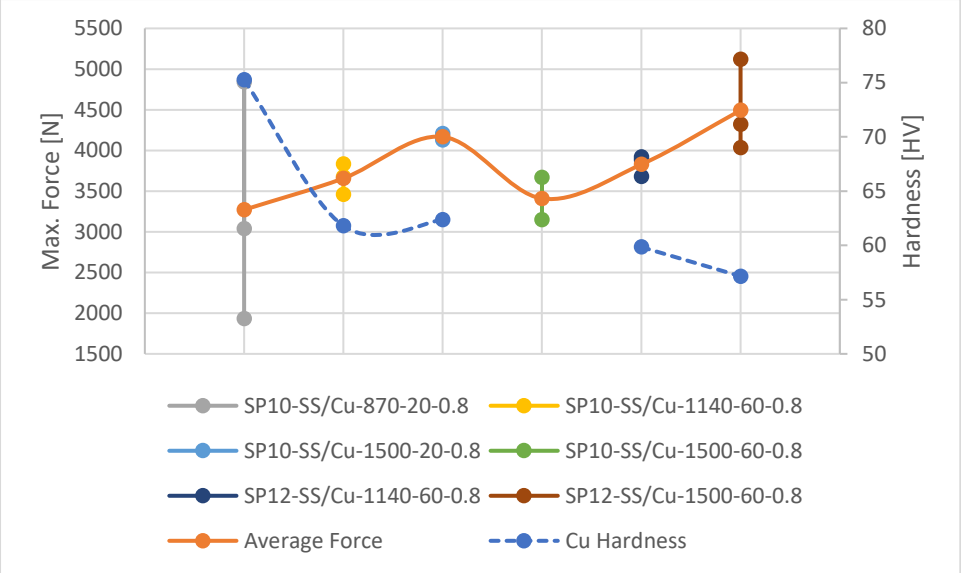

Figure 48 - Maximum and average force compared to the hardness for each weld.

As seen in the macrostructure analysis, the suggested joint width tended to increase with the increase of parameters, leading to an increase in strength since the welded area would be more extensive. However, the hardness has the opposite effect; by increasing parameters, a reduction was seen in copper, visible in Fig. 48, which is expected to reduce the strength of the weld; this means that two different factors have opposite effects on the weld strength, which was also identified by Chu et al. and Ataya et al. [39,49].

After the specimen fracture, the measure of the remained bonding area was done in some samples. By remaining bonding area is understood as the area of the copper that remained in the SS, exemplified by a blue circle in Fig. 47a). For one of the specimens of the SP10-SS/Cu-1140-60-0.8 welds, a remained bonding area of 52.89 mm^2 was registered. 51.32 mm^2 was registered for the SP10-SS/Cu-1500-20-0.8 specimen. Between these two welds, the bonding area decreases, which is expected since the welding time is reduced, and the slight increase in rpm is not significant to equal or increase this area, which means that this reduction would lead to a reduction in force. However, this is not the case because between those two trials, as shown by Fig. 48, the hardness was not so reduced, which makes the effect of the lower bonding area almost irrelevant. Furthermore, for the weld SP10-SS/Cu-1500-60-0.8, the area measured was 54.97 $mm^{2,}$ and despite being superior to the earlier

ones, there is a decrease in strength. Based on the results obtained from the hardness testing, the inferior force registered can be explained by the expected hardness reduction, even though it was not measured because of the sample damage during preparation. Despite the higher parameters increasing the bonding area, it was enough to compensate for the decrease in hardness. In the case of the SP12-SS/Cu-1500-60-0.8 trial, corresponding to the maximum parameters, one specimen achieved the highest force among the other welds, with a bonding area of 90.76 mm^2; this shows that the area bonded was able to counteract the effect of the hardness reduction since this was the weld with the lowest hardness in copper, as shown in Fig. 48.

With this, it can be said that the best weld is the SP10-SS/Cu-1500-20-0.8, both in terms of force obtained since the two specimens obtained similar values to the lowest two of the SP12-SS/Cu-1500-60-0.8 weld. Also, in terms of industrial application, since this weld has lower parameters, which decreases the welding execution time and the energy necessary to execute the weld.

5. Conclusions

The development of the present work, which was aimed at study the morphological, microstructural, and mechanical properties of copper-DHP to SS AISI 304 friction stir spot welds, allowed the following conclusions to be drawn:

For the given experimental layout, it was possible to achieve six successful welds out of 16 trials. The material position was a determining factor in achieving successful welds, with none of the trials performed with copper as the top plate producing consistent welds. On the other hand, some SS/Cu trials presented consistency after the process, where for each tool tested (10 and 12 mm in diameter), higher rotational speed and welding time favored good bonding conditions. The expected pressure increment for the tool with a smaller diameter also made it possible to achieve welds with lower welding times and rotational speeds.

All the trials showed a shining weld surface, leaving a slight indentation of the tool without visible defects. The different parameters, material position, and fixture system affected the visual appearance of the welds. A change of color with a circumferential format was seen for all the weld surfaces, with its intensity getting more significant with increments in all parameters. For a Cu/SS material position, the SS showed minimal morphological change. At the same time, the copper appearance was highly affected by the fixture system, which allowed a non-uniform dispersion of the heat. On the other hand, with the SS/Cu material position, a morphological change was seen for both materials.

The difference in thermal conductivity between the materials revealed opposite effects on the temperature for the two material positions tested. During the welds with a Cu/SS material configuration, the temperature evolution revealed a very evident temperature stabilization, achieving lower temperature values than the SS/Cu position for the same parameters, except for the coldest parameters. Contrarily, with the SS/Cu position, a continuous temperature increase during the welding phase was measured. Also, the welds produced with both tools revealed a temperature rise with increments in rotational speed and welding time, with the largest diameter achieving higher temperatures. However, it was seen that for the SP12 tool, the temperature threshold was reached, where the temperature rising almost became independent of the rotational speed.

The cross-section macrostructure revealed a defect-free bonding line with no mixing between copper and SS, showing that the bonding was not achieved by macro-mechanical interlocking. It also explained why the weld performed with the lowest heat input achieved

bonding since there was a significant reduction in thickness. Another observation was that the bonding length increased as the parameters got higher.

The copper's etching revealed the formation of a HAZ, where grain growth occurred over the entire thickness of the material and with a width superior to the one corresponding to the shoulder actuation zone, which expanded with the largest tool diameter. A higher tool diameter, rotational speed, and welding time allowed the grain to grow further. However, this growth was more expressive for different welding times. A micro-mechanical interlocking was seen during the SEM/EDS analyses, with the EDS element map showing Cu on the SS surface and Fe on the copper surface. The EDS line scan revealed that diffusion had occurred between elements of both materials.

The hardness distribution was found to increase on the upper sheet (SS) and decrease on the lower sheet (copper) compared to the BM, with a minor difference between the horizontal and the transversal hardness profiles. As the temperature increased, a continuous reduction was seen in the copper’s hardness, which is in line with the results obtained in the grain analysis since the grain also had a continuous increase.

Good repeatability was seen for almost all the welds, with some conditions, like colder parameters or more worn tools, showing a higher dispersion in results. It was also found that the welds had reliable performance since the nugget pull-out failure type was witnessed for 15 trials, while one weld failed by interfacial mode.

The parameters also had an opposite effect on the maximum force achieved for each weld. While the increase in joint width, enhanced by the parameters, led to a higher resistant area, thus improving the force achieved. The hardness for the same increase in parameters decreased the strength of the weld since higher temperatures led to more significant grain growth in the copper sheet. In terms of average maximum load, the weld that reached the most significant strength was the one with the highest parameters, achieving 4493.54 N average force, even though it registered the lowest hardness in the copper. However, in terms of industrial application, it should be pointed out that the weld that a 20 s welding time and a 10 mm tool were used achieved an average force of 4168.07 N, with the lowest dispersion among the other trials and an intermediate value of copper hardness. Additionally, it allows the parameters to be reduced, thus reducing the energy needed and the welding execution time.

This work may interest future investigations that want to explore new parameters or different testing conditions and can find this work as a starting point or even use it to compare results. Some future proposals are the microstructural characterization of the SS, which would allow, with the support of hardness evolution, to distinguish the microstructural zones. The characterization of the grain quantitatively would also allow an analysis of how parameters and temperature affect grain evolution. Since the temperature measurement was not done in the center of the shoulder actuation zone, it would be interesting to obtain that recording, which would allow the measurement of the maximum effective temperature. Measure the axial force applied (if position-controlled) by the machine to the different tool diameters to establish a relationship between temperature-axial force. A more detailed analysis of diffusion, both in terms of diffusion distance and its variation with parameters and temperature, would also help to understand this phenomenon and its contribution to the strength of the weld. The possibility, with the tensile-shear testing, of obtaining the stress-strain curve to calculate the joint efficiency. Finally, conduct a fatigue study to obtain a fatigue life prediction, subjecting the specimens to dynamic loads.

References

[1] Shokri, V., Sadeghi, A., and Sadeghi, M. H., 2017, "Effect of Friction Stir Welding Parameters on Microstructure and Mechanical Properties of DSS–Cu Joints," Materials Science and Engineering: A, **693**, pp. 111–120.

[2] Martins, J., 2013, "Joining Copper to Stainless Steel by Friction Stir Diffusion Process," masterThesis, Faculdade de Ciências e Tecnologia.

[3] Wang, T., Shukla, S., Nene, S. S., Frank, M., Wheeler, R. W., and Mishra, R. S., 2018, "Towards Obtaining Sound Butt Joint Between Metallurgically Immiscible Pure Cu and Stainless Steel Through Friction Stir Welding," Metall Mater Trans A, **49**(7), pp. 2578–2582.

[4] Saravanan, S., and Raghukandan, K., 2012, "Weldability Windows for Explosive Cladding of Dissimilar Metals," Advanced Materials Research, **445**, pp. 729–734.

[5] Gao, Y., Nakata, K., Nagatsuka, K., Matsuyama, T., Shibata, Y., and Amano, M., 2016, "Microstructures and Mechanical Properties of Friction Stir Welded Brass/Steel Dissimilar Lap Joints at Various Welding Speeds," Materials & Design, **90**, pp. 1018–1025.

[6] He, J., Sirois, D., Li, S., Sullivan, M., Wikle, C., and Chin, B. A., 2016, "Ballistic Impact Welding of Copper to Low Carbon Steel," Journal of Materials Processing Technology, **232**, pp. 165–174.

[7] Aval, H. J., 2018, "Microstructural Evolution and Mechanical Properties of Friction Stir-Welded C71000 Copper–Nickel Alloy and 304 Austenitic Stainless Steel," International Journal of Minerals, Metallurgy, and Materials, **25**(11), pp. 1294–1303.

[8] Joshi, G. R., and Badheka, V. J., 2019, "Studies on Tool Shoulder Diameter of Dissimilar Friction Stir Welding Copper to Stainless Steel," Metallography, Microstructure, and Analysis, **8**(2), pp. 263–274.

[9] Sadeghian, A., and Iqbal, N., 2022, "A Review on Dissimilar Laser Welding of Steel-Copper, Steel-Aluminum, Aluminum-Copper, and Steel-Nickel for Electric Vehicle Battery Manufacturing," Optics & Laser Technology, **146**, p. 107595.

[10] Gaspar, R. da C., 2020, "Torque and Temperature Analysis in FSSW of Aluminium Alloys," Universidade de Coimbra.

[11] Shen, Z., Ding, Y., and Gerlich, A. P., 2020, "Advances in Friction Stir Spot Welding," Critical Reviews in Solid State and Materials Sciences, **45**(6), pp. 457–534.

[12] Mazda, 2003, "Mazda Develops World's First Aluminum Joining Technology Using Friction Heat" [Online]. Available: https://newsroom.mazda.com/en/publicity/release/2003/200302/0227e.html. [Accessed: 19-Jan-2022].

[13] Lakshminarayanan, A. K., Annamalai, V. E., and Elangovan, K., 2015, "Identification of Optimum Friction Stir Spot Welding Process Parameters Controlling the Properties of Low Carbon Automotive Steel Joints," Journal of Materials Research and Technology, **4**(3), pp. 262–272.

[14] Ojo, O. O., Taban, E., and Kaluc, E., 2015, "Friction Stir Spot Welding of Aluminum Alloys: A Recent Review," Materials Testing, **57**(7–8), pp. 609–627.

[15] Han, S., Li, Z., Wang, Z., and Li, Y., 2022, “Review on Joining Processes of Magnesium Alloy Sheets,” Int J Adv Manuf Technol, **118**(9), pp. 2787–2803.
[16] García-Castillo, F. A., Reyes, L. A., Garza, C., López-Botello, O. E., Hernández-Muñoz, G. M., and Zambrano-Robledo, P., 2020, “Investigation of Microstructure, Mechanical Properties, and Numerical Modeling of Ti6Al4V Joints Produced by Friction Stir Spot Welding,” J. of Materi Eng and Perform, **29**(6), pp. 4105–4116.
[17] Akinlabi, E. T., Sanusi, K. O., Muzenda, E., and Akinlabi, S. A., 2017, “Material Behaviour Characterization of Friction Stir Spot Welding of Copper,” Materials Today: Proceedings, **4**(2, Part A), pp. 166–177.
[18] Sarkar, R., Pal, T. K., and Shome, M., 2016, “Material Flow and Intermixing during Friction Stir Spot Welding of Steel,” Journal of Materials Processing Technology, **227**, pp. 96–109.
[19] Li, M., Zhang, C., Wang, D., Zhou, L., Wellmann, D., and Tian, Y., 2020, “Friction Stir Spot Welding of Aluminum and Copper: A Review,” Materials, **13**(1), p. 156.
[20] Ke, W. C., Oliveira, J. P., Ao, S. S., Teshome, F. B., Chen, L., Peng, B., and Zeng, Z., 2022, “Thermal Process and Material Flow during Dissimilar Double-Sided Friction Stir Spot Welding of AZ31/ZK60 Magnesium Alloys,” Journal of Materials Research and Technology, **17**, pp. 1942–1954.
[21] Akinlabi, E. T., Osinubi, A. S., Madushele, N., Akinlabi, S. A., and Ikumapayi, O. M., 2020, “Data on Microhardness and Structural Analysis of Friction Stir Spot Welded Lap Joints of AA5083-H116,” Data in Brief, **33**, p. 106585.
[22] Benyerou, D., Chikh, E. B. O., Khellafi, H., Meddah, H. M., Benhamena, A., Hachelaf, K., and Lounis, A., 2021, “Parametric Study of Friction Stir Spot Welding (FSSW) for Polymer Materials Case of High Density Polyethylene Sheets: Experimental and Numerical Study,” Frat. Integrita Strut., (55), pp. 145–158.
[23] Tozaki, Y., Uematsu, Y., and Tokaji, K., 2010, “A Newly Developed Tool without Probe for Friction Stir Spot Welding and Its Performance,” Journal of Materials Processing Technology, **210**(6), pp. 844–851.
[24] Schilling, C., and Santos, J. dos, 2004, “Method and Device for Joining at Least Two Adjoining Work Pieces by Friction Welding.”
[25] Hirano, S., Okamoto, K., and Hunt, F., 2005, “Development of Friction Stir Welding Technique and Machine for Aluminum Sheet Metal Assembly- Friction Stir Welding of Aluminum for Automotive Applications (2) -,” *SAE 2005 World Congress & Exhibition*, SAE International.
[26] Schilling, C., von Strombeck, A., dos Santos, J., and von Heesen, N., 2000, “A Preliminary Investigation on the Static Properties of Friction Stir Spot Welds,” The Welding Institute (TWI), Cambridge, UK;, Gothenburg, Sweden.
[27] Buffa, G., Fratini, L., and Piacentini, M., 2008, “On the Influence of Tool Path in Friction Stir Spot Welding of Aluminum Alloys,” Journal of Materials Processing Technology, **208**(1), pp. 309–317.
[28] Sun, Y. F., Fujii, H., Takaki, N., and Okitsu, Y., 2011, “Novel Spot Friction Stir Welding of 6061 and 5052 Al Alloys,” Science and Technology of Welding and Joining, **16**(7), pp. 605–612.

[29] Farmanbar, N., Mousavizade, S. M., and Ezatpour, H. R., 2019, “Achieving Special Mechanical Properties with Considering Dwell Time of AA5052 Sheets Welded by a Simple Novel Friction Stir Spot Welding,” Marine Structures, **65**, pp. 197–214.
[30] Gao, Y., Liang, Y., Ren, X., and Paidar, M., 2020, “Pre-Hole Friction Stir Spot Welding (PFSSW) for Dissimilar Welding of AA2219 to AA3003 Sheets,” Vacuum, **182**, p. 109688.
[31] Yapici, G. G., and Ibrahim, I. J., 2021, “On the Fatigue and Fracture Behavior of Keyhole-Free Friction Stir Spot Welded Joints in an Aluminum Alloy,” Journal of Materials Research and Technology, **11**, pp. 40–49.
[32] Wang, X., Morisada, Y., and Fujii, H., 2021, “Flat Friction Stir Spot Welding of Low Carbon Steel by Double Side Adjustable Tools,” Journal of Materials Science & Technology, **66**, pp. 1–9.
[33] El-Sayed, M. M., Shash, A. Y., Abd-Rabou, M., and ElSherbiny, M. G., 2021, “Welding and Processing of Metallic Materials by Using Friction Stir Technique: A Review,” Journal of Advanced Joining Processes, **3**, p. 100059.
[34] Sharma, C., Tripathi, A., Upadhyay, V., Verma, V., and Sharma, S. K., 2021, “Friction Stir Spot Welding-Process and Weld Properties: A Review,” J. Inst. Eng. India Ser. D, **102**(2), pp. 549–565.
[35] Fujimoto, M., Koga, S., Abe, N., Sato, Y. S., and Kokawa, H., 2008, “Microstructural Analysis of Stir Zone of Al Alloy Produced by Friction Stir Spot Welding,” Science and Technology of Welding and Joining, **13**(7), pp. 663–670.
[36] Infante, V., and Vidal, C., 2014, “5 - Tool and Welding Design,” *Advances in Friction-Stir Welding and Processing*, M.K.B. Givi, and P. Asadi, eds., Woodhead Publishing, pp. 199–240.
[37] Correia, G. R. C., 2019, “Uso da soldadura por fricção linear para otimizar a resistência mecânica de juntas coladas sobrepostas,” Universidade de Coimbra.
[38] Krishnan, K. N., 2002, “On the Formation of Onion Rings in Friction Stir Welds,” Materials Science and Engineering: A, **327**(2), pp. 246–251.
[39] Chu, Q., Yang, X. W., Li, W. Y., and Li, Y. B., 2016, “Microstructure and Mechanical Behaviour of Pinless Friction Stir Spot Welded AA2198 Joints,” null, **21**(3), pp. 164–170.
[40] Fang, F., Yong, Q., Yang, C., and Su, H., 2009, “Microstructure and Precipitation Behavior in HAZ of V and Ti Microalloyed Steel,” Journal of Iron and Steel Research, International, **16**(3), pp. 68–77.
[41] Naffakh, H., Shamanian, M., and Ashrafizadeh, F., 2009, “Dissimilar Welding of AISI 310 Austenitic Stainless Steel to Nickel-Based Alloy Inconel 657,” Journal of Materials Processing Technology, **209**(7), pp. 3628–3639.
[42] Qin, H., Zhang, H., and Wu, H., 2015, “The Evolution of Precipitation and Microstructure in Friction Stir Welded 2195-T8 Al–Li Alloy,” Materials Science and Engineering: A, **626**, pp. 322–329.
[43] Alaeibehmand, S., Mirsalehi, S. E., and Ranjbarnodeh, E., 2021, “Pinless FSSW of DP600/Zn/AA6061 Dissimilar Joints,” Journal of Materials Research and Technology, **15**, pp. 996–1006.

[44] Albannai, A., 2020, “Review The Common Defects In Friction Stir Welding,” International Journal of Scientific & Technology Research, **9**, pp. 318–329.
[45] Bakavos, D., Chen, Y., Babout, L., and Prangnell, P., 2011, “Material Interactions in a Novel Pinless Tool Approach to Friction Stir Spot Welding Thin Aluminum Sheet,” Metall Mater Trans A, **42**(5), pp. 1266–1282.
[46] Sahlot, P., Nene, S. S., Frank, M., Mishra, R. S., and Arora, A., 2018, “Towards Attaining Dissimilar Lap Joint of CuCrZr Alloy and 316L Stainless Steel Using Friction Stir Welding,” null, **23**(8), pp. 715–720.
[47] Barlas, Z., 2017, “Weldability of CuZn30 Brass/DP600 Steel Couple by Friction Stir Spot Welding,” Acta Physica Polonica A, **132**(3), pp. 991–993.
[48] Abdullah, I., and Hussein, S., 2018, “Improving the Joint Strength of the Friction Stir Spot Welding of Carbon Steel and Copper Using the Design of Experiments Method,” Multidiscipline Modeling in Materials and Structures, **14**(5), pp. 908–922.
[49] Ataya, S., Ahmed, M. M. Z., El-Sayed Seleman, M. M., Hajlaoui, K., Latief, F. H., Soliman, A. M., Elshaghoul, Y. G. Y., and Habba, M. I. A., 2022, “Effective Range of FSSW Parameters for High Load-Carrying Capacity of Dissimilar Steel A283M-C/Brass CuZn40 Joints,” Materials, **15**(4), p. 1394.
[50] Shen, Z., Chen, Y., Haghshenas, M., Nguyen, T., Galloway, J., and Gerlich, A. P., 2015, “Interfacial Microstructure and Properties of Copper Clad Steel Produced Using Friction Stir Welding versus Gas Metal Arc Welding,” Materials Characterization, **104**, pp. 1–9.
[51] Gao, Y., Nakata, K., Nagatsuka, K., Shibata, Y., and Amano, M., 2016, “Optimizing Tool Diameter for Friction Stir Welded Brass/Steel Lap Joint,” Journal of Materials Processing Technology, **229**, pp. 313–321.
[52] Lee, R.-T., Liu, C.-T., Chiou, Y.-C., and Chen, H.-L., 2013, “Effect of Nickel Coating on the Shear Strength of FSW Lap Joint between Ni–Cu Alloy and Steel,” Journal of Materials Processing Technology, **213**(1), pp. 69–74.
[53] Mahto, M. K., Kumar, A., Raja, A. R., Vashista, M., and Yusufzai, M. Z. K., 2021, “Cladding of Copper Sheet on Mild Steel Using Friction Stir Welding,” The International Journal of Advanced Manufacturing Technology.
[54] Najafkhani, A., Zangeneh-Madar, K., and Abbaszadeh, H., 2010, “Evaluation of Microstructure and Mechanical Properties of Friction Stir Welded Copper / 316L Stainless Steel Dissimilar Metals,” International Journal of Iron & Steel Society of Iran, **7**(2), pp. 21–25.
[55] Srinivas, K., Ramachandran, S., Lakshminarayanan, A., Nagarajan, S., and Balasubramaniam, V., 2015, “Zone Wise Properties of Friction Stir Welded Copper – Stainless Steel Joints Using Digital Image Correlation,” Applied Mechanics and Materials, **787**, pp. 485–489.
[56] Jafari, M., Abbasi, M., Poursina, D., Gheysarian, A., and Bagheri, B., 2017, “Microstructures and Mechanical Properties of Friction Stir Welded Dissimilar Steel-Copper Joints,” Journal of Mechanical Science and Technology, **31**(3), pp. 1135–1142.
[57] Joshi, G. R., and Badheka, V. J., 2017, “Microstructures and Properties of Copper to Stainless Steel Joints by Hybrid FSW,” Metallography, Microstructure, and Analysis, **6**(6), pp. 470–480.

[58] Giridharan, K., Sevvel, P., Gurijala, C., and Kumar, B. Y., 2021, "Biochar-Assisted Copper-Steel Dissimilar Friction Stir Welding: Mechanical, Fatigue, and Microstructure Properties," Biomass Conversion and Biorefinery.
[59] ASM International Handbook Committee., 1990, *ASM Handbook, Volume 01 - Properties and Selection: Irons, Steels, and High-Performance Alloys*, ASM International., The Netherlands.
[60] ASM International Handbook Committee., 1990, *ASM Handbook, Volume 02 - Properties and Selection: Nonferrous Alloys and Special-Purpose Materials*, ASM International., The Netherlands.
[61] Baghel, P. K., 2012, "Design and Development of Fixture for Friction Stir Welding," Innovative Systems Design and Engineering, **3**, pp. 40–47.
[62] Reilly, A., Shercliff, H., Chen, Y., and Prangnell, P., 2015, "Modelling and Visualisation of Material Flow in Friction Stir Spot Welding," Journal of Materials Processing Technology, **225**, pp. 473–484.
[63] Ma, Z., Li, Q., Ma, L., Hu, W., and Xu, B., 2019, "Process Parameters Optimization of Friction Stir Welding of 6005A-T6 Aluminum Alloy Using Taguchi Technique," Trans Indian Inst Met, **72**(7), pp. 1721–1731.
[64] Memon, S., Fydrych, D., Fernandez, A. C., Derazkola, H. A., and Derazkola, H. A., 2021, "Effects of FSW Tool Plunge Depth on Properties of an Al-Mg-Si Alloy T-Joint: Thermomechanical Modeling and Experimental Evaluation," Materials (Basel), **14**(16), p. 4754.
[65] Gulati, P., and Piyush, D. K., 2017, "Investigation of the Effects of Plunge Depth on the Resulting Temperature Distribution, Microstructure and Mechanical Properties of Friction Stir Welded AZ31B Magnesium Alloy," IJAMMC, **7**(2), pp. 53–59.
[66] Sahu, P. K., and Pal, S., 2014, "Effect of Shoulder Diameter and Plunging Depth on Mechanical Properties and Thermal History of Friction Stir Welded Magnesium Alloy," undefined.
[67] Andrade, D. G., Leitão, C., and Rodrigues, D. M., 2019, "Influence of Base Material Characteristics and Process Parameters on Frictional Heat Generation during Friction Stir Spot Welding of Steels," Journal of Manufacturing Processes, **43**, pp. 98–104.
[68] Li, G., Zhou, L., Zhou, W., Song, X., and Huang, Y., 2019, "Influence of Dwell Time on Microstructure Evolution and Mechanical Properties of Dissimilar Friction Stir Spot Welded Aluminum–Copper Metals," Journal of Materials Research and Technology, **8**(3), pp. 2613–2624.
[69] Zhou, L., Li, G. H., Zhang, R. X., Zhou, W. L., He, W. X., Huang, Y. X., and Song, X. G., 2019, "Microstructure Evolution and Mechanical Properties of Friction Stir Spot Welded Dissimilar Aluminum-Copper Joint," Journal of Alloys and Compounds, **775**, pp. 372–382.
[70] Klobčar, D., Tušek, J., Smolej, A., and Simončič, S., 2015, "Parametric Study of FSSW of Aluminium Alloy 5754 Using a Pinless Tool," Weld World, **59**(2), pp. 269–281.
[71] Andrade, D. G., Leitão, C., and Rodrigues, D. M., 2018, "Properties of Lap Welds in Low Carbon Galvanized Steel Produced by Tool Assisted Friction Welding," Journal of Materials Processing Technology, **260**, pp. 77–86.

[72] Yazdi, S. R., Beidokhti, B., and Haddad-Sabzevar, M., 2019, “Pinless Tool for FSSW of AA 6061-T6 Aluminum Alloy,” Journal of Materials Processing Technology, **267**, pp. 44–51.
[73] Xie, X., Shen, J., Gong, F., Wu, D., Zhang, T., Luo, X., and Li, Y., 2016, “Effects of Dwell Time on the Microstructures and Mechanical Properties of Water Bath Friction Stir Spot-Welded AZ31 Magnesium Alloy Joints,” Int J Adv Manuf Technol, **82**(1–4), pp. 75–83.
[74] Luo, J., Xiang, J., Liu, D., Li, F., and Xue, K., 2012, “Radial Friction Welding Interface between Brass and High Carbon Steel,” Journal of Materials Processing Technology, **212**(2), pp. 385–392.
[75] Salje, G., and Feller-Kniepmeier, M., 1978, “The Diffusion and Solubility of Iron in Copper,” Journal of Applied Physics, **49**(1), pp. 229–232.
[76] Salje, G., and Feller-Kniepmeier, M., 1977, “The Diffusion and Solubility of Copper in Iron,” Journal of Applied Physics, **48**(5), pp. 1833–1839.
[77] Dehghan-Manshadi, A., Barnett, M. R., and Hodgson, P. D., 2008, “Recrystallization in AISI 304 Austenitic Stainless Steel during and after Hot Deformation,” Materials Science and Engineering: A, **485**(1), pp. 664–672.
[78] Sarkar, R., Pal, T. K., and Shome, M., 2014, “Microstructures and Properties of Friction Stir Spot Welded DP590 Dual Phase Steel Sheets,” Science and Technology of Welding and Joining, **19**(5), pp. 436–442.
[79] Zhang, Z., Yu, Y., Zhao, H., and Wang, X., 2019, “Interface Behavior and Impact Properties of Dissimilar Al/Steel Keyhole-Free FSSW Joints,” Metals, **9**(6), p. 691.
[80] Liu, F. C., Hovanski, Y., Miles, M. P., Sorensen, C. D., and Nelson, T. W., 2018, “A Review of Friction Stir Welding of Steels: Tool, Material Flow, Microstructure, and Properties,” Journal of Materials Science & Technology, **34**(1), pp. 39–57.
[81] Sato, Y. S., Nelson, T. W., and Sterling, C. J., 2005, “Recrystallization in Type 304L Stainless Steel during Friction Stirring,” Acta Materialia, **53**(3), pp. 637–645.
[82] Marashi, P., Pouranvari, M., Amirabdollahian, S., Abedi, A., and Goodarzi, M., 2008, “Microstructure and Failure Behavior of Dissimilar Resistance Spot Welds between Low Carbon Galvanized and Austenitic Stainless Steels,” Materials Science and Engineering: A, **480**(1), pp. 175–180.
[83] Mohamadizadeh, A., Biro, E., and Worswick, M., 2020, “Shear Band Formation at the Fusion Boundary and Failure Behaviour of Resistance Spot Welds in Ultra-High-Strength Hot-Stamped Steel,” Science and Technology of Welding and Joining, **25**(7), pp. 556–563.
[84] Janardhan, G., Mukhopadhyay, G., and Dutta, K., 2022, “Failure Behaviour of Spot-Welds on Automotive Steel Sheets,” Materials Today: Proceedings, **62**, pp. 6120–6124.
[85] Rosendo, T., Tier, M., Mazzaferro, J., Mazzaferro, C., Strohaecker, T. R., and Dos Santos, J. F., 2015, “Mechanical Performance of AA6181 Refill Friction Spot Welds under Lap Shear Tensile Loading,” Fatigue & Fracture of Engineering Materials & Structures, **38**(12), pp. 1443–1455.